

# Adsorption and Self-Organization of Organophosphonic Monolayers on Modified Oxide Covered Surfaces

An der Fakultät für Naturwissenschaften  
der Universität Paderborn  
zur Erlangung des Grades eines  
Doktor der Naturwissenschaften (Dr. rer. nat.)  
eingereichte

D i s s e r t a t i o n

vorgelegt von

**Dipl.-Chem. Peter Thissen**

geb. am 1. März 1982 in Willich

1. Prüfer:	Prof. Dr. Guido Grundmeier
2. Prüfer:	Prof. Dr. Dirk Kuckling
3. Prüfer:	Prof. Dr. Wolf Gero Schmidt
Tag der Einreichung:	26.05.2009
Tag der mündlichen Prüfung:	30.06.2009

Paderborn, am 25.05.2009

Gewidmet meinem lieben Vater Johannes Thissen, der für mich und die ganze Familie immer als Vorbild vorangeht; und meiner lieben Mutter Marion Thissen, die zu jeder Zeit auch die Probleme anderer Menschen sieht.

## Danksagung - Acknowledgement

Für meine Doktorarbeit schulde ich sehr vielen Menschen einen herzlichen Dank.

Besonders hervorheben möchte ich meinen Doktorvater, Herrn Prof. Dr. Guido Grundmeier. Die Vergabe eines interessanten Themengebietes und die damit verbundenen fachspezifischen und auch privaten Gespräche sorgten dafür, daß ich mich während der Zeit als Doktorant sehr gut und selbstständig entwickeln konnte.

Selbstverständlich gilt mein Dank auch Herrn Prof. Dr. Dirk Kuckling, der sich viel Zeit für die Übernahme des Koreferats genommen hat.

Tatkräftig unterstützt wurde ich von Herr Prof. Dr. Martin Stratmann; durch ihn erhielt ich die Möglichkeit zur Durchführung aller experimentellen und theoretischen Arbeiten am Max-Planck-Institut für Eisenforschung in Düsseldorf.

Allen Mitarbeitern des Max-Planck-Instituts danke ich für die angenehme Arbeitsatmosphäre und manch aufmunterndes Wort.

In diesem Zusammenhang möchte ich besonders Herrn Dr. Christian Stromberg danken. Er hat mich für die Arbeit in der Eisenforschung sensibilisiert und stark motiviert.

Mit Herrn Dr. Miroslaw Giza verband mich eine gute Kooperation im ersten Jahr meiner Doktorarbeit.

Mit Herrn Dr. Detlef Diesing der Universität Duisburg-Essen führte ich zahlreiche konstruktive Diskussionen auf verschiedenen Fachgebieten.

Özlem Özcan, Edmanuel Torres, Dr. Juan Zuo, Tobias Titz, Rene Vlasak, Dr. Ingo Klüppel, Sergiy Borodin, Galina Giza, Dr. Ullrich Biedermann, Petra Ebbinghaus, Dr. Guoguang Sun, Dr. Xumei Wang, Dr. Nicole Fink, Vesselina Popova, Berkem Özkaya, Dr. Markus Valtiner, Ralf Posner, Monika Santa, Haybat Itani, Dr. Patrick Keil und Eberhard Heinen danke ich für viel Kritik; sie haben mir mit ihrem Fachwissen und ihren vielen Ideen immer wieder den nötigen Aufschwung gegeben. 'Danke' sage ich aber auch für den Ausgleich zur wissenschaftlichen Arbeit in Form von Sport und zahlreichen Ausflügen.

Mein Dank gilt auch allen Mitarbeitern der Arbeitsgruppe 'Technische und Makromolekulare Chemie' für die schnelle und freundliche Aufnahme an der Universität Paderborn. Dies ist bei einer örtlichen Neuorientierung sehr wichtig. Besonders hervorheben möchte ich Thomas Arens, Markus Voigt und Claudia Altmiks.

Ich bedanke mich auch bei Herrn Prof. Dr. Wolf Gero Schmidt und

seinen Mitarbeitern Stefan Wippermann und Dr. Simone Sanna, die viel Zeit und Geduld investierten, um mir das Tor zur theoretischen Chemie neu zu öffnen.

Ferner gilt mein Dank Frau Köyer, Frau Dr. Krebs und Herrn Meurer vom Dortmunder Oberflächencentrum sowie Herrn Maurus, Herrn Dr. Schmidt-Hansberg und Herrn Dr. Schubert von der Chemetall für die sehr gute Zusammenarbeit im Projekt 'Neuartige kombinierte Produktionsverfahren mit hoher Nachhaltigkeit für die Beschichtung von Stahlband'.

Mein spezieller Dank geht an Vera Moellmann für die L<sup>A</sup>T<sub>E</sub>X-Hilfe beim Schreiben der Arbeit und Mr. Peter Hetzler für den letzten Schliff beim Englischen.

Nicht vergessen möchte ich Herrn Dr. Michael Schillings, der seit zehn Jahren mein Leben begleitet und der mich immer bestärkt hat, meinen Weg zu gehen.

Ein ganz besonderer Dank gilt meiner gesamten Familie. Sie brachte mir viel Geduld entgegen und hat mich immer wieder bestärkt, wenn ich einmal an mir gezweifelt habe. Sie hat immer an den Erfolg meiner Arbeit geglaubt.

Meine Patentante Henny hat mich stets gestützt und mir in vielerlei Hinsicht geholfen. Ich danke ihr.

Dem Bundestministerium für Bildung und Forschung, BMBF, danke ich für die Bereitstellung der finanziellen Mittel.

## Kurzfassung

Die vorliegende Arbeit befasst sich mit dem Korrosionsschutz technisch relevanter Oberflächen durch neuartig kombinierte Produktionsverfahren, die in der Wirtschaft eine hohe Nachhaltigkeit aufweisen. Am Anfang steht eine Konzeptentwicklung der plasmabasierten Konditionierung der chemischen und elektronischen Struktur von Passivschichten und der Untersuchung des Einflusses einer plasmamodifizierten Oxidschicht auf die Adsorption, Selbstorganisation und Adhäsion von organischen Haftvermittlern. Hierbei kann erstmals durch den Einsatz der Quarzkristallmikrowägung (QCM) für das System Octadecylphosphonsäure (ODPA) / Aluminiumoxid eine zehnfache Beschleunigung der Adsorptionsgeschwindigkeit aufgrund der Plasmamodifikation direkt nachgewiesen werden. Um ein größeres Spektrum an Forschungsmöglichkeiten zu erhalten, werden die zu untersuchenden Modellsysteme erweitert auf Aluminiumoxid-Einkristalle mit verschiedenen Oberflächenorientierungen einerseits, andererseits auf Zinkaluminium-Legierungen, die ihre Anwendung als Stahlüberzug in vielen Bereichen haben. Dabei werden vor allem die Bildung und Langzeitstabilität der als Self-Assembled Monolayer (SAM) adsorbierten ODPA auf den verschiedenen oxidbedeckten Aluminiumoberflächen fokussiert. Sowohl bei der Entstehung als auch bei der Stabilität der ODPA Monolayer zeigen sich klare Unterschiede auf den verschiedenen Oberflächen; viele können durch die Weiterentwicklung der bestehenden Bindungsmodelle für die Wechselwirkung zwischen ODPA und Aluminiumoxid verstanden werden. Bei der Bildung einer ODPA Monolage, die als Haftvermittler auf den gewählten Stahlüberzügen HDG, Galfan und Galvalume fungieren kann, kann gezeigt werden, dass ein Aluminiumgehalt  $< 0.5\%$  (HDG) zur Bildung einer Fällungsschicht und nicht mehr zur Selbstorganisation der ODPA auf der Oberfläche führt. Die Stabilität der Bindung zwischen ODPA und Aluminiumoxid im wässrigen Medium wird hauptsächlich von drei Faktoren beeinflusst, der Grenzflächen-Wechselwirkung, der freien Adsorptionsenergie im Vergleich zu Wasser und der atomaren Geometrie der Oberfläche. Schließlich wird durch den Einsatz einkristalliner Modellsysteme der Brückenschlag in die moderne Quantenmechanik geschafft. Für das System Phosphonsäure, adsorbiert als SAM auf Aluminiumoxid, werden die bestehenden Modelle aufgegriffen, zudem wird das Spektrum durch die Arbeit auf Einkristallen und einen theoretischen Ansatz erweitert. Für die Zukunft kann nur eine Kombination aus Grundlagenforschung, sowohl experimentell als auch theoretisch, und direkten Anbindungsversuchen mit der Industrie der Schlüssel zu fundamentalem Verständnis und ausreichendem Fortschritt sein.

## Abstract

The dissertation mainly deals with the protection of corrosion by novel combination of production processes which have a high sustainability in the economy. Topics like effects of the plasma modification on the adsorption kinetics of adhesion promoters, investigations on the adhesion promoters as corrosion inhibitors, and the influence of the surface chemistry on the stability of adsorbed adhesion promoters are brought into focus. It is shown, that plasma modification can influence the electronic and geometric parameters of the passive layers and thereby prevent corrosion, as well as the adsorption process of the adhesion promoter. The quartz crystal microweighing (QCM) is applied for the first time as a method for the determination of adsorption kinetics of organophosphonic acids on aluminum. Investigations of the adhesion promoters adsorbed on passive layers lead to the conclusion, that a further adsorption of water can be reduced but the diffusion itself to the passive layer cannot be hindered. The variation of surfaces and alloy composition has shown that adhesion promoters have to be adapted to the parameters of subject system to reach certain stability. The stability of the resulting bonding is mainly based on three competing influences, namely interfacial bonding types, adsorption free energies in competition with water and the involved adsorption geometries. By the introduction of new single crystalline model systems a gap between the modern theory and experimental data can be bridged. For water-rich conditions the formation of the adsorbing water is predicted by density functional theory (DFT) and proven by temperature programmed desorption (TPD) spectroscopy. In one can say that phosphonic acids are the most promising candidates as adhesion promoters for aluminum and alloys that form up oxide covered aluminum surfaces. Furthermore, the plasma modification is an efficient process for cleaning and changing the surface parameters in electronic and geometric way, which facilitates the possibility to tailor the surface chemistry. For the future, only a combination of basics research on the one hand, and direct cooperation with industry on the other hand, can be the key for fundamental comprehension and adequate progress.

# Contents

<b>1. Introduction</b>	<b>1</b>
1.1. General Review on the State of Research . . . . .	1
1.2. Motivation . . . . .	3
<b>2. Fundamentals</b>	<b>6</b>
2.1. Surface Chemistry of Single Crystalline Aluminum Oxide . . .	6
2.1.1. $\alpha - \text{Al}_2\text{O}_3(0001)$ . . . . .	6
2.1.2. $\alpha - \text{Al}_2\text{O}_3(1 - 102)$ . . . . .	8
2.2. Surface Chemistry of Aluminum and Alloys . . . . .	10
2.2.1. Native Grown Aluminum Oxide Films . . . . .	10
2.2.2. ZnAl Alloy Coatings . . . . .	11
2.3. Self-Assembled Monolayer Formation . . . . .	13
2.3.1. General Overview . . . . .	13
2.3.2. Mechanisms and Kinetics of Self-Assembled Monolayers Formation . . . . .	14
2.3.3. Self-Assembled Monolayers on Metal Surfaces . . . . .	16
2.3.4. Self-Assembled Monolayers on Oxide Covered Surfaces .	16
2.4. Adhesion Promoting Organophosphonic Acids . . . . .	19
2.4.1. Binding to the Oxide Surface . . . . .	19
2.4.2. Coupling Reactions at the Interface Self-Assembled Mono- layer/Polymer . . . . .	20
2.5. Ab initio Simulations . . . . .	22
2.5.1. The Schrödinger Equation . . . . .	22
2.5.2. The Molecular Hamiltonian . . . . .	23
2.5.3. The Born-Oppenheimer Approximation . . . . .	24
2.5.4. Density Functional Theory . . . . .	25
2.5.5. Pseudopotential Theory . . . . .	26
2.5.6. Supercell Approximation . . . . .	27
2.5.7. Iterative Minimization . . . . .	27
<b>3. Experimental</b>	<b>29</b>
3.1. Chemicals and Materials . . . . .	29
3.2. Fourier Transform Infrared Spectroscopy . . . . .	29

## Contents

3.2.1. Polarization Modulation Infrared Reflection Absorption Spectroscopy . . . . .	29
3.2.2. Spectra Refinement . . . . .	32
3.2.3. Diffuse Reflectance Infrared Fourier Transform Spectroscopy . . . . .	33
3.3. Quartz Crystal Microweighing . . . . .	34
3.3.1. Quartz Crystal Microweighing in Gas-Phase . . . . .	34
3.3.2. Quartz Crystal Microweighing in Liquids . . . . .	36
3.4. Contact Angle Measurements . . . . .	39
3.5. Thermal Desorption Spectroscopy . . . . .	40
3.6. Time-of-Flight Secondary Ion Mass Spectroscopy . . . . .	42
3.7. X-ray Photoelectron Spectroscopy . . . . .	43
3.8. Scanning Electron Microscopy . . . . .	44
<b>4. Adsorption Kinetics</b> . . . . .	<b>46</b>
4.1. Introduction . . . . .	46
4.2. Experimental . . . . .	47
4.2.1. Sample Preparation . . . . .	47
4.2.2. Surface Chemistry . . . . .	48
4.2.3. Surface Analysis . . . . .	50
4.2.4. Determination of the Mass Sensitivity . . . . .	50
4.3. Results and Discussion . . . . .	55
4.3.1. Plasma Surface Chemistry . . . . .	55
4.3.2. Adsorption Kinetics of Octadecylphosphonic Acid . . . . .	58
4.4. Conclusions . . . . .	65
4.5. Outlook . . . . .	65
<b>5. Formation and Stability I</b> . . . . .	<b>66</b>
5.1. Introduction . . . . .	66
5.2. Experimental . . . . .	68
5.2.1. Sample Preparation . . . . .	68
5.2.2. Surface Chemistry . . . . .	68
5.2.3. Surface Analysis . . . . .	69
5.3. Results and Discussion . . . . .	71
5.3.1. Plasma Surface Chemistry on Aluminum . . . . .	71
5.3.2. In-situ Quartz Crystal Microweighing during H <sub>2</sub> O and D <sub>2</sub> O Plasma Treatment of Aluminum Films. . . . .	75
5.3.3. Adsorption of Octadecylphosphonic Acid on the Oxide Covered Aluminum . . . . .	77
5.3.4. Dependence of the Adsorption Isotherms of D <sub>2</sub> O on the Surface Chemistry . . . . .	79
5.3.5. Self-Assembled Monolayer as Isotopic Barrier . . . . .	81

## Contents

5.4. Conclusions . . . . .	83
5.5. Outlook . . . . .	84
<b>6. Formation and Stability II</b>	<b>85</b>
6.1. Introduction . . . . .	85
6.2. Experimental . . . . .	87
6.2.1. Sample Preparation . . . . .	87
6.2.2. Static Contact Angle Measurements . . . . .	88
6.2.3. Atomic Force Microscopy . . . . .	88
6.2.4. Polarization Modulation Infrared Reflection Absorption Spectroscopy . . . . .	89
6.2.5. Diffuse Reflectance Infrared Fourier Transform Spectroscopy	89
6.3. Results . . . . .	89
6.3.1. Adsorption of Octadecylphosphonic Acid Monolayers on Aluminum Oxide Surfaces . . . . .	90
6.3.2. Stability of Octadecylphosphonic Acid Self-Assembled Monolayers on Aluminum Oxide Surface in an Aqueous Environment . . . . .	95
6.3.3. Fourier Transform Infrared Spectroscopy of Octadecylphosphonic Acid Covered Surfaces after Immersion in Water	103
6.4. Discussion . . . . .	105
6.5. Conclusions . . . . .	109
6.6. Outlook . . . . .	109
<b>7. Formation and Stability III</b>	<b>111</b>
7.1. Introduction . . . . .	111
7.2. Experimental . . . . .	113
7.2.1. Materials . . . . .	113
7.2.2. Sample Preparation . . . . .	113
7.2.3. Scanning Electron Microscopy . . . . .	115
7.2.4. X-ray Photoelectron Spectroscopy . . . . .	115
7.2.5. Polarization Modulation Infrared Reflection Absorption Spectroscopy . . . . .	116
7.2.6. Static Contact Angle . . . . .	116
7.2.7. Time-of-Flight Secondary Ion Mass Spectroscopy . . . . .	116
7.3. Results and Discussion . . . . .	117
7.3.1. Characterization of the ZnAl Alloy Coating Surfaces . . . . .	117
7.3.2. Adsorption of Octadecylphosphonic Acid Monolayers . . . . .	121
7.3.3. Stability of Octadecylphosphonic Acid Monolayers . . . . .	125
7.4. Conclusions . . . . .	126
7.5. Outlook . . . . .	128

*Contents*

<b>8. Water Adsorption on the <math>\alpha</math>-Al<sub>2</sub>O<sub>3</sub>(0001) Surface</b>	<b>129</b>
8.1. Introduction . . . . .	129
8.2. Theory . . . . .	130
8.3. Experimental . . . . .	131
8.4. Results and Discussion . . . . .	131
8.5. Conclusions . . . . .	141
<b>9. Overall conclusions and Outlook</b>	<b>143</b>
<b>Bibliography</b>	<b>147</b>
<b>A. Glossary</b>	<b>163</b>
<b>B. List of Symbols</b>	<b>164</b>
<b>C. Publications</b>	<b>165</b>
<b>D. Curriculum Vitae</b>	<b>166</b>

# 1. Introduction

This work is organized into four main parts. First an overview of the relevant literature followed by the motivation is given (chapter 1). In the second part the theoretical fundamentals (chapter 2) as well as the experimental setups (chapter 3) will be reviewed. The third part (chapter 4 - 8) summarizes and discusses the main results of this work, which is followed by a final discussion of the overall idea and an outlook (part four, chapter 9).

## 1.1. General Review on the State of Research

Low temperature plasma processes at reduced or atmospheric pressure are of high interest for the adjustment of surface chemistry on metals and polymers. In an extremely short period of time, the material surface can be changed in its chemical composition [1] [2]. Grundmeier et al. illustrated how oxide covered iron and zinc can be modified in their surface chemistry and oxide thickness [3] [4]. However, for most technical applications the time required to form a functional monolayer is crucial for the applicability in a process chain, the most challenging being continuous lines for aluminum sheet surface technology. Adsorption times of few tens of seconds would allow the integration of self-assembly processes in these high speed technologies. Till now the study of the kinetics of self-assembled monolayers (SAMs) on industrial relevant material was not in the focus of the investigations. Most monolayers were formed within hours of immersion in solution.

In recent years, especially the development of ZnAl containing coatings was in the focus of interest [5] [6] [7] [8] [9]. Worsley and employees showed that by changing the cooling temperature a change in the microstructure and hence a change to the corrosion stability follows. Analytical studies on the surface structure of the passive layer, however, were not carried out.

In a few years, molecular bonding agent systems such as bi-functional

## 1. Introduction

organophosphonate developed to marketability. Organophosphonate particularly were developed on aluminum alloys as alternative to chromate conversions, since the chemical bonding of phosphonic acid to the aluminum surface is extraordinarily stable. Thus there are also a few works that deal with the optimization of the oxide or hydroxide structure on metal surfaces prior to the application of these systems employ adhesion promoter molecules [10]. Initial approaches to simulate the interfacial bonds, however, indicate that based on the decrease of the surface density of hydroxides or even the structure of the adhesion promoter molecule an optimization of liability may be possible.

The corrosion resistance and the adhesion of organic coatings on oxide covered aluminum is of high importance and is mainly determined by the alloy composition, the surface chemistry of the alloy and the composition of the organic coating. To substitute surface technologies such as anodizing or conversion chemistry, adhesion promoting, ultra-thin films or even monomolecular layers like SAMs of organophosphonic acids have been investigated as new advanced interfacial layers for polymer coated aluminum alloys [11]. Although the adhesion and interfacial corrosion protection of these adsorbed monolayers proved to be excellent even in comparison to thicker conversion films, the barrier properties and the influence of water on the interface between the adsorbed organophosphonic acid and the oxide covered substrate were not evaluated in detail. The interaction of water with solid surfaces is fundamental to research in various fields ranging from atmospheric chemistry to corrosion and heterogenous catalysis. Despite substantial research, precise information on the water geometry at the atomic level often seems elusive, for the ubiquitous liquid phase [212] as well as for many cases of substrate-supported thin water films and clusters prepared in the laboratory [214] [217] [220]. Experimentally, most studies propose water dissociation on the Al-terminated  $\text{Al}_2\text{O}_3(0001)$  surface. This was concluded from high-resolution electron-energy-loss spectroscopy (HREELS) studies [221] as well as thermal desorption experiments [222] [223]. X-ray photoemission experiments [224] were interpreted to indicate water dissociation in particular at surface defect sites. Early ultraviolet photoelectron spectra, on the other hand, seem to indicate molecular adsorption of water at room temperature [225]. Also the mobility of the adsorbed molecules on the  $\text{Al}_2\text{O}_3(0001)$  surface seems to be a somewhat open question. In [223] a low mobility of the hydroxyl groups at the surface was stated, in contrast

## 1. Introduction

to the interpretation of dynamic scanning force microscopy images of the water exposed  $\text{Al}_2\text{O}_3(0001)$  surface [226]. Theoretically, most *ab initio* studies agree on the stability of the dissociative vs the molecular adsorption [227, 228, 229] while one cluster study [230] found little difference between the energies of molecular and dissociative adsorption of water.

## 1.2. Motivation

The generation of aluminum and aluminum alloy coatings on steel is one of the most commercially important processing techniques used to protect steel components exposed to corrosive environments. From a technological standpoint, the principles of galvanizing have remained unchanged since this coating came into use over 200 years ago. However, because of new applications in the automotive, aerospace and construction industry, a considerable amount of research has recently occurred on all aspects of the galvanizing process and on new types of coatings.

One objective of this dissertation consists of understanding the low temperature plasma based modification of the chemical and electronic structure of passive layers on ZnAl alloy surfaces and using the influence of a modified oxide on the adsorption, and self-organization of organic molecular adhesion promoters. Based on ZnAl alloys layer concepts for direct the connection of metal oxides and organic coatings will be developed. The correlation between the structure of the metal alloy layer terminating oxide and the resulting adhesion and corrosion resistance will be in the foreground.

The dissertation will focus on exploring the interaction between Al, Zn, surface oxides and adsorbed organic monolayers as well as on possible conditioning of passive layers through modification of manufacturing conditions in the hot dip arrangements, or PVD (physical vapor deposition) place. In the production of alloy layers natively growing ultra-thin oxide layers should be conditioned through plasma processes, which do not lead to chemically polymerization but a conversion of the oxide layer and the amendment of its thickness. The plasma modification has the following aims:

**(1):** Inhibition of electron transfer processes by influencing the semi-conducting properties of the oxide.

## 1. Introduction

**(2):** Setting the Fermi level in the oxide to reduce the driving force for cathodic delamination.

**(3):** Generate a certain density of OH groups on the oxide surface for linking organic adhesion promoters.

Afterwards, a covalently connecting organic phase should be achieved by adsorption. On the plasma modified oxide and hydroxide passive layers molecular bonding agents should be adsorbed in the next step. According to the literature organophosphonic acids are promising candidates [11] [12] [13] [14]. These components can be mixed to coating systems and guarantee an adhesion to the substrate by interfacial enrichment. Through the use of environmentally friendly plasma technology in combination with the procedure of self-organization of bi-functional organic molecules from the polymer phase one can achieve combined systems with outstanding characteristics and avoid environmental pollution caused by wastewater. Moreover, the molecular interfacial structuring is a very material efficient way of production, as ultra-thin oxide layers from the alloy grow and only monolayers of the adhesion promoter polymer/metal phase boundary are needed.

For a better understanding of the involved processes and mechanisms model systems were identified and used. Thus, studies on the aluminum oxide will start on single crystalline surfaces. Because of their purity, a well-known bulk structure and many other good properties, the sapphire single crystal samples with different surface orientations are a well suited model system for the aluminum oxide. They offer the possibility for new research approaches, like density functional theory (DFT) calculations, compared with the results of atomic force microscope (AFM) and diffuse reflectance infrared fourier transform spectroscopy (DRIFTS). The new knowledge can be partially transferred to polycrystalline bulk samples and be improved. Industrial nature of a sample or PVD produced ones demand a different treatment because the oxide covered aluminum surface is amorphous. Interesting research approaches will be done by polarization modulation infrared reflection absorption spectroscopy (PM-IRRAS), quartz crystal microweighing (QCM), and cross-sections. Techniques, like x-ray photoelectron spectroscopy (XPS) or Time-of-Flight secondary ion mass spectroscopy (ToF-SIMS), are able to deal with both single crystalline samples on the one hand and amorphous oxides. In the end, the combination of both approaches will give

## 1. Introduction

a deeper understanding of the investigated fields.

The presented research starts in chapter 4 introducing results about the adsorption kinetics. Tailoring of oxide chemistry on aluminum by means of low pressure water and argon plasma surface modification was performed to influence the kinetics of the self-organization process of ODPA monolayers. The plasma induced surface chemistry was studied by in-situ IRRAS. Ex-situ IRRAS and was applied for the analysis of the adsorbed SAMs.

In chapter 5 water barrier properties of self-assembled ODPA monolayers on low temperature plasma modified oxide covered aluminum oxide surfaces are analysed by means of in-situ FT-IRRAS in combination with QCM, ex-situ PM-IRRAS, and water contact angle measurements.

In chapter 6 analytical studies about the formation of ODPA and stability in competition with water on four distinct different aluminum oxide surfaces - single crystalline  $\text{Al}_2\text{O}_3(0001)$  and  $\text{Al}_2\text{O}_3(1-102)$  surfaces, native grown amorphous oxide covered aluminum and PV deposited amorphous aluminum oxide are presented. The adsorbed SAMs were investigated using an AFM, static contact angle of water, PM-IRRAS and DRIFTS.

Formation and stability of ODPA have been studied in chapter 7 on ZnAl alloy coatings with contents of aluminum between 0.5% and 55%. The alloys and the native grown oxide films were characterized by XPS, PM-IRRAS and ToF-SIMS. These methods indicate a strong dependency of formation and stability of ODPA from the surface chemistry.

The final chapter 8 will bridge the gap between experiments and theory. A systematic and comprehensive analysis of the adsorption of water monomers, small water clusters and water thin films on  $\alpha - \text{Al}_2\text{O}_3(0001)$  surfaces on the basis of density functional theory calculations is performed. In addition, temperature programmed desorption (TPD) is performed.

## 2. Fundamentals

### 2.1. Surface Chemistry of Single Crystalline Aluminum Oxide

#### 2.1.1. $\alpha - \text{Al}_2\text{O}_3(0001)$

Corundum in the bulk phase  $\text{Al}_2\text{O}_3$  has a rhombohedral symmetry and the atomic positions are usually given in terms of a hexagonal unit cell. This unit cell can be seen as a sequence of 12 aluminum layers, which are translational equivalent to each other, and six oxygen layers, with the oxygen ions in positions close to those of a hexagonal closed packed (hcp) lattice. For the six oxygen layers, alternate layers are translational equivalent, and sequential layers are equivalent only after a translation and mirroring through a plane perpendicular to the surface. Any of these 18 layers may serve as surface termination, and each of these surfaces has  $p3$  symmetry, i.e., threefold rotational axis through the aluminum ions and no mirror planes (see figure 2.1).

Since such surface contaminants can significantly alter the reactivity of this surface, the actual understanding of the  $\alpha - \text{Al}_2\text{O}_3(0001)$  surface - arguably the simplest of the alumina surfaces - even under UHV conditions, cannot be regarded as complete.

The  $\alpha - \text{Al}_2\text{O}_3(0001)$  surface has been extensively studied by both theoretical and experimental methods. Although early results were inconsistent, more recent theoretical [15] and experimental studies [16] [17] [18] indicate that the most stable surface is Al-terminated, with Al cations on octahedral sites (see figure 2.1). There is a discrepancy, however, between the theoretical estimate of surface Al cation relaxation of 70 – 80 % [15], and that determined by GIXRD [16], detailed LEED [17] and ion scattering studies [18], which is < 60 %, although the LEED studies reported an anomalously large vibrational amplitude for the surface cations.

The  $\alpha - \text{Al}_2\text{O}_3(0001)$  surface undergoes a series of reconstructions upon annealing above 1400  $K$ . The most stable structure, observed after an-

## 2. Fundamentals

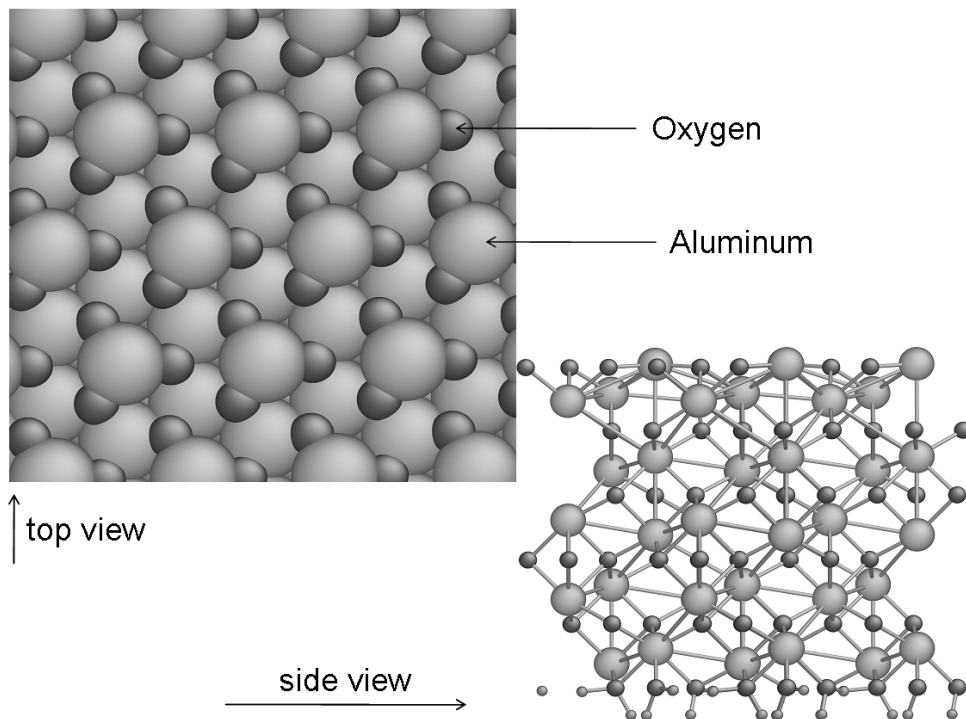


**Figure 2.1.:** Top and side view of the Al<sub>2</sub>O<sub>3</sub>(0001) surface.

nealing to 1623 K, is a  $(\sqrt{31} \times \sqrt{31}) \pm 9^\circ$  reconstruction. GIXRD [16] has been used to investigate several of these phases, and atomic resolution AFM images [22] [23] have been reported. The reconstructed surface becomes enriched in Al. The GIXRD data indicate that the outermost Al layer is disordered at the boundaries between surface domains, with evidence suggesting the second Al layer to be considerably more ordered than the outermost layer. Non-contact AFM atomic resolution imaging of the  $(\sqrt{31} \times \sqrt{31}) \pm 9^\circ$  reconstruction reveals a grid of rhombic unit cells, with a high degree of order at the center of each unit cell, and disordered regions at the boundaries between unit cells [22] [23]. The AFM data are in agreement with the GIXRD data, particularly with regard to the existence of disordered regions at the boundaries of domains which are well ordered in the center of an Al-rich surface. The disordered areas are preferential sites for reaction upon exposures to H<sub>2</sub>O/H<sub>2</sub> environments at  $P > 10^{-4}$  Pa. The nature of this chemical reaction was not determined, but the rough topography of the affected area led the authors

## 2. Fundamentals

to suggest the onset of hydroxide formation [22]. The high temperature reconstruction is one complication in investigating the reactivity of  $\alpha$ -phase alumina surfaces. Another is the fact that it is sometimes difficult to determine whether the surface is actually atomically clean. The polychromatic X-ray sources fail to completely resolve the  $\text{OH}^-$  versus  $\text{O}^{2-}$  portions of the O1s photoemission spectrum [24] [25] [26]. So it is possible that surfaces presumed to be clean in fact contained a significant concentration surface hydroxyl groups. There are inconsistencies within the literature regarding various aspects of the reactivity of the  $\alpha - \text{Al}_2\text{O}_3(0001)$  surface [25], and the possible presence of undetected surface hydroxyl groups or other impurities may be a cause of this confusion. Heating to 1400  $K$  is not sufficient to produce an atomically clean surface [28], while heating to higher temperatures can induce a surface reconstruction.

### 2.1.2. $\alpha - \text{Al}_2\text{O}_3(1 - 102)$

The  $\alpha - \text{Al}_2\text{O}_3(1 - 102)$  surface is considered an important model surface for naturally abundant alumina hydroxide phases, and therefore is of considerable interest in geochemistry and environmental chemistry studies. This surface has been investigated by AES, LEED, EELS and XPS [30]. The interaction of this surface with  $\text{H}_2\text{O}$  under UHV conditions has been studied using LEED, EELS and TPD [31]. The nucleation of gold on this surface has been investigated by RHEED and AFM [32]. This surface has also been researched by GIXRD after cleaning in UHV and exposed to  $\text{H}_2\text{O}$  at partial pressures ranging from UHV to ambient conditions [33].

Two types of LEED patterns are observed, a  $(1 \times 1)$  and a  $(2 \times 1)$  reconstruction [30] [31]. There is some controversy concerning the exact nature both the  $(1 \times 1)$  surface and the  $(2 \times 1)$  reconstruction. A rigorous cycle of Ar-ion sputtering and annealing in UHV results in the formation of the  $(2 \times 1)$  surface, which is not removed by exposure to  $\text{H}_2\text{O}$  at 300  $K$  under UHV conditions, but is removed by electron bombardment of the OH layer, leaving the  $(1 \times 1)$  [31]. This would suggest that the  $(1 \times 1)$  surface is O-terminated, in agreement with the bulk terminated structure (see figure 2.2). Surfaces prepared by extensive annealing in air and in partial pressures of  $\text{O}_2$  also yielded a  $(1 \times 1)$  LEED pattern [33]. In a separate study [32], annealing to 1100  $K$  in UHV produced a  $(1 \times 1)$

## 2. Fundamentals

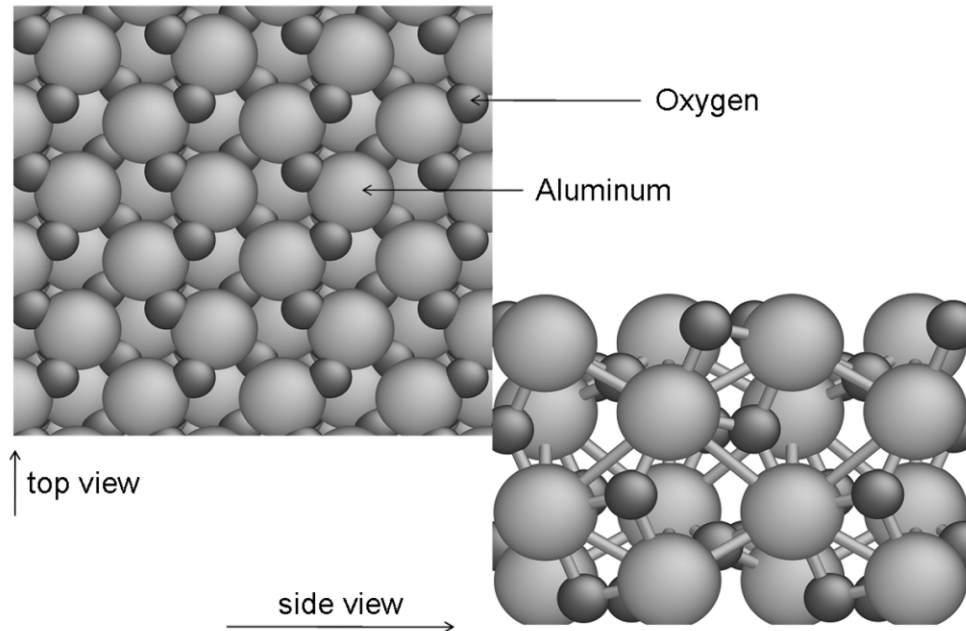


**Figure 2.2.:** Top and side view of the  $\text{Al}_2\text{O}_3(1-102)$  surface.

surface, and subsequent annealing to 2000  $K$  resulted in the  $(2 \times 1)$  reconstruction. These results are consistent with a  $(2 \times 1)$  reconstruction being produced by O removal from the  $(1 \times 1)$  surface, although the  $(2 \times 1)$  phase can also be produced at lower temperatures in UHV [31]. GIXRD studies [33] report two possible  $(1 \times 1)$  O-terminated relaxed structures with equally good fits to the data. The structure with zero Al occupancy of the second layer, however, has more reasonable Al – O bond distances.

## 2.2. Surface Chemistry of Aluminum and Alloys

### 2.2.1. Native Grown Aluminum Oxide Films

Native oxide aluminum grows according to the Cabrera-Mott mechanism [43]. The mechanism proposes the setting up of a strong electric field across the initial oxide layer due to the contact potential difference between the metal at the metal-oxide interface and the adsorbed  $O_2$  at the oxide-gas interface (see figure 2.3). According to Mott it was this strong electric field that assisted the metal ions in moving through the oxide via interstitial sites and forming the oxide at the oxide-gas interface.

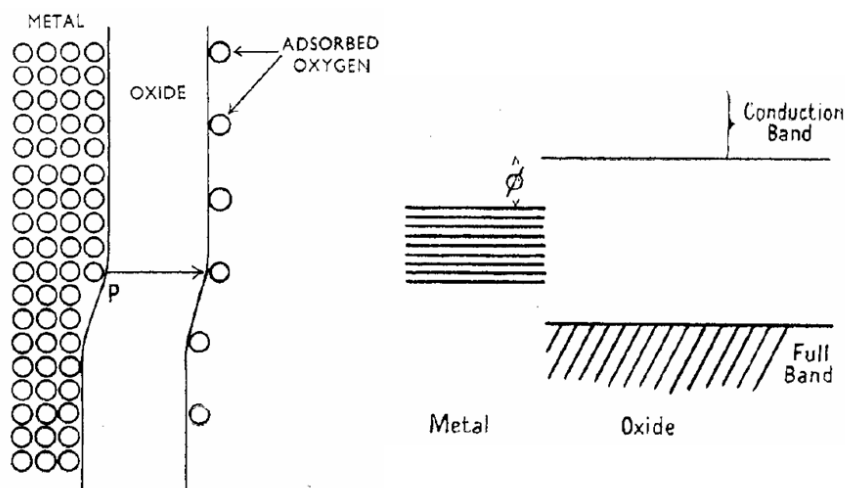


**Figure 2.3.:** Showing the mechanism by which ions leave a metal and pass through oxide layer, according to [43].

In case of plasma modification adsorbed oxygen and hydroxide ions produced by electron-impact induced chemistry at the interface between the oxide and the plasma volume, induce a strong electric field across the oxide layer that drives ionic migration through the film. Depending on the specific mobilities of the species, either  $Al^{3+}$  ions move towards the oxide surface or oxygen ions towards the metal/oxide interface. The transport of electrons is considered to be independent of the ionic motion and fast in comparison to the ion transport [139].

## 2. Fundamentals

### 2.2.2. ZnAl Alloy Coatings

ZnAl Alloy coatings are mainly used to improve the corrosion resistance of steel by two methods, barrier protection and galvanic protection. In barrier protection, the coating, which separates the steel from the corrosion environment, will first corrode before the corrosive environment reaches the steel. In galvanic protection, the coating is less noble to iron at ambient conditions, and will sacrificially corrode to protect the substrate steel, even if some of the steel is exposed as cut edges or scratches in the coating. Typical processing methods used in producing ZnAl alloy coatings include hot-dip galvanizing (HDG), thermal spraying and electrodeposition. These fundamentals will be limited to HDG, i.e. the immersion of a steel strip in a liquid bath of ZnAl alloys, by batch or continuous processing. The continuous process is more advantageous for coiled products such as sheet, wire and tube, whereas the batch process is normally used for bulk products [27].

Considerable work has been reported about ZnAl alloy coating properties and has recently been reviewed [36]. The important properties that concern the use of ZnAl alloy coatings are primarily corrosion resistance and adhesion. However, it should be noted that the corrosion resistance of any coating can drastically change depending upon the specific corrosion environment and whether the coating is welded, contains a paint system or is deformed, and the extent to which galvanic protection is required for nearby uncoated areas [37].

#### **Zn-0.5%-Al (HDG)**

Aluminum is probably the most important alloying element added to the HDG bath, with different levels required in order to produce different properties in the bath [34]. Levels of 0.005 – 0.02 *wt %* are added to brighten the initial coating surface. The effect is related to the formation of a continuous aluminum oxide layer on the coating surface that inhibits further oxidation by acting as a protective barrier. This effect is also responsible for the reduced atmospheric oxidation of the zinc bath. HDG is the most prominent procedure to coat flat steel with a protective zinc alloy coating. During the galvanizing process, the steel strip moves through hot zinc melt containing small additional amounts of aluminum. The latter process leads to the formation of a very thin FeAl-alloy layer at the interface between steel and the metal alloy coating, thus preventing

## 2. Fundamentals

the formation of brittle FeZn-alloys. The addition of aluminum to the zinc melt also leads to the formation of a native aluminum rich oxyhydroxide passive layer on the surface during cooling of the liquid zinc alloy coating. Such Al-surface enrichments have been detected and reported in various papers [39].

### **Zn-5%-Al (Galfan)**

Galfan is a Zn + 5% Al alloy coating, which is near the eutectic point in the ZnAl equilibrium phase diagram [50]. Two compositions have been reported based on additions to the eutectic composition: small composition metal additions containing lanthanum and cerium contents up to about 0.5 % [35] and additions of 0.5 % magnesium [36]. These additions are made to improve the wettability and fluidity of the molten bath without affecting the corrosion resistance of the coating [35]. The microstructure of Galfan is characterized by a two-phase structure, a zinc-rich proeutectic phase surrounded by an eutectic phase consisting of aluminum and zinc. However, the microstructure can be varied depending upon cooling rate [38].

### **Zn-55%-Al (Galvalume)**

Galvalume is a Zn + 55% Al alloy coating containing about 1.6% Si added for the purpose of preventing an exothermic reaction at the coating overlay substrate steel interface [48]. During the coating process an interfacial FeAlZn intermetallic alloy layer forms at the interface between the steel substrate and the overlay coating [49]. The surface of the Galvalume coating contains characteristic spangles that consist of aluminum dendrites with a clearly measurable dendrite arm spacing (DAS). In cross-sections (which will be discussed more detailed later), three features of the coating are defined: The coating contains aluminum dendrites, Zn-rich interdendritic regions and a fine dispersion of Si particles. The Al dendrites were reported to contain approximately 18 *wt* % Zn and up to 1.8 *wt* % Si which is in good agreement with the ZnAl phase diagram [50].

## 2.3. Self-Assembled Monolayer Formation

### 2.3.1. General Overview

All surface treatments based on conversion have in common that they form up a closed macroscopic oxide or hydroxide film, which usually has amorphous characteristics and protects the surface as a barrier from aggressive ions. The adhesion of polymer coatings on such surfaces will be caused mainly by the morphology of the layers and van der Waals interactions. A chemical linking of the polymer layer to the conversion layer was postulated only one time in the case of zirconium oxide [64].

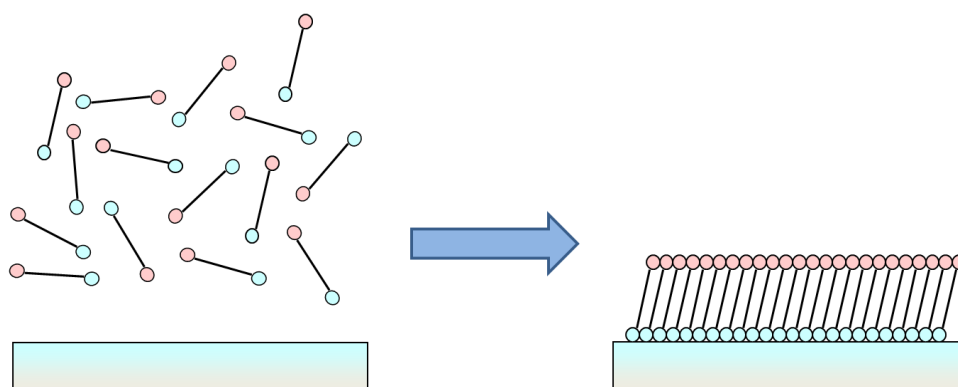


**Figure 2.4.:** Self-assembly of amphiphilic adsorbates onto a solid surface.

A more novel concept of surface treatment is the chemical modification of surfaces by ultra-thin films of organic compounds. These attempts are made by the adsorption of surface-active substances, a functionalization of the surface to reach the modified substrate properties. Novel applications for such ultra-thin layers are in the areas of sensor technology, optics and the corrosion protection. These are extreme cases in order to modify a surface with only a single molecule capable of an organic substance. In figure 2.4 the principle of such a coating is shown schematically. During the adsorption the headgroups of the molecules interact with the surface. Through interaction of the carbon frameworks of the single molecules an orderly, densely packed structure will form, which is characterized by the angle between the molecular axes and the surface normals. A second

## 2. Fundamentals

functional group, in which in the simplest case a methyl group, in the end determines the properties of the modified surface.

### 2.3.2. Mechanisms and Kinetics of Self-Assembled Monolayers Formation

The concept of molecular bonding agents is substrate-specific and has to be continued in a way that the outward-pointing end of the molecules will be able to build up covalent chemical bonds to subsequently applied coatings to stabilize the adhesion promoter molecules directly to the phase boundary between metal and polymer layer. Monomolecular layers of surface-active molecules in principle can be generated in two ways. In the Langmuir-Blodgett technique, the surface-active molecules are in a special apparatus on a liquid surface [65]. The substrate to be coated is then pulled out of the liquid through the liquid film, which will form highly ordered layers in the end. The method is far too expensive to be used for complex structures to be coated and this way in industry. The second process leading to monomolecular layers can be obtained as self-organization (see figure 2.5). This is generally the spontaneous adsorption of surface-active substances on metal and oxide covered substrates mostly from organic solutions and leading to a highly ordered structure. In practice, SAMs can be achieved by simple immersion of the substrate in a solution of surface-active substance. In contrast to the Langmuir-Blodgett technique the procedure is only applied to molecules whose functional headgroups have a very high affinity to the substrate surface, and hence to the spontaneous adsorption capacity. Furthermore the process of the self-organization in terms of a uniform orientation of all molecules on the surface is usually only possible for a minimum length of about four carbon units in the alkyl chain. A typical molecule capable of self-assembling has a polar headgroup and an alkyl chain (ODPA). During the chemisorption of the headgroups on a metal surface, the adsorption energy is the driving force for a full coverage on the surface. The adsorption consists in the displacement of solvent molecules from the surface. With increasing coverage, the long chain molecules form a more dense pack together. They have, however, still enough agility between their relative positions to change slightly. In this way, over time a highly ordered crystalline pack can be build up.

2. Fundamentals

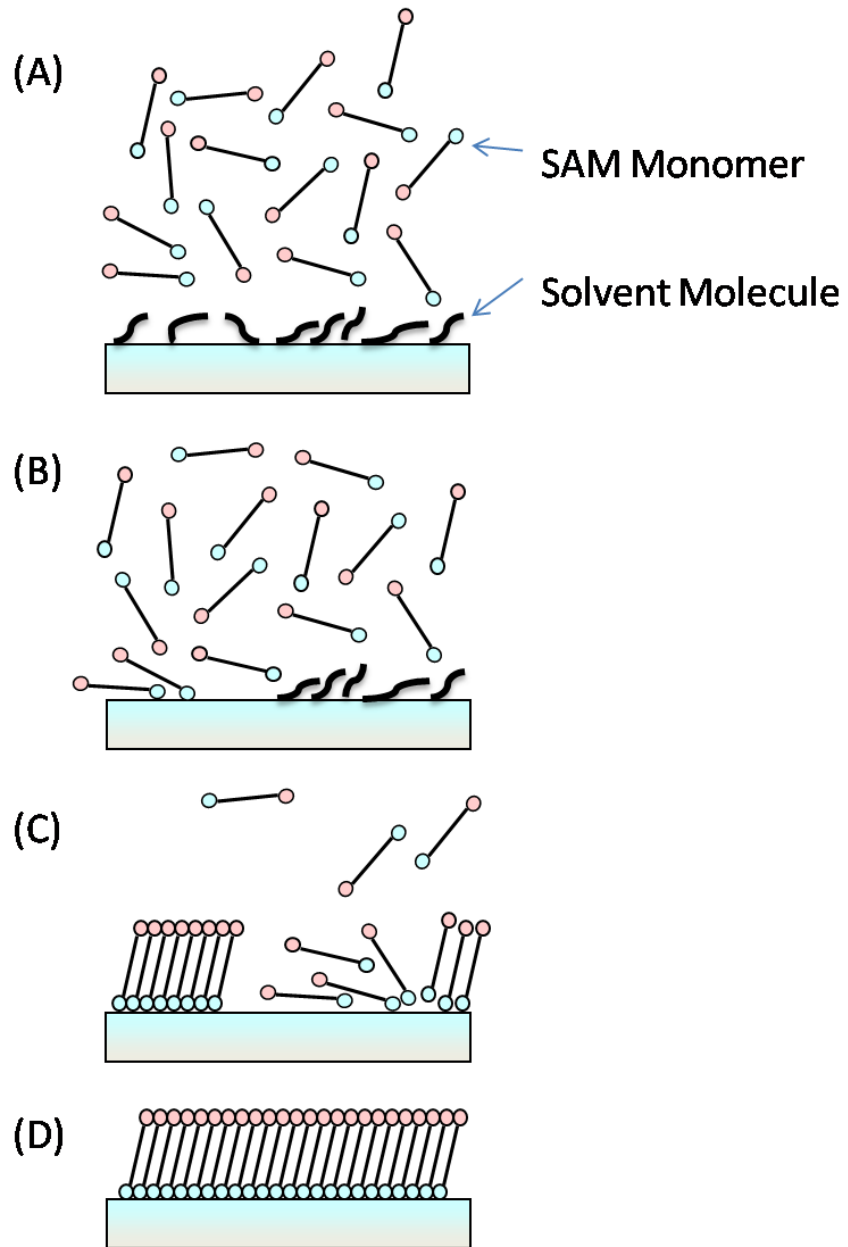


**Figure 2.5.:** Illustration of the self organization process, according to [40].

## 2. Fundamentals

### 2.3.3. Self-Assembled Monolayers on Metal Surfaces

The study of SAMs on metal surfaces is undoubtedly in the modification of gold surfaces with thiols most advanced. An even incomplete overview of the immense number of publications on this topic would be beyond the scope of this work. Both the efforts to characterize the molecular structure of the SAMs as well as all attempts by the chemical modification of metal surface by suitable functional end groups on the phase boundary between film and ambient atmosphere with all the related applications in sensors and nonlinear optics started on this field [66] [67] [68]. But only few works deal with this issue from the viewpoint of corrosion protection and surface treatment of metals. One work of Rohwerder and de Weldige noted that with the self-organization of thiols on gold electrodes as a function of potential employees and, in particular defect structures of the films and the electrochemical, the reduction of oxygen is changing [69]. Furthermore the behavior of the modified surfaces oxygen reduction was investigated [69]. The work aimed to gain insights into the applications of thiols on iron surfaces. In addition to gold surfaces, the self-organization of thiols also on copper and silver is known. Here, possible applications of thiols are the corrosion protection, especially in the field of microelectronics [70]. Films of the thiols inhibit the oxygen reduction on copper surfaces considerably. It was shown that the kinetics of oxygen reduction varies with the chain length of the connections [48]. Industrially already used are thiols for corrosion protection on silver contacts in electronic components during transportation and storage, especially in marine areas.

### 2.3.4. Self-Assembled Monolayers on Oxide Covered Surfaces

The state of research in the field of ultrathin organic compounds on oxide covered surfaces such as aluminum or zinc is far from being as advanced as in the case of the metals. This is mainly due to the difficulty of preparing a defined substrate surface, which does not change in its chemical composition and microstructure during the adsorption and thus permits the formation of an ordered molecular structure and its spectroscopic characterization. Most are located on the surface of metals or alloys, oxide layers, which are in the treatment solution, either dissolve or coagulate and thus disturb the process of self-assembly. Unlike the adsorption on

## 2. Fundamentals

metals, one SAM on an oxide covered metal can slow down the corrosion processes but usually not completely suppress it. An application of such coatings for surface treatment is therefore only in conjunction with an additional polymer coating.

The extremely high bond strength of the iron-sulfur binding provided the motivation for the study of thiols on iron surfaces. Since the accessibility of the thiols on an iron oxide surface required in the work of Volmer and Reinartz [71] that the native oxide layer was removed by cathodic polarization by several times and exchange in the electrolyte containing the thiols as an organic phase were adsorbed. In this way they got multilayers, which in aqueous solutions showed a protective effect, but in alcoholic solutions were not resistant. The protective effect here is not based on a stable monolayer, but on the barrier properties of a macroscopic hydrophobic thiols. In-situ studies in UHV on extremely thin metallic iron on thiols showed that although the stability of the oxide surface towards the oxidation by the presence of thiols actually increased, the protective effect extends. However, it was by far not sufficient to generate in air stable monomolecular films. The connection of organic molecules and the ordering of ultrathin films are possible on oxide surfaces, however, are other functional groups as required for adsorption on metal oxide surfaces.

One of the major classes of layer formation on oxide covered surfaces often already been studied is the alkoxy silane [72]. They differ from the other surface-active compounds by the fact that when applied from organic solutions initially by hydrolysis the corresponding silanol which must be formed will react with the surface hydroxide in a condensation reaction can enter into each other simultaneously. A polymeric network on the surface of the metal can be built up this way. Their wide application in practice, however, failed mainly due to the need for their application in organic media, the difficulty of controlling the hydrolysis under industrial conditions and the high cost of chemicals used.

The possible applications of SAMs on aluminum or aluminum alloy surfaces as described in the present work have so far hardly been studied. Most works dealing with the molecular structure of thin aluminum films to employ were on flat surfaces from the gas phase or deposited on aluminum single crystals carried out. Allara and Nuzzo [39] studied the adsorption behavior of carboxylic acids to oxidized aluminum surfaces with the aid of IR spectroscopy and provided a detailed analysis of spec-

## 2. *Fundamentals*

troscopic data on thickness and structure of the formed films. They investigated carboxylic acids with a chain length of C12 to C22 and proposed a structure for the SAMs, where the headgroup is in anionic form and the backbone has all-trans conformation of methylene units and a tilt of  $12^\circ$  to the surface normals.

Also for the adsorption of phosphonic acids on aluminum oxide an ionic interactions is proposed [54] [55] [56]. Ramsi and Templeton investigated the interaction of phosphonic acid with aluminum oxide surfaces in such systems with the help of IETS [73]. In addition, several works, which deal specifically with the surface treatment used phosphonic acid in combination with aluminum materials from the viewpoint of corrosion protection.

## 2.4. Adhesion Promoting Organophosphonic Acids

An adhesion promoter is applied to a substrate to improve the adhesion of a coating to the substrate (see figure 2.6). There are many reasons for delamination such as low adhesion due to incompatible surfaces, surface contamination, and void formation during curing.

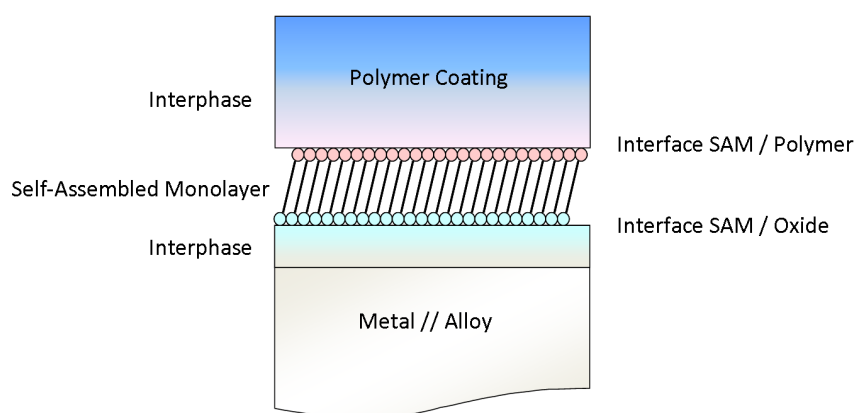


**Figure 2.6.:** The zone called interphase is mainly determined by the interactions between the substrate and the coating. These interactions can be enhanced in many cases by introducing an adhesion promoter.

In this study self-organizing phosphonic acid molecules were investigated on aluminum oxide surfaces to improve the adhesion.

### 2.4.1. Binding to the Oxide Surface

With regard to the use of molecules as self-assembled monolayers, primarily aliphatic molecules with 12 to 18 methyl groups were investigated. The headgroups were varied, initially in the field of well-researched systems, such as thiols, carboxylic acids and silanes. Additionally functional groups were selected, from which an interaction with aluminum was reported already. In most cases phosphonic acids, but also amine

## 2. Fundamentals

molecules were used for adhesion promotion. All adhesion promoter candidates have been subjected to a flotation experiment. In a first step, all molecules should adsorb on a powder of aluminum by solution self-assembly. Subsequently, the powder and solutions were separated by filtration. If the powder now has a complete and stable hydrophobic shell of the molecules, it was able to float on water. The number of floating powder grains and the time to until they dive as a selection criterion was investigated. It was found that phosphonic acid has the best characteristics for aluminum.

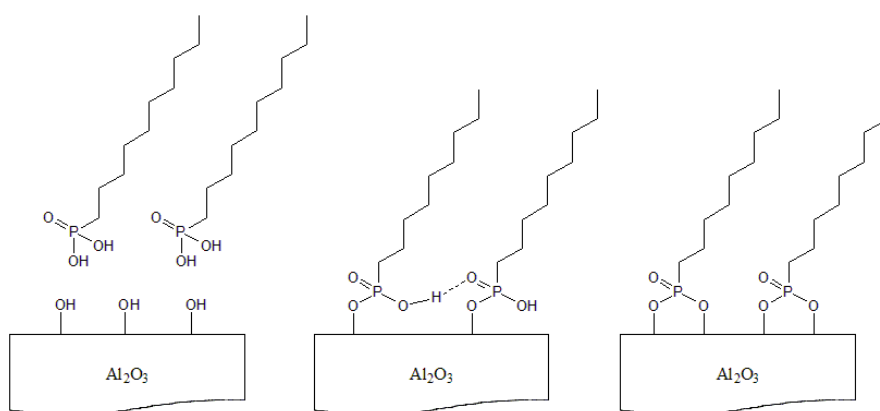


**Figure 2.7.:** Binding models developed in the literature.

Maège et al. [54] were the first to bring up the acid-base binding model for the phosphonic acid/aluminum oxide interface in the year 1998 (left side). The driving force was the formation of a surface salt. This approach was further investigated and developed by Gawalt et al. (center) [55] and Hoque et al. (right side) [56] to an mono- and bidentate binding model (see figure 2.7). According to Gawalt et al. the phosphonate group stretchings in the IR indicate a bidentate coordination mode of the phosphonate to the surface.

### 2.4.2. Coupling Reactions at the Interface Self-Assembled Monolayer/Polymer

The stability of a coating/adhesion promoter/oxide interface is decisively determined by the type of attractive forces between functional groups of coating and oxide surface as well as between coating and adhesion promoter. If organic molecules adhere via hydrogen bonds, an incorporation

## 2. Fundamentals

of water to the organic/oxide interface leads to wet de-adhesion. The substrate/coating interface stability can be increased by donor/acceptor attraction of the Brönsted or Lewis type due to their higher binding energy. If the polymeric top coat structure does not permit such interaction, an adhesion promoting molecule can improve the adherence. Aminopropylphosphonic acid (APPA) for example is mixed to epoxy-amine coatings, enriches at the polymer/oxide interface during hardening and increases the adhesion force between organic layer and substrate. For a defined interface structure and in terms of economical use it is tried to reduce the amount of adhesion promoter to a single monolayer, which should also specifically bond to the coating [57]. Pahnke et al. presented a technique to specifically connect a benzophenone derivative to a hydrocarbon chain on the one hand and adhering it by a phosphonic acid anchor to an aluminum surface on the other hand [58]. For industrial applications a promising corrosion protective system involves the choice of a suitable substrate material, a compatible adhesion promoter and tailored coating. Besides the stability of the monolayer/oxide interface a highly stable monolayer/top coat interface is important, but was not specifically investigated so far.

## 2.5. Ab initio Simulations

Atoms and molecules, and the solids and in this work which are considered systems, are many-particle systems, which require a quantum mechanical description. However, for many-particle systems, no analytical solutions of the Schrödinger equation can be found. This chapter will begin with some approximations and methods described by the free parameters (*ab initio*) calculations in this work.

### 2.5.1. The Schrödinger Equation

The Schrödinger equation describes the wavefunction of a particle [59]:

$$\left\{ \frac{-\hbar^2}{8\pi^2m} \nabla^2 + V \right\} \Psi(\vec{r}, t) = \frac{i\hbar}{2\pi} \frac{\partial \Psi(\vec{r}, t)}{\partial t} \quad (2.1)$$

In this equation,  $\Psi$  is the wavefunction,  $m$  is the mass of the particle,  $\hbar$  is Planck's constant, and  $V$  is the potential field in which the particle is moving. The operator  $\nabla$  is equivalent to partial differentiation with respect to  $x$ ,  $y$  and  $z$  componets:

$$\nabla = \frac{\partial}{\partial x} \hat{i} + \frac{\partial}{\partial y} \hat{j} + \frac{\partial}{\partial z} \hat{k} \quad (2.2)$$

The product of  $\Psi$  with its complex conjugate  $\Psi^*$  is interpreted as the propability distribution of the particle. The Schrödinger equation for a collection of particles like a molecule is very similar. In this case,  $\Psi$  would be a function of the coordinates of all the particles in the system as well as  $t$ . The energy and many other properties of the particle can be obtained by solving the Schrödinger equation for  $\Psi$ , subject to the appropriate boundary conditions. Many different wavefunctions are solutions to it, corresponding to different stationary states of the system. If  $V$  is not a function of time, the Schrödinger equation can be simplified using the mathematical technique known as separation of variables. If we write the wavefunction as the product of a spatial function and a time function:

$$\Psi(\vec{r}, t) = \Psi(\vec{r}) \tau(t) \quad (2.3)$$

and then substitute these two new functions into equation (2.1), we will obtain two equations, one of which depends on the position of the particle

## 2. Fundamentals

independent of the time and the other of which is a function of time alone. For the problems in which we are interested, this separation is valid, and we focus entirely on the familiar time independent Schrödinger equation:

$$E\Psi(\vec{r}) = H\Psi(\vec{r}) \quad (2.4)$$

where  $E$  is energy of the particle, and  $H$  is the Hamiltonian operator, equal to:

$$H = \frac{-\hbar^2}{8\pi^2m}\nabla^2 + V \quad (2.5)$$

The various solutions to equation (2.4) correspond to different stationary states of the particle or molecule. The one with the lowest energy is called the ground state. Equation (2.4) is a non-relativistic description of the system which is not valid when the velocities of particles approach the speed of light. Thus, it does not give an accurate description of the core electrons in large nuclei.

### 2.5.2. The Molecular Hamiltonian

For a molecular system,  $\Psi$  is a function of the positions of the electrons and the nuclei within the molecule, which we will designate as  $r$  and  $R$ , respectively. These symbols are a shorthand for the set of component vectors describing the position of each particle. We will use subscripted versions of them to denote the vector corresponding to a particular electron or nucleus:  $r$  and  $R$ . Note that electrons are treated individually, while each nucleus is treated as an aggregate; the component nucleons are not treated individually.

The Hamiltonian is made up of kinetic and potential energy terms:

$$H = T + V \quad (2.6)$$

The kinetic energy is summation of  $\nabla^2$  over all the particles in the molecule:

$$T = -\frac{\hbar^2}{8\pi^2} \sum_k \frac{1}{m_k} \left( \frac{\partial^2}{\partial x_k^2} + \frac{\partial^2}{\partial y_k^2} + \frac{\partial^2}{\partial z_k^2} \right) \quad (2.7)$$

The potential energy component is the Coulomb repulsion between each pair of charged entities (treating each atomic nucleus as a single charged

## 2. Fundamentals

mass):

$$V = \frac{1}{4\pi\epsilon_0} \sum_j \sum_{k < j} \frac{e_j e_k}{\Delta r_{jk}} \quad (2.8)$$

where  $\Delta r_{jk}$  is the distance between the two particles, and  $e_j$  and  $e_k$  are the charges on the particles  $j$  and  $k$ . For an electron, the charge is  $-e$ , while for a nucleus the charge is  $Z \times e$ , where  $Z$  is the atomic number for that atom.

$$V = \frac{1}{4\pi\epsilon_0} \cdot \left[ - \sum_i^{elec} \sum_I^{nucl} \left( \frac{Z_I e^2}{\Delta r_{jI}} \right) + \sum_i^{elec} \sum_{j < i}^{elec} \left( \frac{e^2}{\Delta r_{ij}} \right) + \sum_I^{nucl} \sum_{J < I}^{nucl} \left( \frac{Z_I Z_J e^2}{\Delta R_{IJ}} \right) \right] \quad (2.9)$$

The first term corresponds to electron-nuclear attraction, the second to electron-electron repulsion, and the third to nuclear-nuclear repulsion.

### 2.5.3. The Born-Oppenheimer Approximation

The Born-Oppenheimer approximation is the first of several approximations used to simplify the solution of the Schrödinger equation [60]. It simplifies the general molecular problem by separating nuclear and electronic motions. This approximation is reasonable since the mass of a typical nucleus is thousands of times greater than that of an electron. The nuclei move very slow with respect to the electrons, and the electrons react essentially instantaneously to changes in nuclear positions. Thus, the electron distribution within a molecular system depends on the positions of the nuclei, and not on their velocities. Put another way, the nuclei look fixed to the electrons, and electronic motion can be described as occurring in a field of fixed nuclei. The full Hamiltonian for the molecular system can be written as:

$$H = T^{elec}(\vec{r}) + T^{nucl}(\vec{R}) \quad (2.10)$$

$$+ V^{nucl-elec}(\vec{R}, \vec{r}) + V^{elec-elec}(\vec{r}) + V^{nucl}(\vec{R})$$

The Born-Oppenheimer approximation allows the two parts of the problem to be solved independently, so we can construct an electronic Hamiltonian which neglects the kinetic energy term for the nuclei:

## 2. Fundamentals

$$H^{elec} = -\frac{1}{2} \sum_i^{elec} \left( \frac{\partial^2}{\partial x_i^2} + \frac{\partial^2}{\partial y_i^2} + \frac{\partial^2}{\partial z_i^2} \right) \quad (2.11)$$

$$- \sum_i^{elec} \sum_I^{nucl} \left( \frac{Z_I}{|\vec{R}_I - \vec{r}_i|} \right) + \sum_i^{elec} \sum_{j<i}^{elec} \left( \frac{1}{|\vec{r}_i - \vec{r}_j|} \right) + \sum_I^{nucl} \sum_{J<I}^{nucl} \left( \frac{Z_I Z_J}{|\vec{R}_I - \vec{R}_J|} \right)$$

This Hamiltonian is used in the Schrödinger equation describing the motion of electrons in the field of fixed nuclei:

$$H^{elec} \Psi^{elec}(\vec{r}, \vec{R}) = E^{eff}(\vec{R}) \Psi^{elec}(\vec{r}, \vec{R}) \quad (2.12)$$

Solving this equation for the electronic wavefunction will produce the effective nuclear potential function. It depends on the nuclear coordinates of the system and describes the potential energy surface (PES) of the system. For a given set of nuclear coordinates, this corresponds to the total energy predicted by a single point energy calculation, although such calculations, of course, do not solve this equation exactly. One possibly approximation method used to solve it will be discussed in the next section of this introduction. Accordingly,  $E^{eff}$  is also used as the effective potential for the nuclear Hamiltonian:

$$H^{nucl} = T^{nucl}(\vec{R}) + E^{eff}(\vec{R}) \quad (2.13)$$

This Hamiltonian is used in the Schrödinger equation for nuclear motion, describing the vibrational, rotational and translational states of the nuclei. Solving the nuclear Schrödinger equation is necessary for predicting the vibrational spectra of molecules.

### 2.5.4. Density Functional Theory

Density Functional Theory (DFT) methods ultimately derive from quantum mechanics research from the 1920's, especially the Thomas-Fermi-Dirac model, and from Slater's fundamental work in quantum chemistry in the 1950's [63]. The DFT approach is based upon a strategy of modeling electron correlation via general functionals of the electron density. Such methods owe their modern origins to the Hohenberg-Kohn theorem, published in 1964, which demonstrated the existence of a unique func-

## 2. Fundamentals

tional which determines the ground state energy and density exactly [61]. The theorem does not provide the form of this functional, however. Following on the work of Kohn and Sham [62], the approximate functionals employed by current DFT methods partition the electronic energy into several terms:

$$E = E^T + E^V + E^J + E^{XC} \quad (2.14)$$

where  $E^T$  is the kinetic energy term arising from the motion of the electrons,  $E^V$  includes terms describing the potential energy of the nuclear-electron attraction and of the repulsion between pairs of nuclei,  $E^J$  is the electron-electron repulsion term, and  $E^{XC}$  is the exchange-correlation term and includes the remaining part of the electron-electron interactions. Beyond the Born-Oppenheimer approximation and the density functional theory further simplifications can be introduced to the total energy calculations. The most important ones are the pseudopotential theory to model the electron-ion interactions, supercells to model systems with non-periodic geometries, and iterative minimization techniques to relax the electronic coordinates. The essential concepts will be reviewed very briefly.

### 2.5.5. Pseudopotential Theory

The pseudopotential theory allows one to replace the strong electron ion potential with a much weaker potential - called pseudopotential - that describes all the salient features of a valence electron moving through the solid, including relativistic effects [59]. Thus the original solid is now replaced by pseudo valence electrons and pseudo ion cores. These pseudo electrons experience exactly the same potential outside the core region as the original electrons but have a much weaker potential inside the core region. The fact that the potential is weaker is crucial, however, because it makes the solution of the Schrödinger equation much simpler by allowing expansion of the wave functions in a relatively small set of plane waves. Use of plane waves as basis functions makes the accurate and systematic study of complex, low-symmetry configurations of atoms much more tractable.

### 2.5.6. Supercell Approximation

The supercell approximation allows one to deal with non-periodic configurations of atoms within the framework of Bloch's theorem [59]. One simply constructs a large unit cell containing the configuration in question and repeats it periodically throughout space (see figure 2.8). By studying the properties of these system for larger and larger unit cells, one can gauge the importance of the induced periodicity and systematically filter it out.

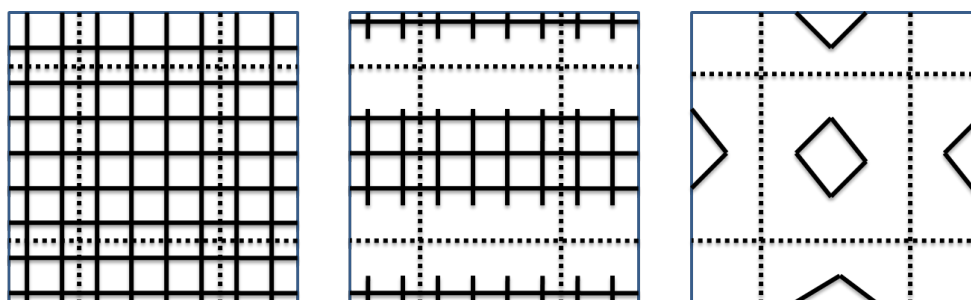


**Figure 2.8.:** Schematic illustration of a supercell geometry. On the left hand a bulk solid is illustrated. In the middle one can see a model for a surface of a bulk solid and on the right hand a geometry for a molecule is shown. The supercell is the area enclosed by the dashed lines; according to [74].

### 2.5.7. Iterative Minimization

New iterative diagonalization approaches can be used to minimize the total energy functional [59]. These are much more efficient than the traditional diagonalization methods. New methods allow expedient calculation of ionic forces and total energies and significantly raise the level of modern total energy calculations. The procedure requires an initial guess for the electronic charge density, from which the Hartree potential and the exchange-correlation potential can be calculated. The Hamiltonian matrices for each of the  $k$  points included in the calculation must be constructed and diagonalized to obtain the Kohn-Sham eigenstates. These eigenstates will normally generate a different charge density from the one originally used to construct the electronic potentials, and hence a

## 2. *Fundamentals*

new set of Hamiltonian matrices must be constructed using the new electronic potentials. The eigenstates of the new Hamiltonians are obtained, and the process is repeated until the solutions are self-consistent.

## 3. Experimental

In this section the details of all used experimental and theoretical tools are given. For each technique the used experimental setup is described and possible sources of errors will be commented.

### 3.1. Chemicals and Materials

If not indicated otherwise, all chemicals were of p.a. grade (analytical reagent grade) and were used as supplied without any further purification. The following chemicals and materials were used within this work: Supplier VWR-International: 85 %  $\text{H}_3\text{PO}_4$ , 30 % water-based  $\text{H}_2\text{O}_2$  solution, 27 % water-based  $\text{NH}_3$  solution, Ethanol absolute. Supplier Alfa Aesar: 99 % Octadecylphosphonic acid (ODPA). Other suppliers: > 99.99 % Gold (Goodfellow), > 99.99 % Aluminum (Goodfellow), > 99.99% Chrom (Goodfellow), HDG (Dortmunder Oberflächencentrum, (DOC)), Galfan (DOC), Galvalume (DOC),  $\text{Al}_2\text{O}_3(0001)$  (Mateck) and  $\text{Al}_2\text{O}_3(1 - 102)$  (Mateck).

### 3.2. Fourier Transform Infrared Spectroscopy

A continuous light source emits infrared radiation, which is weakened by the sample frequency-dependent (corresponding to the excited molecular vibrations). The rest of the incoming radiation is registered in a detector and electronically converted into an IR-spectrum.

#### 3.2.1. Polarization Modulation Infrared Reflection Absorption Spectroscopy

In the infrared investigation of thin films and monolayers on metal surfaces it is well known that at high angles of incidence, near the grazing angle, enhanced absorbance of the reflected p-polarized light are achieved.

### 3. Experimental

In contrast, nearly no absorbance is observed with s-polarized light. This disparity in absorbance intensities offers the possibility to obtain the differential reflectance spectrum of the surface species  $\Delta R/R$  by polarization modulation. It is important to have only polarization insensitive

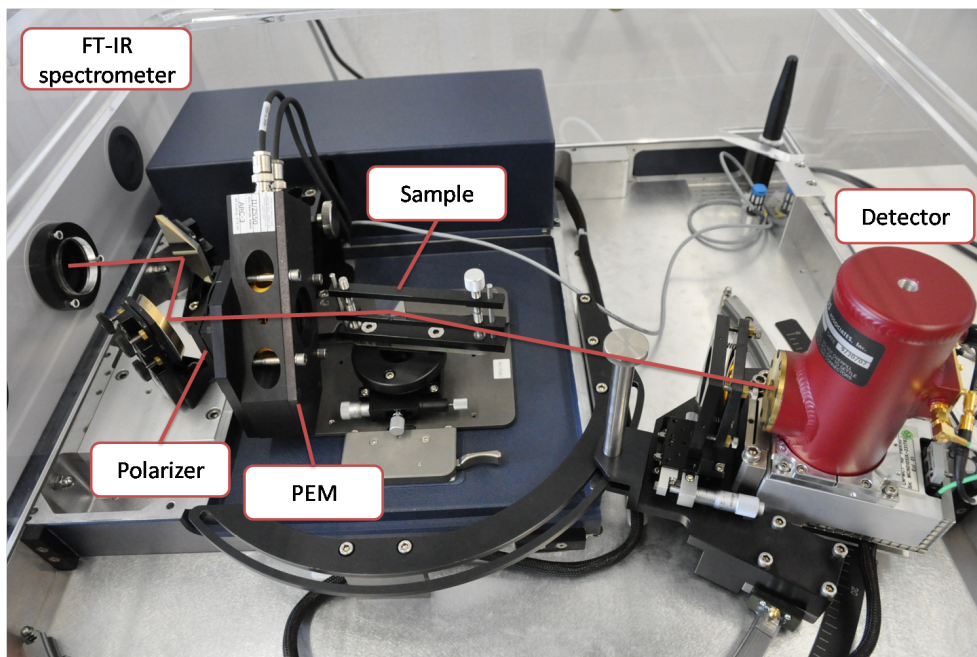


**Figure 3.1.:** Optical setup block diagram for PM-IRRAS measurements.

elements behind the sample (see figure 3.1), since any instrumental polarization differences will appear in the PM-IRRAS spectrum. To obtain the differential spectrum, the detector signal is processed by a specialized electronics that generates the average and the difference interferogram required for the PM-IRRAS spectrum. These two signals are digitized simultaneously with the A/D converter of the FT-IR spectrometer.

If ZnSe is stressed by compression or stretching, the material becomes birefringent. That means different linear polarizations of light have slightly different speeds of light when passing through the material. The stress amplitude can be selected so that the photoelastic modulator (PEM) acts like a 'half-wave' plate. That means the plane of linear polarized light is rotated by  $90^\circ$ , after passing through the PEM crystal. The stress, applied to the PEM crystal, is sinusoidally modulated. Thus,

### 3. Experimental

the state of polarization is modulated, too. The effective polarization modulation frequency of the light is twice the mechanical oscillation frequency of the PEM crystal. The (PEM) modulates the infrared beam by rotating the polarization of the light sinusoidally at the frequency of the birefringence modulation introduced mechanically in a ZnSe crystal [76] [77]. If a monochromatic incident infrared beam that is linearly polarized  $45^\circ$  to the strain axis is passed through the modulator, the intensity of output light is given by:

$$I(t) = [I_p + I_s + (I_p - I_s) \cdot \cos(\Phi_0 \cdot \cos(\gamma \cdot t))] / 2 \quad (3.1)$$

$I_p$ : polarization of the light beam prior to the PEM, experimentally set to p-polarized light, i.e. polarized so that the electric field is parallel to the plane of incidence.

$I_s$ : s-polarized light, i.e. polarized so that the electric field is perpendicular to the plane of incidence.

$\cos(\gamma \cdot t)$ : modulation frequency of the PEM

$\Phi_0$ : constant that depends linearly on the amplitude of mechanical modulation of the PEM

This modulation is found as a high frequency modulation on the classical interferogram, detected at the detector element. These two frequencies, interferometer and PEM modulation, are separated by the dedicated electronics. The low frequency signal is the average interferogram  $I_A$  :

$$I_A(\delta) = (I_p + I_s)/2 \quad (3.2)$$

The high frequency signal, typically  $100 \text{ kHz}$  modulation signal which is demodulated by an external lock-in amplifier and send back to the electronics, represents the difference interferogram  $I_D$  :

$$I_D(\delta) = (I_p - I_s)/2 \quad (3.3)$$

After the Fourier Transformation, the average and the difference spectra are calculated:

$$I_A(\omega) = (I_p + I_s)/2 \quad (3.4)$$

$$I_D(\omega) = (I_p - I_s)/2 \quad (3.5)$$

### 3. Experimental

The differential reflectance spectrum is defined as:

$$\Delta R/R = [I_D(\omega)/I_A(\omega)] \quad (3.6)$$

Because of the different reflectivity of s- and p-polarized infrared radiation at a metal surface the differential spectrum is multiplied by the Bessel function, i.e. a background is obtained:

$$\Delta R/R = J_2(\phi_0) \cdot I_D/I_A \quad (3.7)$$

The amplitude of the mechanical excitation of the PEM crystal defines the points of the zero crossings of the Bessel function. The appropriate setting for the amplitude depends on the experiment, i.e. on the wavelength region of interest.

#### 3.2.2. Spectra Refinement

1.) The software calculates the raw PM-IRRAS curve:

$$\Delta R/R_{(raw)} = [I_D/I_A] \quad (3.8)$$

2.) The amplification factor of the lock-in amplifier has to be removed:

$$\Delta R/R = (\Delta R/R_{(raw)})/f_A \quad (3.9)$$

3.) Removal of the background:

The background curve  $\Delta R/R_{(back)}$  can be fitted by a polynomial algorithm or it can be obtained by the measurement of a clean metal substrate. However, the differential reflectivity spectrum is ratioed against the normalized background curve to result in the normalized differential reflectivity spectrum.

$$\Delta R/R_{(norm)} = (\Delta R/R) / ([\Delta R/R_{(back)}] \cdot R_{max}) \quad (3.10)$$

In comparison to the infrared transmission spectroscopy, especially the investigation of ultrathin ( $< 5 \text{ nm}$ ) layers is not described adequate by macroscopic dielectric constants. During measurements this leads to a shift and change of the full width at half maximum of the peaks.

### 3. Experimental

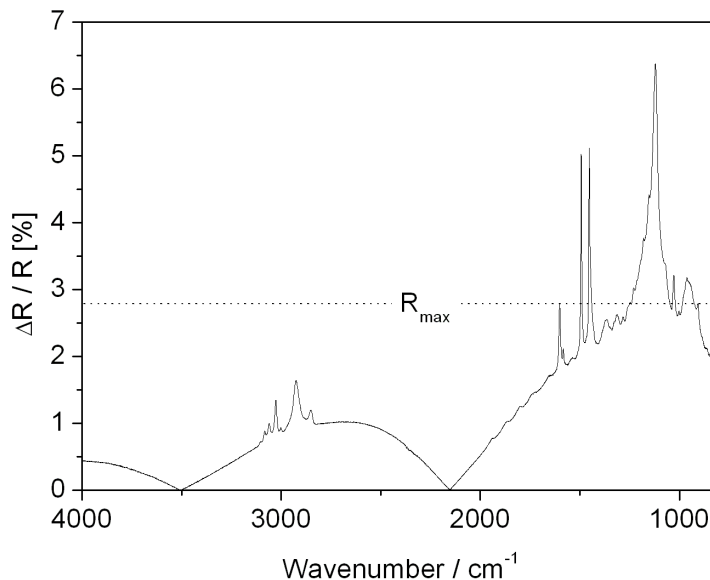


**Figure 3.2.:** Differential reflectance spectrum of [12-(4-Benzophenone)-dodecyl] phosphonic acid monolayer on oxide covered aluminum. Spectral features of the sample and Bessel function background.

#### 3.2.3. Diffuse Reflectance Infrared Fourier Transform Spectroscopy

With the help of DRIFTS rough powder or solid state samples can be examined directly, without further sample preparation. The diffuse radiation is reflected by a reflecting ball again and focused in the detector bulk. The radiation is then detected, integrated and electronically converted into an IR-spectrum.

The DRIFTS offers some advantages over the IRRAS. First, it allows the investigation of strongly scattering or absorbing samples. Second, it provides high signal intensity, since the spectral information of many particles is used. Therefore, even low intensity bands are measured. The most important advantage, however, is that no sample preparation is required, why powder or even single crystals of metal oxides can be measured directly. In comparison to the PM-IRRAS, the DRIFTS does not suffer from optical shifts because of ultrathin layers.

### 3. Experimental

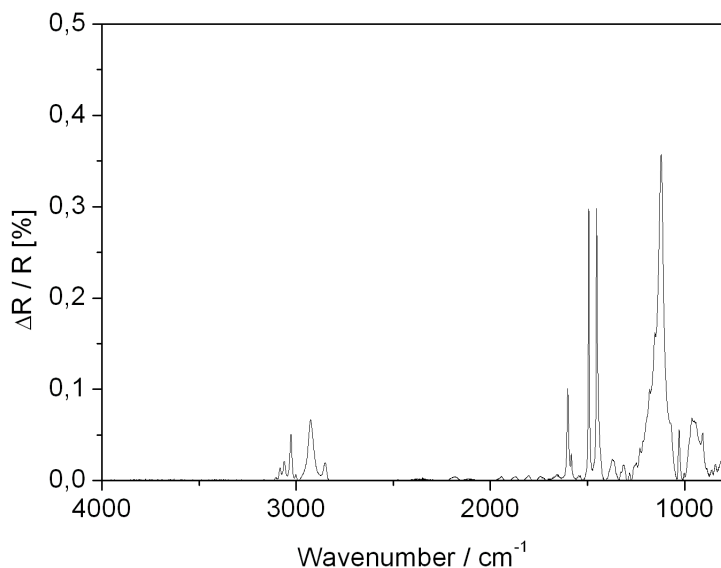


**Figure 3.3.:** Differential reflectance spectrum of [12-(4-Benzophenone)-dodecyl] phosphonic acid monolayer on oxide covered aluminum. Spectral features of the sample after removal of the background.

## 3.3. Quartz Crystal Microweighing

If a layer is applied on a quartz crystal excited to shear vibrations, then the resonance frequency of the quartz crystal changes due to an enlargement of the swinging mass. Since frequency change of swinging quartz can be measured very exactly, a very sensitive measuring method results for the weighing of thin layers. Mass allocations of the layer and frequency change are each other proportional. The proportionality constant can be calculated from the resonance frequency of the swinging quartz crystal, so that a calibration is void during the layer weighing with QCM. The accuracy of the QCM is primarily limited by the temperature dependence of the quartz resonance frequency [82].

### 3.3.1. Quartz Crystal Microweighing in Gas-Phase

The quartz crystal microbalance is an extremely sensitive sensor capable of measuring mass changes in the  $ng/cm^2$  range with a wide dynamic range extending into the  $g/cm^2$  range. Sauerbrey was the first to rec-

### 3. Experimental

ognize the potential usefulness of the technology and demonstrate the extremely sensitive nature of these piezoelectric devices towards mass changes at the surface of the QCM electrodes [86]. The results of his work are embodied in the Sauerbrey equation, which relates the mass change per unit area at the QCM electrode surface to the observed change in oscillation frequency of the crystal:

$$\Delta f = -C_f \cdot \Delta m \quad (3.11)$$

$\Delta f$ : observed frequency change in  $Hz$

$C_f$ : sensitivity factor of the crystal in  $Hz/(ng \cdot cm^2)$

( $0.056 Hz/(ng \cdot cm^2)$  for a 5  $MHz$  crystal @ 20 °C)

( $0.081 Hz/(ng \cdot cm^2)$  for a 6  $MHz$  crystal @ 20 °C)

( $0.181 Hz/(ng \cdot cm^2)$  for a 9  $MHz$  crystal @ 20 °C)

$\Delta m$ : change in mass per unit area, in  $g/cm^2$

The minimum detectable mass change is typically a few  $ng/cm^2$  and limited by the noise specifications of the crystal oscillator and the resolution of the equipment used to measure frequency shifts. The Sauerbrey equation relies on a sensitivity factor,  $C_f$ , which is a fundamental property of the QCM crystal. Thus, in theory, the QCM mass sensor does not require calibration. This ability to calculate the mass sensitivity from first principles is obviously a very attractive feature of these devices. However, it is very important to notice, that the Sauerbrey equation is only strictly applicable to uniform, thin-film deposits originating from a low pressure (i.e. vacuum) gas environment [78] [79]. Thick deposits and operation in liquid environments or in contact with lossy films, relies on the use of more complex equations relating the frequency shifts to mass loading, and often requires calibration of the setup for accurate results. Several articles have been published on simple ways to calibrate the mass sensitivity of QCMs for electrochemical applications [81] and for vacuum thin-film deposition processes [84], and some useful calibration guidelines are also described herein. Many studies have shown that the crystal's sensitivity is approximately Gaussian. The maximum sensitivity is in the center of the crystal and it tapers off towards the edge of the active area [85] [86]. The mass sensitivity distribution has also been shown to become slightly more confined to the electrode region as the mass loading is increased.

The temperature coefficient of quartz crystals is normally specified in

### 3. Experimental

units of parts per million per degree of temperature change. A one part per million change in frequency of the sensing crystal corresponds to an indicated thickness change of approximately  $7.4 \text{ \AA}$  for a material with a density of  $1.0 \text{ g/cm}^3$ . For aluminum with a density of  $2.7 \text{ g/cm}^3$ , this is equivalent to approximately  $2.7 \text{ \AA}$ . This intrinsic dependence of resonance frequency of a sensor crystal on temperature is generally small in experiments in gas phase when operating at or near its "turn-around-point". The "turn-around-point" is where the temperature coefficient of the crystal is zero.

The Quartz Crystals utilised for all experiments were standard AT-cut, 1-inch diameter crystals for use in liquid applications. The AT-cut quartz is chosen for its superior mechanical and piezoelectric properties, and the angle of cut can be adjusted to obtain a zero temperature coefficient at a desired operating temperature. The 1-inch diameter was chosen to allow enough distance between the active area of the crystal and the mounting o-ring. This improves the overall stability of the crystal by reducing the frequency changes due to mounting stress. The Maxtek's 1-inch crystal electrode patterns configuration enables both electrical contacts to be made on the backside of the crystal allowing measurement in conductive liquids. The oversized front electrode ( $1/2$  inch in diameter as opposed to the  $1/4$  inch diameter rear electrode) was chosen to ensure a more consistence deposition across the active area of the crystal. The exposed area of the front electrode is  $0.212 \text{ inch}$  ( $137 \text{ mm}^2$ ), but the active oscillation region (displacement area) is limited to the overlapping area of the front and rear electrodes ( $0.053 \text{ inch}$  or  $34.19 \text{ mm}^2$ ).

#### 3.3.2. Quartz Crystal Microweighing in Liquids

In the following experiments the crystal holder is in direct contact with the sensor crystal and the experiment environment. Thus, care must be taken to ensure its cleanliness eliminating any contaminants that may react with the crystal or the experiment media. QCMs have been used as gas-phase mass detectors with lossless films for many years. However, recently their applications have been extended to liquids and with viscoelastic deposits. In these cases, both frequency and series resonance resistance of the quartz crystal are important to completely characterize the material and/or the liquid in contact with the crystal electrode. The development of QCM systems for use in liquids opened a new world of

### 3. Experimental

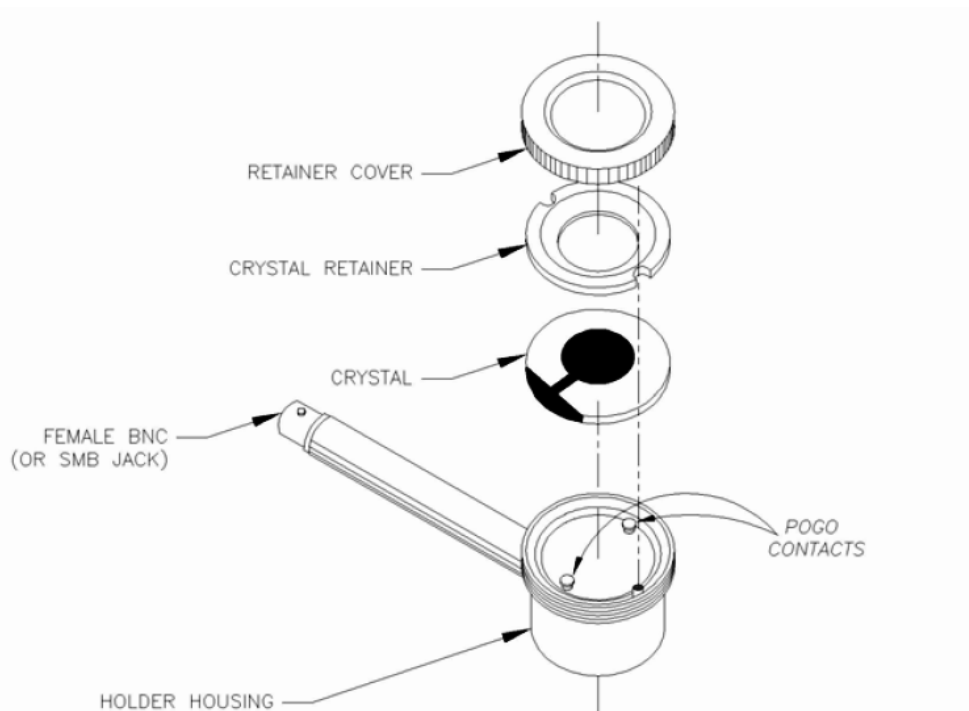


**Figure 3.4.:** QCM-holder for liquid media.[87]

applications, including electrochemistry and micro-rheology. More recent developments have focused on tailoring electrode surface chemistry (i.e. specialized polymer coatings) so that these devices can be applied as discriminating mass detectors for many applications including: specific gas detection, environmental monitoring, biosensing and basic surface molecule interaction studies. When the QCM comes in contact with a liquid, there is a decrease in frequency that is dependent upon the viscosity and density of the liquid. Kanazawa's solution for the change in resonant frequency of the crystal due to liquid loading is shown in the following equation

$$\Delta f = -f_q^{\frac{3}{2}} \sqrt{\frac{\eta_L \cdot \rho_L}{\pi \cdot \mu_q \cdot \rho_q}}. \quad (3.12)$$

Liquid loading also dampens the resonant oscillation of the crystal causing an increase in series resonance resistance,  $R$ , of the crystal.  $\Delta f$  and  $\Delta R$  measurements are both routinely used as independent indicators of mass loading and viscosity at the crystal-liquid interface of the QCM res-

### 3. Experimental

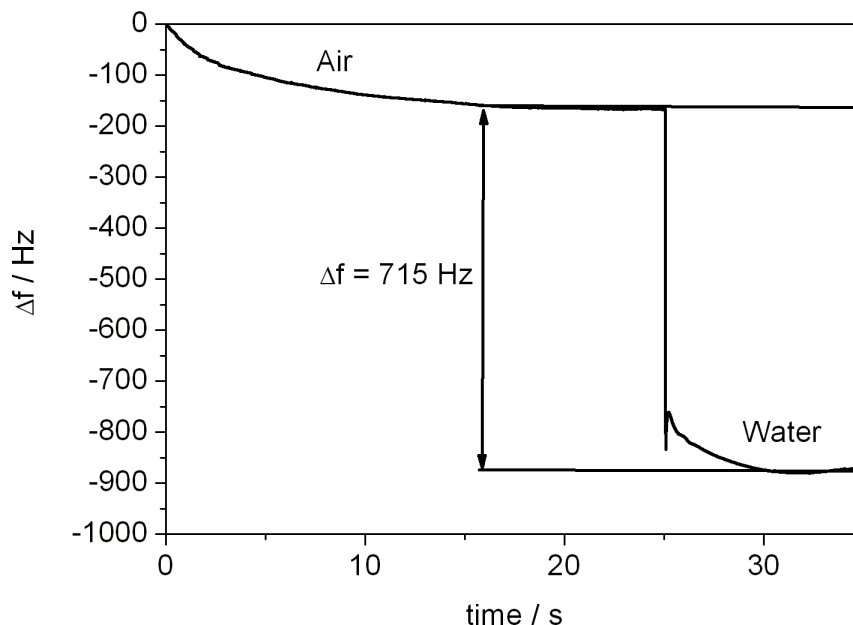


**Figure 3.5.:** Change in resonant frequency of the crystal due to liquid loading.

onator during chemical and electrochemical depositions in solution. For example, moving the crystal from air to pure water @  $20^\circ\text{C}$ , Kanazawa's equation predicts a decrease in  $f$  of  $714 \text{ Hz}$ , respectively. This value is in agreement with the results observed with an QCM using a  $5 \text{ MHz}$ , 1-inch diameter, polished, gold coated mounted on a Maxtek Crystal Holder (see figure 3.5). Note that pure water @  $20^\circ\text{C}$  has a density of  $998.2 \text{ kg/m}^3$ , and a viscosity of  $1.002 @ 10^{-3} \text{ N/m}^2$ . Excellent agreements between the frequency equations and the experimental results have been proved, making the QCM an excellent tool for the evaluation of fluid properties. Application examples include in-situ monitoring of lubricant and petroleum properties. The tight correspondence between theory and the QCM is clearly illustrated in figure 3.5, respectively. Note that some of the discrepancy in the frequency curve could arise from an error in estimating the active electrode area.

Studies have shown that electrode surface roughness can cause large apparent mass loadings due to the liquid that is trapped within pores at the crystal surface. Maxtek's crystals are optically polished to  $50 \text{ \AA}$  average surface roughness to minimize this effect. Polished crystals are required

### 3. Experimental

to obtain good agreement between theory and measurement during liquid immersion experiments. Polished crystals are also required to obtain measurements reproducibility from crystal to crystal.

## 3.4. Contact Angle Measurements

Contact angle measurements were made to demonstrate the relationship between the properties and chemistry of a surface. Wettability (ability of a fluid to cover a surface) varies with both the completeness of the monolayer and its degree of order. Wettability also varies with the polarity of the monolayer surface functional groups.

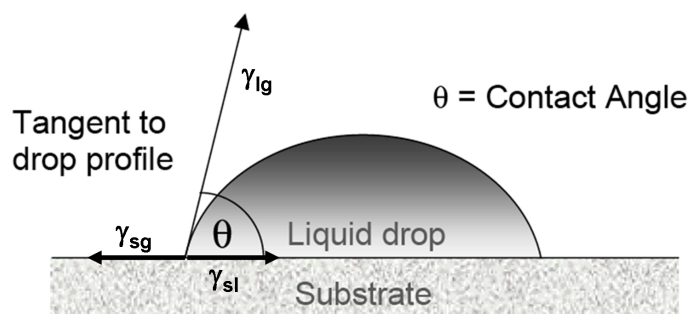


**Figure 3.6.:** Schematic draw of a liquid/solid interface with the contact angle  $\theta$ .

To determine the surface free energy of the monolayers by measuring contact angles as a function of surface tension, a measurement of a series of liquids is necessary. The Young equation gives the following relation

$$\gamma_{sg} = \gamma_{sl} + \gamma_{lg} \cos\theta \quad (3.13)$$

where  $\gamma$  is the surface tension which can be thought of as the energy required to create a unit area of an interface. If the energy required to create the solid-liquid (sl) interface is greater than that required for creation of a solid-gas (sg) interface, then the contact angle  $\theta$  will be lower than  $90^\circ$ . In other words, the liquid will spread over the surface to maximize the solid-liquid interfacial area (see figure 3.6).

The surface energy as well as dispersive and polar fractions of the surface free energy were determined from the static contact angles of water, formamide and di-iodomethane following the approach of Owens [88]

### 3. Experimental

assuming that the total free energy at a surface can be considered as a sum of contributions.

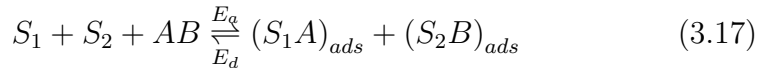
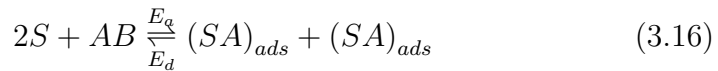
## 3.5. Thermal Desorption Spectroscopy

Temperature-programmed desorption (TPD) techniques are well suited methods for the determination of kinetic and thermodynamic parameters of desorption processes or decomposition reactions. A sample is heated with a temperature program  $\beta(t) = dT/dt$  (with the temperature  $T$  usually being a linear function of the time  $t$ ) and the partial pressures of atoms and molecules evolving from the sample are measured, e.g. by mass spectrometry. When experiments are performed using well-defined surfaces of single crystalline samples in a continuously pumped UHV chamber (see figure 3.7) then this experimental technique is often also referred to as thermal desorption spectroscopy (TDS).

TPD is an UHV based technique for the determination of the adsorption parameters of a system: the number of different adsorption states with one particular adsorbate, the adsorbed mass on the surface, the order of the desorption reaction and their activation energy. The initial step of surface processes is the adsorption creating a chemical bond, which can be expressed in a chemical equilibrium as



where  $S$  is the surface site of the adsorption,  $A$  is the adsorbing atom or molecule and  $(SA)_{ads}$  is the adsorbate. Taking dissociative adsorption (molecules: A-A and A-B) into account the adsorption equilibrium is reached if



where  $S_1$  and  $S_2$  are different surface sites of the adsorption. With the reactions (3.14) to (3.17) indicated are the activation energy of the adsorption  $E_a$  and the activation energy of the desorption  $E_d$ . When a

### 3. Experimental

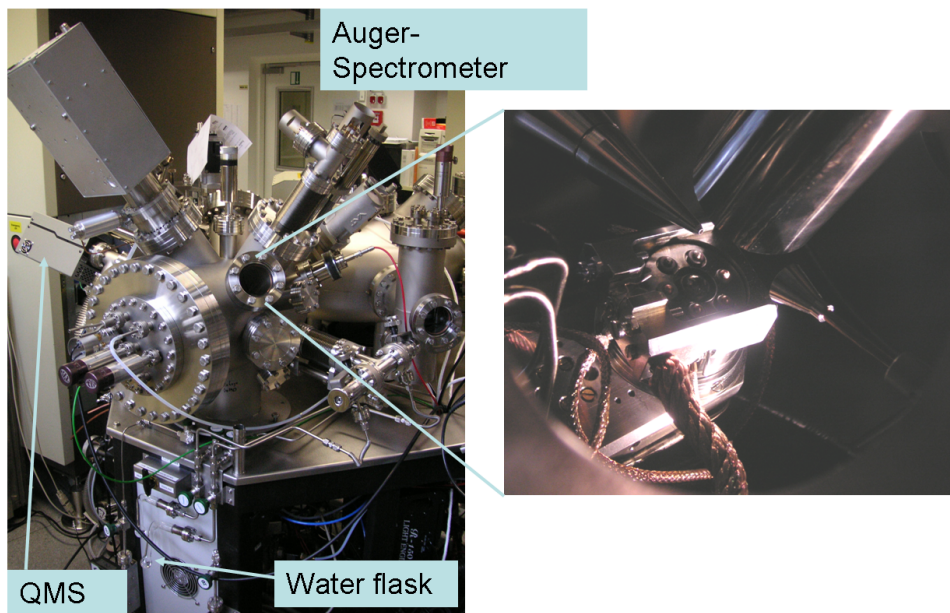


**Figure 3.7.:** On the left hand the complete UHV chamber and on the right hand the manipulator, the conus leading to the QMS, the AES and the head of the dosing system can be seen. This experimental configuration allows adsorption, thermal desorption in-situ, and furthermore the confirmation of the surface state by AES.

particle approaches to the surface and is finally adsorbed, the following condition is applied:

$$|E_d| = |E_{ads}| + |E_a| \quad (3.18)$$

This equation can be simplified for the case of non-activated adsorption to

$$|E_d| = |E_{ads}| \quad (3.19)$$

with  $E_{ads}$  being the adsorption energy. Non dissociative adsorption reactions are also not activated; dissociative reactions can be both activated and not activated. In general adsorption reactions are exothermic. Adsorption reactions mean a decrease of entropy for gaseous adsorbents. The total gain of free energy can be calculated from the Gibbs-Helmholtz

### 3. Experimental

equation for the free standard reaction enthalpy of adsorption

$$\Delta G_{ads} = \Delta H_{ads} - \Delta S_{ads} \cdot T \quad (3.20)$$

where  $S_{ads}$  is the entropy difference between the right and the left side of equation (3.14). The adsorption entropy is negative because the number of the degrees of freedom is smaller in the adsorbate than in the gas. Therefore  $G_{ads}$  can be only negative if  $H_{ads}$  is negative.

For the description of a desorption reaction the surface coverage  $\Theta$  is used as a measure for the surface coverage of the adsorbate and the negative derivative as reaction rate  $\nu_d$

$$\nu_d = -\dot{\Theta} = -\frac{\partial \Theta}{\partial t} \quad (3.21)$$

The desorption reaction of  $n$ -th order is described as

$$\dot{\Theta} = -k_0 \cdot \Theta^n \quad (3.22)$$

where is the  $n$ -th exponential of the coverage as function of the time  $t$ , is the variation of coverage with time,  $k_0$  is the reaction constant and  $n$  is the order of the desorption reaction. The order  $n = 1$  is assumed for the non-associative and  $n = 2$  for associative desorption. The reaction constant is given by the Arrhenius equation

$$k_0 = k_d \cdot \exp\left(-\frac{E_d}{R \cdot T}\right) \quad (3.23)$$

where  $k_d$  is the pre-exponential factor,  $R$  is the gas constant and  $T$  is the temperature of the adsorbate. From equations (3.22) and (3.23) we receive as differential equation for desorption of  $n$ -th order

$$\dot{\Theta} = -k_d \cdot \Theta^n \cdot \exp\left(-\frac{E_d}{R \cdot T}\right). \quad (3.24)$$

## 3.6. Time-of-Flight Secondary Ion Mass Spectroscopy

A primary ion beam of  $\text{Ga}^+$  strikes the sample causing the emission of secondary ions characteristic for the composition of the sample surface.

### 3. Experimental

The primary beam is a Gallium ion beam emitted by a so-called Liquid Metal Ion Gun (LMIG). The secondary ions are accelerated and focused by a lens system (not entirely represented) before reaching the spectrometer. The kinetic energy of an ion of mass  $m$  and charge  $z \cdot e$  after acceleration by an extraction voltage  $V_0$  is:

$$E_k = \frac{1}{2}mv^2 = |z| \cdot e \cdot V_0 \quad (3.25)$$

The spectrometer (or secondary ion optics) is constituted of an electrostatic analyzers and a secondary ion detector (dual micro-channel plate detector). Since the primary ion beam is pulsed, the time  $t$  required for an ion to hit the detector plate is measured (so-called Time-of-Flight: ToF). If  $L_0$  is the effective length of the spectrometer,  $t$  is given by:

$$t = \frac{L_0}{v} = L_0 \cdot \sqrt{\frac{m}{2 \cdot |z| \cdot e \cdot V_0}} = C \cdot \sqrt{\frac{m}{|z|}} \quad (3.26)$$

So, the mass separation (resolution) is given by the separation of the times of flight between sample and detector for the various secondary ions. Besides, the arrival position of a secondary ion on the micro-channel detector plate is correlated to the emission point at the sample surface. This allows lateral resolution and chemical mapping. Since a given acceleration voltage extracts secondary ions of a given polarity, two acquisitions, one for the positive ions, one for the negative ones, are required to obtain a complete ionic image of the surface.

## 3.7. X-ray Photoelectron Spectroscopy

The kinetic energy of electrons extracted from a sample at given photonic energy is an element specific parameter. The analytical x-ray energy balance can be expressed as:

$$E_B = h \cdot \nu - E_{kin} - e_\phi \quad (3.27)$$

$E_B$  = binding energy [eV]

$h \cdot \nu$  = photoelectric energy of the x-ray [eV]

$E_{kin}$  = kinetic energy of the photoelectrons [eV]

$e_\phi$  = electronic work function [eV]

### 3. Experimental

The XPS may be used for the identification of chemical bondings and the contained elements. It is also a quantitative analyse technique for the elemental distribution near surface layers ( $2 - 5 \text{ nm}$ ).

The depth information of the method is limited by the mean free path of electrons. For a normal metal this length goes from 2 to 5 nm, which is very small compared to the penetration of the x-rays (1 to 10  $\mu\text{m}$ ). It is clear that only electrons from the material can be measured by the detector. The intensity contribution decreases with increasing depth exponentially.

There are two kinds of spectra obtained: Survey and detail spectrum. The first one serves as global information about the investigated sample and obtains intensities as function of the binding energies. Measured for the entire area the existing elements can be detected qualitatively.

For a quantitative analysis of a particular element one can perform detail spectra. Here, a higher resolution in the binding energy of each element is given. The XPS method can also include information about the chemical state of an element. A bound element (such as a metal in a metal oxide) has a different charge distribution in comparison to non bonded or pure state, with a shift in the XPS binding energy. Thus, for example different oxidation states can be distinguished [118].

## 3.8. Scanning Electron Microscopy

The scanning electron microscope (SEM) allows imaging and analyzing sample surfaces by rastering a surface with a beam of high-energy electrons (usually between  $2 - 25 \text{ keV}$ ) in a grid-like scan-pattern. Varieties of interactions of the electrons with the surface produce different types of signals that contain information of the surface topography, chemical composition and crystalline structure. The interaction of the incoming electrons with the surface first of all leads to elastic back-scattering of the electrons. Moreover, incoming electrons can cause other electrons to leave the sample surface as so-called secondary electrons. The photo electric emission of electrons from core-levels leads to the emission of characteristic x-rays and auger electrons due to electronic relaxation processes. All of these types of signals generated by the electron beam can be analyzed by conventional SEMs. The standard imaging mode, secondary electron imaging, allows to obtain extremely high-resolution images of the sam-

### 3. *Experimental*

ple surfaces revealing details down to  $nm$  in size. Also back-scattered electrons enable an evaluation of the surface topography. Moreover, the analysis of the diffraction pattern of the back-scattered electrons (Electron Backscatter Diffraction, EBSD) allows obtaining crystallographic information from samples with the SEM. The diffraction pattern can e.g. be used to analyze the orientation of individual grains on polycrystalline samples. Auger electrons and emitted x-rays are of course sensitive to the emitting element and can therefore be used for an analysis of the chemical composition [75].

# 4. Application of Quartz Crystal Microweighing to Adsorption Kinetics of Self-Assembled Monolayers

## 4.1. Introduction

The aim of this work was to investigate the native and plasma modified oxide covered films of aluminum as a starting point for the adsorption of different organic monolayers. In the literature, these compounds are described as self-organizing on oxide covered aluminum surfaces. In addition, they have a protective effect against corrosion on the Al-surface. They replace conventional micrometer thick conversion layers. Before starting this work, however, only little knowledge existed about the kinetics of adsorption of the Organophosphonate.

Pahnke and Rhe showed the effective coupling of benzophenone functionalized organophosphonates to oxide covered aluminum surfaces which opens the way of adhesion promotion to organic layers via a photochemical reaction [92]. Wapner and Grundmeier applied aminopropylphosphonic acids as short chain adhesion promoting molecules on aluminum alloy surfaces from dilute aqueous solutions and from a liquid adhesive film and showed excellent filiform corrosion resistance [93]. It is generally accepted that surface hydroxyl groups promote the adsorption of the organophosphonate and that the adhesion of the phosphonate group is based on an acid-base interaction. The driving force is assumed to be the formation of a surface salt as already described for long-chain carboxylic acids by Allara et al. [94] and recently by van den Brand et al. [95] [96]. Alexander et al. showed that an aluminum surface under atmospheric conditions is covered by a thin pseudo-boehmite layer. The passive film consists of the two main phases  $-\text{Al}_2\text{O}_3$  and  $-\text{Al}(\text{O})\text{OH}$ .

## 4. Adsorption Kinetics

The hydroxide to oxide ratio could be characterized by means of XPS and appropriate curve fitting [97]. Low temperature plasma processes at reduced or atmospheric pressure recently are of high interest for the adjustment of surface chemistry on metals and polymers. In extremely short times the material surface can be changed in its chemical composition [1] [2]. Grundmeier et al. illustrated how oxide covered iron and zinc can be modified with regard to their surface chemistry and oxide thickness [3] [4]. However, for most technical applications the time required to form a functional monolayer is crucial for the applicability in a process chain, the most challenging being continuous lines for aluminum sheet surface technology. Adsorption times of few tens of seconds would allow the integration of self-assembly processes even in these high speed technologies. Up to now the study of the kinetics of adsorption was not in the focus of the investigations. Most monolayers were formed within hours of immersion in solution.

In this work, for the first time quartz crystal microweighing was used as a method to determine the kinetics of adsorption and the density of hydroxides on Al-modified surfaces. Moreover, it should be examined to what extent a modification of the oxides in a glow discharge can influence the kinetics of adsorption. As a second point of interest the dependence of the adsorption kinetics of the concentration has been investigated. This way a novel combined process for Al-materials has been developed. The aluminum was deposited in the form of a 250 nm thick layer on a quartz crystal. The adsorption of the monolayers was done from dilute ethanol solution. With the help of quartz crystal microweighing a time resolved in-situ investigation of the layer adsorption was achieved. Individual results were determined by FTIR spectroscopy under grazing incidence.

## 4.2. Experimental

### 4.2.1. Sample Preparation

For the here presented studies the aluminum samples were prepared by PVD. Aluminum layers were deposited on commercial gold coated quartz crystals (Maxtek,  $\varnothing = 1$  inch) for the in-situ IRRAS measurements and subsequent study of adsorption kinetics of phosphonic acids by a QCM. Samples were coated with 250 nm aluminum layer (Al 99.99%) using

#### 4. Adsorption Kinetics

electron beam evaporation (Univex 450, Leybold AG). During the evaporation the layer thickness was monitored by a QCM (Inficon XTC). Prior to aluminum film deposition the samples were thoroughly cleaned in a mixture of hydrogen peroxide and ammonia (1 : 1) for 60 minutes at 80 °C, afterwards rinsed with de-ionized water and dried in a nitrogen stream.

##### 4.2.2. Surface Chemistry

The experimental setup for the plasma modification is shown in figure 4.1 a). The sample is mounted on a holder which can be moved by a stepper motor along the chamber axis. For a uniform modification of the surface the sample was moved through the plasma zone at a constant velocity which determines the time of exposure. More detailed description of the plasma generation is given by Raacke et al. [98]. The base pressure of the chamber before flushing with the working gases was ensured to be in the range of  $10^{-4}$  mbar. The pressure of the corresponding gas atmosphere during all plasma modifications was adjusted to 0.3 mbar. Pure gases were used for the experiments, argon and hydrogen in the quality 5.0 by Air Liquid, for the water plasma modifications a closed flask with a high precision valve was filled with ultra pure water. Before using the water was frozen by dipping in liquid nitrogen and the residual gas content pumped down. For the adjustment of a defined water vapor atmosphere in the plasma chamber to 0.3 mbar the water partial pressure was fed by a fine valve and the pumping system was throttled. The gas composi-

**Table 4.1.:** Gas phase composition and relevant times of the several plasma treatments.

Gas composition	Partial pressure/mbar	Treatment time/s
Ar/H <sub>2</sub>	0.25/0.05	120
H <sub>2</sub> O	0.3	120
Ar	0.3	120

tions and relevant times during the different plasma treatments are given in table 4.1. The experimental setup for the adsorption experiments is shown in figure 4.1 b). The QCM (Maxtek, RQCM) with a resonance frequency of 5 MHz is sensitive to mass changes down to nanograms

#### 4. Adsorption Kinetics

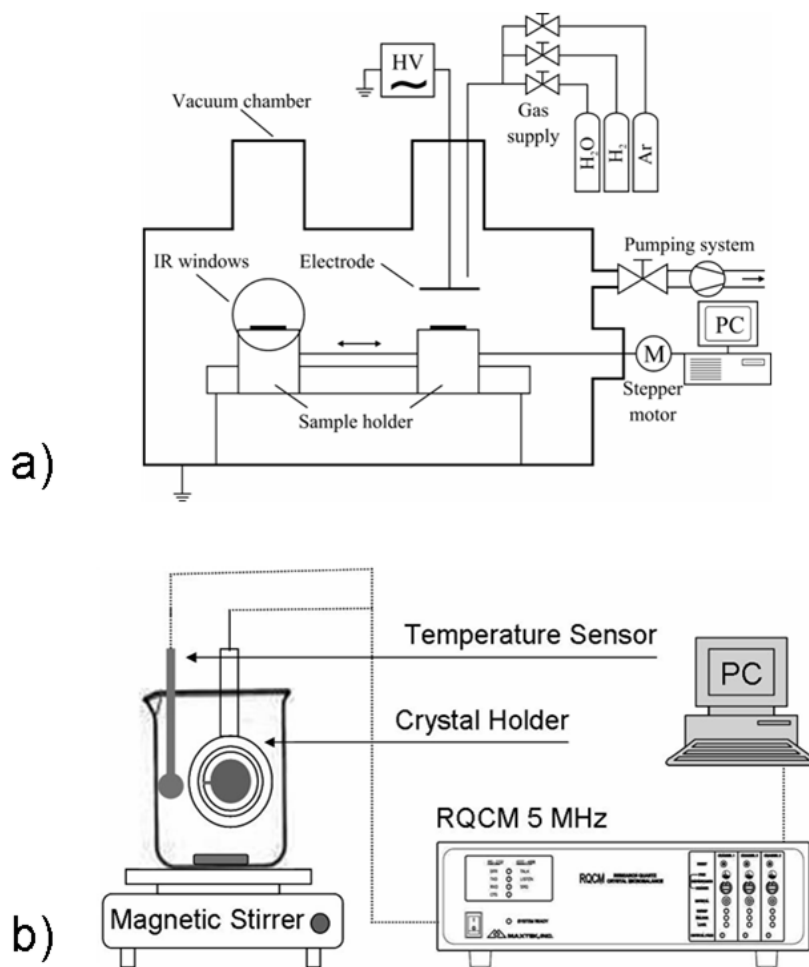


**Figure 4.1.:** Schematic drawing of the experimental setups for a) plasma treatment and in-situ IRRAS and b) the measurements of the adsorption caused mass change on the surface by QCM. [10]

( $56.49 \text{ Hz} \times \text{cm}^2 \times \mu\text{g}^{-1}$ ). To minimize the QCM frequency drift associated with thermal fluctuations, the temperature of the solutions during adsorption was monitored over the complete measurement time and did not fluctuate more than  $0.1 \text{ K}$ . All adsorption measurements were performed in a  $150 \text{ ml}$  glass beaker. Total solution volume in the beaker was  $100 \text{ ml}$  for each measurement. Stirring was accomplished with a magnetic stirrer and a Teflon coated stir bar. The experiments were started

#### 4. Adsorption Kinetics

first in pure ethanol (absolute for analysis, Merck) until the QCM was running with a stable baseline, without any oscillations or shifts. The phosphonic-acid (n-octadecylphosphonic acid  $CH_3(CH_2)_{17}P(O)(OH)_2$ , by Alfa Aesar) was then quickly introduced by a syringe. To achieve final concentrations of  $10^{-4}$  mol/L,  $5 \times 10^{-5}$  mol/L and  $10^{-5}$  mol/L the experiment was started with 99 ml of solvent. After equilibration, 1 ml of the phosphonic acid solution was introduced. The Sauerbrey equation assumes that an additional mass or film deposited on the crystal has the same acousto-elastic properties as the quartz [99]. This assumption results in a sensitivity factor  $C_f$ , which is a fundamental property of the QCM. It is important to note that under these assumptions, the change in frequency is a function of mass per unit area. Therefore, in theory, the QCM mass sensor does not require calibration. However, the Sauerbrey equation is only strictly applicable to uniform, rigid, thin-film deposits.

##### 4.2.3. Surface Analysis

The plasma chamber which is implemented in a FTIR spectrometer (Digilab, FTS 3000) allows an in-situ analysis of the modified surface by Fourier transform infrared reflection absorption spectroscopy (FT-IRRAS). The mid infrared beam is guided by a set of mirrors and transmitted through ZnSe windows onto the sample and reflected under  $80^\circ$  to a liquid nitrogen cooled mercury cadmium telluride (MCT) detector. All presented spectra were recorded using a resolution of  $4\text{ cm}^{-1}$  and originate from a co-addition of 256 single scans. To further enhance the sensitivity for the surface species and to eliminate the gas phase absorption of residual water and carbon dioxide in the spectrometer a discrete polarization modulation was performed [100] [101]. The chemical composition of the oxide layer on freshly evaporated aluminum changes on the time scale of several days [102]. With regard to possible industrial in-line applications, deposited layers were used for each series of measurements within 24 hours after preparation and stored in an exsiccator before using.

##### 4.2.4. Determination of the Mass Sensitivity

The QCM enables the detection of smallest mass changes at the surface of a vibrating quartz by measuring the change of its resonance frequency  $f_q$ . This makes the QCM also suitable for the investigation of coating

#### 4. Adsorption Kinetics

processes. In case of very thin or rigid films, the additional applied mass according to Sauerbrey mass density at the surface  $m_f$  (measured in mass per area) is directly proportional to the change of the resonance frequency  $f_q$ .

$$\Delta f = -C \cdot m_f \quad (4.1)$$

For coatings in solution, the liquid phase directly reduces the resonance frequency. The proportionality between the change in the resonance frequency and the additional mass applied to the surface density remains, so that the measurement of the applied mass density is also possible here. The advantage of the QCM outside of the UHV range is a much wider range of chemicals that can now be used in solutions or chemical vapor deposition (CVD). The wavelength  $\lambda_q$  of the oscillation in the quartz is given by

$$t_q = \lambda_q/2 \quad (4.2)$$

because of

$$\lambda_q \cdot f_q = \nu_q \quad (4.3)$$

it is given

$$f_q \cdot t_q = \nu_q/2 \quad (4.4)$$

The change in resonance frequency  $f_q$  due to a change in the crystal thickness  $t_q$  is given as

$$\frac{\partial f_q}{f_q} = -\frac{\partial t_q}{t_q} \quad (4.5)$$

The negative sign tells a decrease in the frequency with an increase of the thickness required. Equation 4.5 can also be obtained by the mass and its change.

$$\frac{\partial f_q}{f_q} = -\frac{\partial M_q}{M_q} \quad (4.6)$$

Sauerbrey suggested that, when the growing layer is very thin, the change of the mass can be seen as a mass change of the crystal itself. This changes equation 4.6 to

$$\frac{\partial f_q}{f_q} = -\frac{\partial M}{M} \quad (4.7)$$

#### 4. Adsorption Kinetics

The mass of a film applied to the quartz crystal is given as  $M_f$  and the frequency after adsorption as  $f_c$ .

$$\frac{f_c - f_q}{f_q} = -\frac{M_f}{M_q} \quad (4.8)$$

One can also write

$$\frac{f_c - f_q}{f_q} = -\frac{m_f}{m_q} \quad (4.9)$$

For isotropic layers be the mass density can be formulated as a product of thickness and density

$$m_f = t_f \cdot \rho_f, m_q = t_q \cdot \rho_q \quad (4.10)$$

Equation (9) now is expressed as

$$m_f = -(f_c - f_q) \rho_q \nu_q / 2f_q^2 \quad (4.11)$$

but is often symplified to

$$\Delta f = -C \cdot m_f \quad (4.12)$$

Where  $\Delta f$  is the frequency difference before and after the adsorption and  $C$  is the so-called mass sensitivity constant defined as:

$$C = 2f_q^2 / \rho_q \nu_q \quad (4.13)$$

The present system has a theoretical mass sensitivity  $C$  of

$$C = \frac{2 \cdot (5000000s^{-1})^2}{2.650gcm^{-3} \cdot 334000cms^{-1}} = 56.49Hz \cdot cm^2 \cdot \mu g^{-1} \quad (4.14)$$

To verify the mass sensitivity  $C$  of the system a chemical deposition of copper was carried out on the quartz. Thereby the quartz surface is the working electrode connected to a potentiostat, operatinh galvanostatic. A gold wir was chosen as a counter electrode. The experiment was carried out at 15 mA, as the electrolyte is 0.5 M  $CuSO_4$  / 0.5 M  $H_2SO_4$  solution. According to the Faraday law, the mass of chemical deposited copper can be identified:

$$m = \frac{M \cdot I \cdot t}{z \cdot F} \quad (4.15)$$

#### 4. Adsorption Kinetics

In the figure frequency shift vs mass shift 4.2 the slope can be determined. The surface of the crystal was determined to be  $1.23 \text{ cm}^2$ .

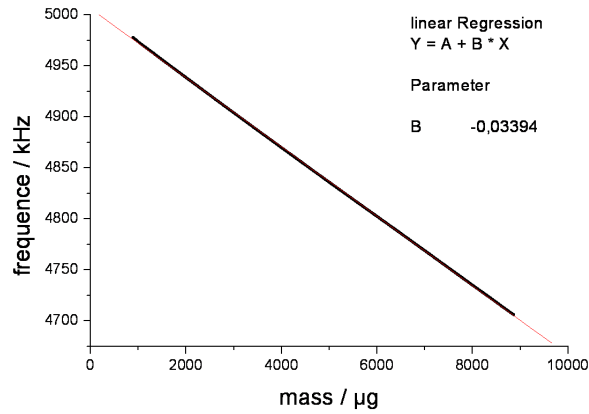


**Figure 4.2.:** The frequency shift vs mass shift for an electrochemical copper deposition on a gold coated quartz.

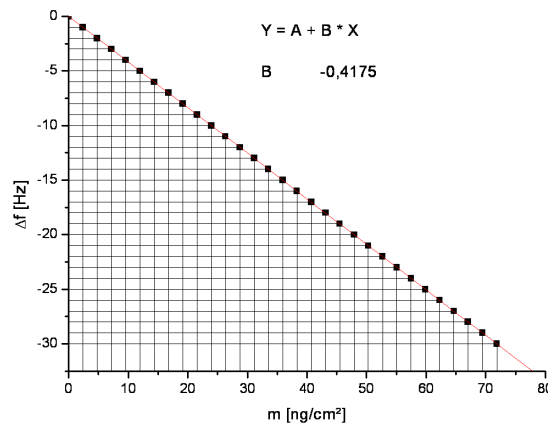


**Figure 4.3.:** Approximating a fixed surface of the quartz now the mass sensitivity can be predicted. In the graph it is shown as frequency shift vs applied mass.

This results in a mass sensitivity  $C$  of

$$C = 41.75 \text{ Hz} \cdot \text{cm}^2 \cdot \mu\text{g}^{-1} \quad (4.16)$$

#### 4. Adsorption Kinetics

The difference between the theoretical and actual calibrated value is essentially determined by the electronics of the product. The comparison with a better-known system, such as the thiols on gold, now allows conclusions about the surface coverage. Under the assumption of an ideal

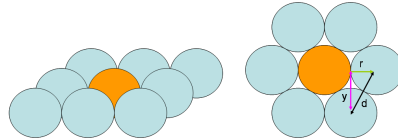


**Figure 4.4.:** An ideal (111) hcp surface.

(111) hcp surface one estimate a maximum of adsorption places  $N$  on the basis of the atoms in the hcp surface. In an ideal quartz crystal surface  $A$  of  $1\text{cm} \times 1\text{cm}$  therefore the following number of adsorption places  $N$  exist:

$$N = \frac{A}{r^2\sqrt{12}} \quad (4.17)$$

Referring to last equations one can determine a dense packed SAM system ( $M \approx 300\text{ g/Mol}$ ) to cause a frequency shift of about  $12\text{ Hz}$ . This

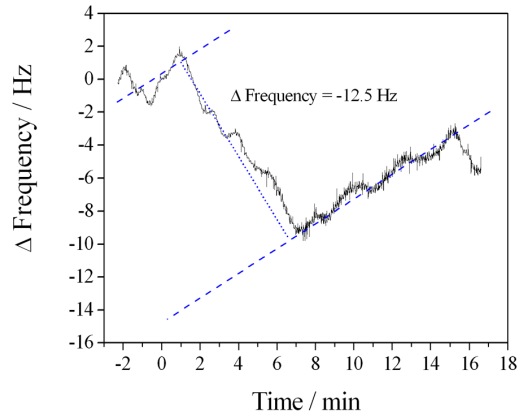


**Figure 4.5.:** Frequency change of a gold coated quartz due to the adsorption of octadecanethiol as SAM.

was proved in model a experiment with gold covered quartz crystals and octadecanethiol as SAM (see figure 4.5).

## 4.3. Results and Discussion

### 4.3.1. Plasma Surface Chemistry

To achieve a carbon contamination free surface before the water plasma modification was performed, each sample was cleaned in an argon/hydrogen plasma. Figure 4.6 shows the corresponding infrared reflection absorption spectra of an aluminum coated quartz crystal surface after the cleaning step with a treatment time of 120 s. The resulting infrared absorption after the modification is related to the signal obtained from the native surface. The cleaning procedure leads to a removal of

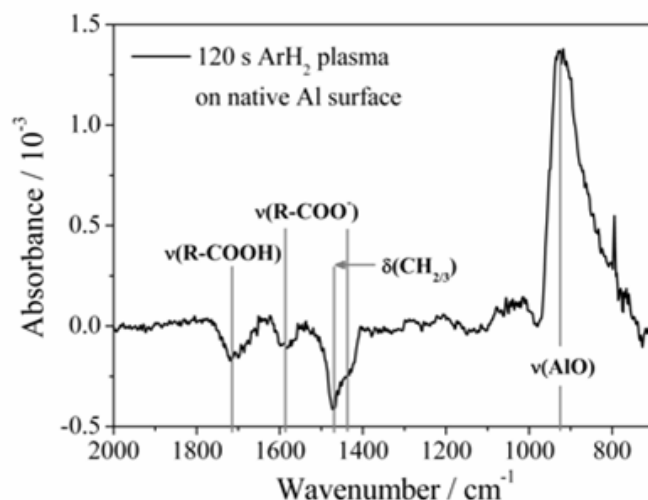


**Figure 4.6.:** In-situ FT-IRRAS of an oxide covered aluminum surface after 120 s argon/hydrogen plasma modification with the surface of the PVD aluminum film as reference. [10]

hydrocarbon contaminations resulting in negative signals in the range of  $2800 - 3000 \text{ cm}^{-1}$  [10] caused by the symmetrical and asymmetrical stretching vibrations of  $\text{CH}_2$  and  $\text{CH}_3$ , and in a weak negative signal at  $1420 \text{ cm}^{-1}$  caused by the deformation vibrations of  $\text{CH}_2$  and  $\text{CH}_3$ . The broad and asymmetrical negative band at  $3500 \text{ cm}^{-1}$  is assigned to a plasma induced remove of adsorbed water from the native oxide layer, the corresponding peak at  $1650 \text{ cm}^{-1}$  is very small (with an expected ratio of 6:1 [95]) and could be overlaid by the broad peak at  $1720 \text{ cm}^{-1}$  (see

#### 4. Adsorption Kinetics

figure 4.6). The negative absorption bands at  $1720\text{ cm}^{-1}$ ,  $1590\text{ cm}^{-1}$  and  $1475\text{ cm}^{-1}$  (see figure 4.6) appear due to a removal of organocarboxylates. The dominant feature of the spectrum is located at  $930\text{ cm}^{-1}$  and results from a first plasma induced formation of  $\text{Al}_2\text{O}_3$  (see positive peak in figure 4.6). The oxidizing species appear in the plasma due to a residual amount of water, oxygen, and carbon mono- and dioxide resulting as well from the vacuum conditions in the chamber ( $p_{\text{base}} \approx 10^{-4}\text{ mbar}$ ) as from plasma induced desorption of adsorbates from the sample surface and from the walls of the chamber. Two processes interact here simultaneously, a formation of surface oxides and hydroxides due to the residual gases in the plasma volume and an additional transformation of aluminum hydroxide to aluminum oxide, due to the influence of the argon plasma. The other aspect will be discussed more detailed later. Figure 4.7 shows the infrared reflection absorption spectra of an alu-

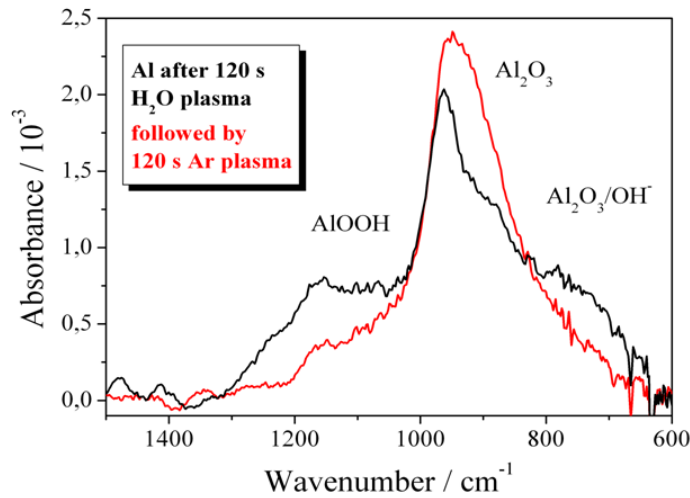


**Figure 4.7.:** In-situ FT-IRRAS of an oxide covered Al surface after a water and subsequently argon plasma modification related to the background acquired after the cleaning step; the region of Al – O, Al – OH and  $\text{H}_2\text{O}$  vibrations ( $1800 - 600\text{ cm}^{-1}$ ). [10]

minum coated quartz crystal surface after the Ar/ $\text{H}_2$  plasma cleaning step and subsequent  $\text{H}_2\text{O}$  plasma modification (black line) and after an additional Ar plasma treatment (grey line). Both spectra were acquired in-situ immediately after the respective plasma modification and were re-

#### 4. Adsorption Kinetics

lated to a background measured immediately prior to the water plasma treatment. The interesting regions of the spectrum are expanded to a larger scale. The region from  $2800\text{ cm}^{-1}$  to  $3800\text{ cm}^{-1}$  includes the vibration modes of terminal hydroxyls ( $3700\text{--}3800\text{ cm}^{-1}$ ), bridging hydroxyls, hydrogen bridge bonded hydroxyls and water ( $3200\text{--}3500\text{ cm}^{-1}$ ). The broad asymmetric absorption band in the spectrum has its maximum at  $3500\text{ cm}^{-1}$ . The absence of the corresponding band at  $1650\text{ cm}^{-1}$  for the water molecules is a hint for the lack of water in the formed film. An absorption band at  $3700\text{--}3800\text{ cm}^{-1}$  is also absent, which indicates that the water plasma modification does not increase the density of terminal non-hydrogen bonded hydroxyls compared to the Ar/H<sub>2</sub> plasma cleaned native passive film. For these reasons the measured absorption band can be assigned to the symmetric and asymmetric vibration modes of bridging or hydrogen bridge bonded hydroxyls in the formed layer. The exact wavenumber of these vibration modes depends on the local chemical environment of the hydroxyls [95]. The second important region from  $600\text{ cm}^{-1}$  to  $1800\text{ cm}^{-1}$  is shown in figure 4.7). The water plasma treatment induced absorption bands within these range represent the vibration modes of AlOOH ( $1100\text{ cm}^{-1}$ ), Al<sub>2</sub>O<sub>3</sub> ( $950\text{ cm}^{-1}$ ) and OH- adsorbed on Al<sub>2</sub>O<sub>3</sub> [103] [104]. There is a second possible outcome of the water plasma modification, which was observed under certain conditions. In this case the feature of the FTIR spectrum at  $950\text{ cm}^{-1}$  does not appear and the vibration bands attributed to the hydroxides are detected only. The authors suppose, that this behavior strongly depends on the thickness of the already air formed oxide film, which can not be furthermore increased by a plasma treatment. The observations and results described in the following are independent from the formation of this additional oxide layer, since the formation of aluminum hydroxides is the crucial process. To check a possible reversibility of the water plasma induced tailoring of the surface chemistry on oxide covered aluminum an additional argon plasma treatment of the modified oxide layer was performed. This subsequent argon plasma treatment leads to an increase of the Al<sub>2</sub>O<sub>3</sub> signal in the FTIR spectrum in figure 4.7) while the intensities of the AlOOH and of the OH-peaks decrease. This can be explained with a partial transformation of hydroxides into oxides under argon ion bombardment. This is similar to the observation of Grundmeier and Stratmann, that an argon plasma treatment of an oxide film on iron, which was formed by an oxygen plasma, does not change the

#### 4. Adsorption Kinetics

layer thickness but changes significantly the film chemistry [97]. The influence of the argon ion bombardment on the surface chemistry of aluminum was not discussed intensively in the literature until now. It is well known that an ion bombardment might change the surface chemistry depending on the substrate material e.g. during a sputter process [105]. McCafferty and Wightman used an argon plasma for cleaning of native aluminum surface from carbon contamination and did not observe any changes neither in the oxide thickness nor in the  $\text{OH}^-/\text{O}^{2-}$ -ratio by XPS measurements [106]. This discrepancy in the results might be explained by the differences in the plasma conditions in the experiments.

##### 4.3.2. Adsorption Kinetics of Octadecylphosphonic Acid

IRRAS measurements were done after the phosphonic acid adsorption as well on native as on plasma pretreated samples. For the IRRAS studies the adsorption time was varied between 30 s and several hours. As an example the corresponding characteristic IR absorption bands of the adsorbed phosphonic acid on water plasma treated passive film on aluminum are shown in figure 4.8. In this case the adsorption time was chosen to be two hours.

Part a) of the spectrum shows the range of  $2750 - 3050 \text{ cm}^{-1}$  with the symmetric and asymmetric stretching vibrations of the  $\text{CH}_2$  chains with a  $\text{CH}_3$  head group. In part b) the range of  $700 - 1600 \text{ cm}^{-1}$  with a broad line with a centre at  $1100 \text{ cm}^{-1}$  is shown, which can be assigned to a convolution of symmetric and asymmetric stretching bands of the phosphonate groups. As already discussed by Maege et al. [91] for long chain aliphatic phosphonates, salts of the alkylphosphonic acids give characteristic stretching vibrations at  $1125 - 970 \text{ cm}^{-1}$  and at  $1000 - 960 \text{ cm}^{-1}$ . Based on this argument the broad absorption at  $1100 \text{ cm}^{-1}$  indicates that bonding to the aluminum oxi-hydroxide surface occurs via a acid-base interaction. The position and intensity of all peaks assigned to the adsorbed organophosphonic acids were proven to be independent of the adsorption time and the respective plasma pre-treatment of the aluminum surface.

To reveal the adsorption kinetics the QCM technique was applied. The frequency transients caused by adsorption of organophosphonic acids on different pretreated oxide films on PVD aluminum are shown in figure 4.9. The adsorption induced resulting frequency change, which was achieved

#### 4. Adsorption Kinetics

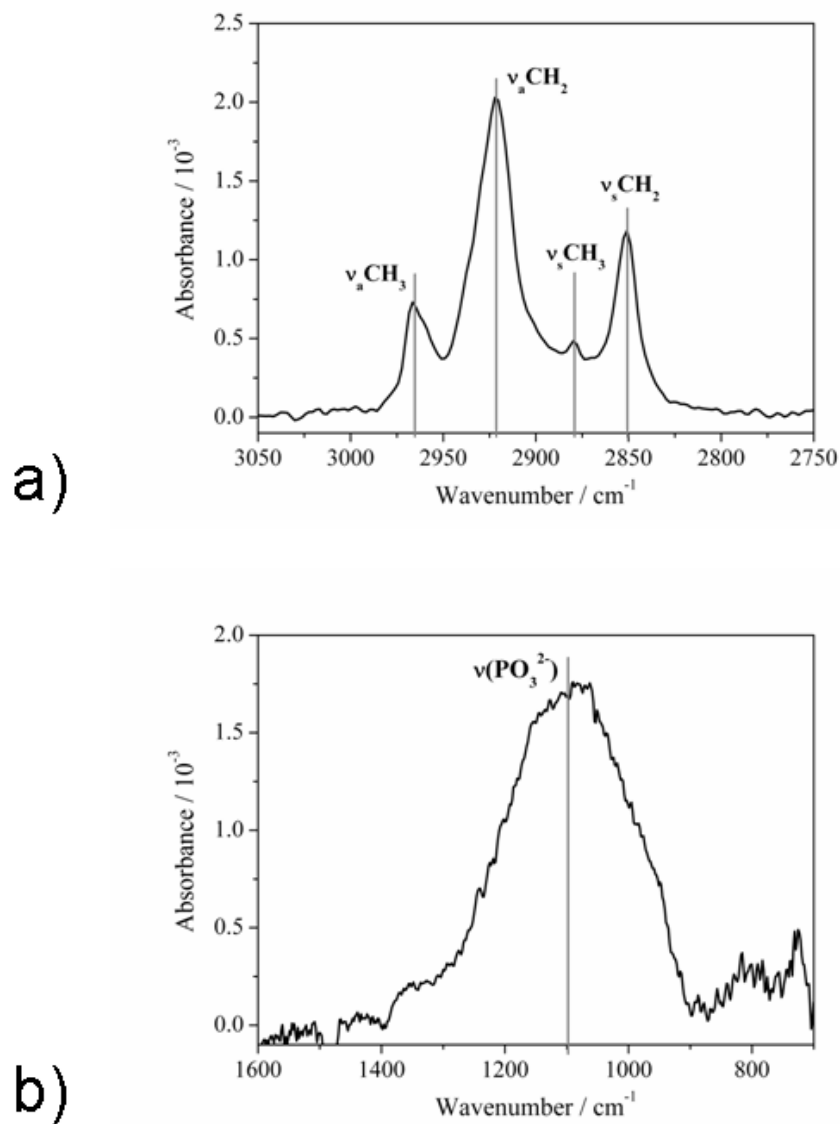


**Figure 4.8.:** FT-IRRAS of an Al surface after 2 h rinsing in an ODPA solution, (a) range of the hydrocarbon vibrations and (b) vibration region of the phosphonates. [10]

for long times of immersion on native and plasma treated oxide films on PVD aluminum surfaces was reproducible and did not vary significantly with the initial hydroxide to oxide ratio of the PVD deposited

#### 4. Adsorption Kinetics

film. However, the transients show a remarkable dependence on the

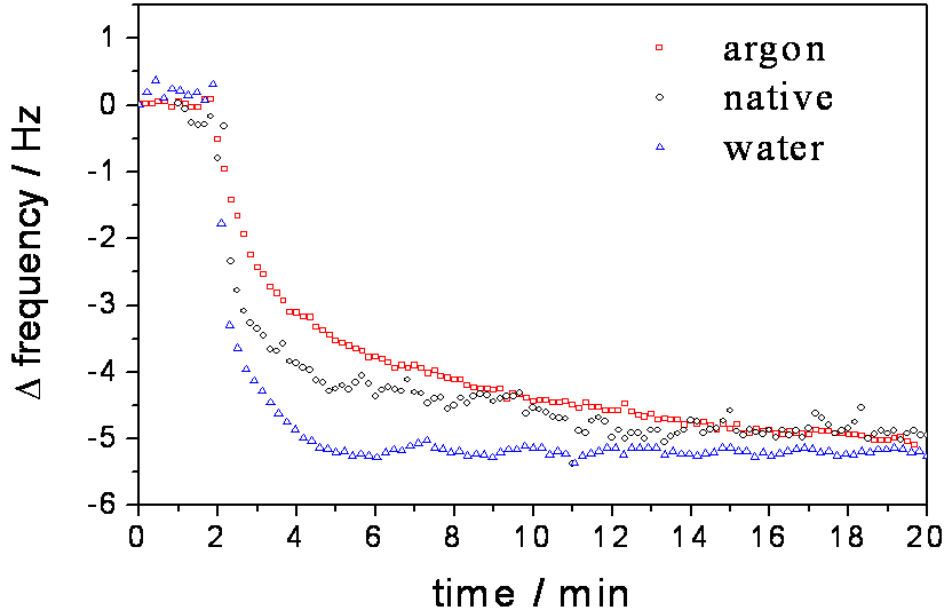


**Figure 4.9.:** Frequency change of an aluminum coated quartz crystal due to the adsorption of ODPA  $10^{-4} \text{ mol/L}$  on the native oxide film, on a water plasma modified oxide film and on a water and subsequently argon plasma treated passive film on aluminum measured by means of QCM. [10]

plasma treatment. Figure 4.9 shows the frequency changes after addition of ODPA for all discussed surface modifications. On the native oxide film on the aluminum surface an initial fast decrease of approximately  $-2 \text{ Hz}$  with a further slower decay of the frequency down to a limiting value of  $-5 \text{ Hz}$  takes place. After reaching this plateau value the adsorption was accepted as complete and the measurement was terminated. In the case of adsorption on a water plasma modified oxide on aluminum surface the time required for a frequency change of  $-5 \text{ Hz}$  was significantly shorter than in the case of the native passive film. The subsequent argon plasma treatment of a water plasma modified passive film on aluminum resulted in slower adsorption kinetics comparable with the adsorption kinetics on the native surface. The fast initial drop of the quartz frequency followed by a slower decrease in case of native passive film on the aluminum surface suggests either a two step process at different rates or the existence

#### 4. Adsorption Kinetics

of at least two types of adsorption sites with different adsorption energies. For the H<sub>2</sub>O-plasma treated surface with high hydroxyl density already no second regime with slower adsorption kinetics is observed. This can be explained by the high density of hydroxyl sites dominating the adsorption kinetics. For less hydroxyl rich surfaces it is likely, that the non hydroxyl terminated surface areas show slower adsorption kinetics. Especially, the argon plasma treatment creates a comparable clean surface but as previously mentioned leads to a partial transformation of the hydroxides to oxides and effectively leads to a decrease of the adsorption rate. These effects show that the assumption of a dependence of adsorption kinetics of phosphonates on oxide covered aluminum from the density of hydroxyl functions on the surface is an appropriate way to explain the observed phenomena on plasma treated passive films on aluminum. An additional line of experiments were performed to investigate the dependence of concentration on the adsorption kinetics, again according to the system oxide covered aluminum and ODPA. The cov-

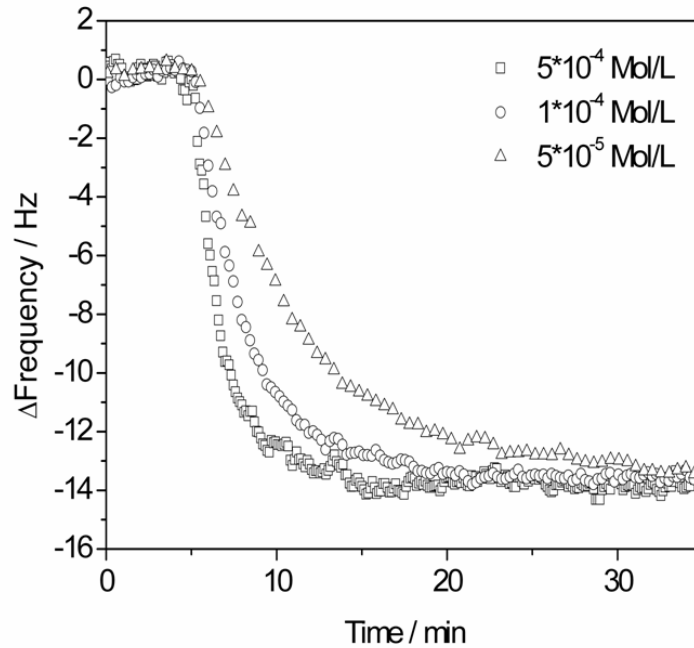


**Figure 4.10.:** Frequency change of an aluminum coated quartz crystal due to the adsorption of ODPA with three different concentrations, measured by means of QCM.

#### 4. Adsorption Kinetics

erage of the QCM electrode surface is expressed as a unitless quantity  $\Theta$ , the fraction of available sites that have reacted, or, equivalently, the fraction of a monolayer ( $0 \leq \Theta \leq 1$ ). The Langmuir isotherm dictates that the rate of surface reaction is given by

$$\frac{d\Theta}{dt} = k_a (1 - \Theta) c - k_d \Theta \quad (4.18)$$

where  $\Theta$  is the fraction of surface covered,  $(1 - \Theta)$  is the fraction of surface exposed,  $c$  is the concentration, and  $k_a$  and  $k_d$  are the association and dissociation constants, respectively. Integration of equation 4.18 yields the time course of the monolayer formation

$$\Theta(t) = \frac{c}{c + \left(\frac{k_d}{k_a}\right)} [1 - \exp(-(k_a c + k_d) t)] \quad (4.19)$$

This result can be simplified by

$$k_{obs} = k_a \times c - k_d \text{ and } K = \frac{c}{c + \left(\frac{k_d}{k_a}\right)} \quad (4.20)$$

giving

$$\Theta(t) = K [1 - \exp(-k_{obs} t)] \quad (4.21)$$

Fitting the experimental data gives  $k_{obs}$ . Since a plot of  $k_{obs}$  vs  $c$  for a

**Table 4.2.:** Fitting values determined from raw data as a function of ODPA concentration.

ODPA concentration[mol/L]	$k_{obs}$ [s <sup>-1</sup> ]
$1 \times 10^{-4}$ mol/L	0.546
$5 \times 10^{-5}$ mol/L	0.344
$1 \times 10^{-5}$ mol/L	0.196

series of concentrations gives a line with a slope of  $k_a$ , and an intercept of  $k_d$  (see figure 4.11).

The values obtained are presented in table 4.2. The data we present in Table 2 allow the determination of the equilibrium constant,  $K_{eq}$  for the monolayer system.

$$K_{eq} = k_a/k_d \quad (4.22)$$

#### 4. Adsorption Kinetics

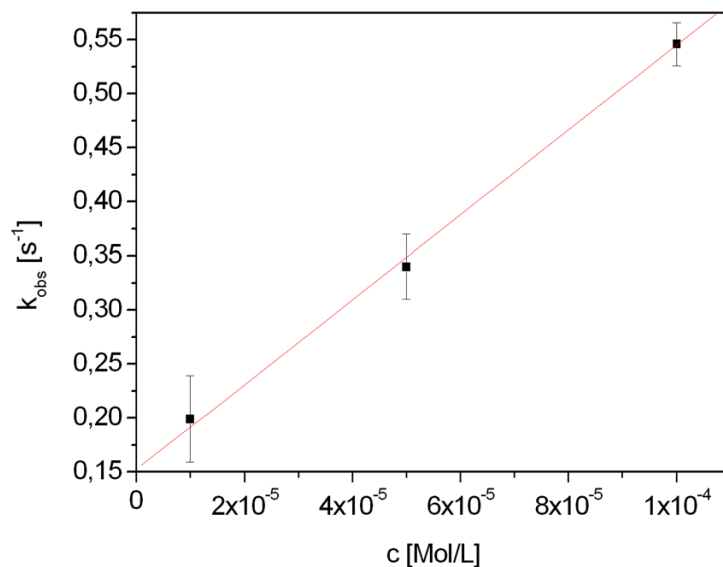


**Figure 4.11.:** Plot of  $k_{obs}$  vs  $c$  for a series of concentrations.

We can obtain important physical quantities from  $K_{eq}$ . The free energy of adsorption of the monolayer is found directly from the equilibrium constant data.

$$\Delta G_{ads} = -RT \ln K_{eq} \quad (4.23)$$

We show in table 4.3 the free energy and equilibrium constant we have determined. The data show that desorption plays an important role in

**Table 4.3.:** Equilibrium constant  $K_{eq}$  of the adsorption reaction and free energy of adsorption  $\Delta G_{ads}$  determined from the experimental data.

$K_{eq}$	$\Delta G_{ads}$ [ $\text{kJ} \times \text{mol}^{-1}$ ]
25920	-24

the formation of the ODPAs monolayers, because  $k_d > 0$ . This is an important finding in and of itself, because the existence of a nonzero  $k_d$  for phosphonic acid SAMs demonstrates that the adsorption surface reaction in ethanol is reversible, and therefore at any given instant in time, some fraction of the adsorbate sites on the surface is unoccupied.

Since the density of hydroxyl groups dominates the adsorption kinetics

#### 4. Adsorption Kinetics

and as proven by the FTIR-data the chemisorbed molecule is deprotonated, a two step mechanism of the adsorption process can be assumed. The nucleophilic substitution of organophosphonic acids on hydroxide rich oxide covered aluminum surfaces is initiated by the formation of hydrogen bonds. The hydroxyl groups of the phosphonic acid interact with the hydroxylated aluminum oxide surface. This transition state is followed by a condensation reaction leading to stable acid-base interactions between the phosphonate and the aluminum oxide surface. As an explanation for the finally equal overall frequency shift after the full completion of adsorption process it might be assumed that the adsorption of the phosphonic acid group and the subsequent condensation reaction lead to the additional formation of hydroxides on the Ar-plasma treated oxide surface.

## 4.4. Conclusions

The water and subsequent argon plasma modification of native oxide covered aluminum was studied for the first time by in-situ IRRAS. These measurements showed that a water plasma treatment increases the density of hydroxides in the oxide surface layer while a subsequent argon plasma transforms the hydroxides to oxides.

The combination of ex-situ IRRAS with QCM measurements of the adsorption process of ODPAs as well on native oxide covered aluminum as on plasma modified films has shown a strong dependence of the adsorption kinetics on the density of hydroxyl functions on the oxide covered aluminum surface. By the increase in the surface hydroxyl density the adsorption kinetics can be accelerated. Such an acceleration can be explained by the adsorption of the phosphonic acid via surface hydrogen bonds prior to the condensation reaction leading to the finally adsorbed phosphonate.

Furthermore the existence of a nonzero  $k_d$  for phosphonic acid SAMs demonstrates that the adsorption surface reaction is reversible. In other cases this equilibrium will represent a mobility of the SAM on the surface.

## 4.5. Outlook

The QCM has been introduced as a system being able to investigate SAM on metal and oxide covered surfaces. Research systems like the QCM, which have a high resolution of time are precious in the investigation field of kinetics. Quartzes of the QCM can easily be equipped by new metals or oxides with the help of physical or chemical vapor deposition. This will expand the research possibilities for the QCM in the future. One problem which has to be addressed is that the actual surfaces on the quartz crystals can not be grown in a single crystalline way.

# 5. Water Adsorption and Proton Exchange Reactions on Octadecylphosphonic Acid Monolayer Covered Aluminum

## 5.1. Introduction

The corrosion resistance and the adhesion of organic coatings on oxide covered aluminum is of high importance and is mainly determined by the alloy composition, the surface chemistry of the alloy and the composition of the organic coating. To substitute surface technologies such as anodizing or conversion chemistry, adhesion promoting, ultra-thin films or even monomolecular layers like self-assembled monolayers of organophosphonic acids have been investigated as new advanced interfacial layers for polymer coated aluminum alloys [109]. Although the adhesion and interfacial corrosion protection of these adsorbed monolayers proved to be excellent even in comparison to thicker conversion films, to date the barrier properties and the influence of water on the interface between the adsorbed organophosphonic acid and the oxide covered substrate was not evaluated in detail. Alexander et al. [115] showed that an aluminum surface under atmospheric conditions is covered by a thin pseudo-boehmite layer. This layer consists of the two main phases  $-\text{Al}_2\text{O}_3$  and  $-\text{Al}(\text{O})\text{OH}$ . The hydroxide to oxide ratio can be characterized by means of high resolution XPS and appropriate curve fitting. It was observed that surface hydroxyl groups promote the adsorption of organophosphonates and that the adhesion of the phosphonate group is based on an acid-base interaction. The driving force is assumed to be the formation of a surface salt as already described for long-chain carboxylic acids by

## 5. Formation and Stability I

Allara et al. [115] and recently by Terryn et al. [116] [117]. In a recent study Giza et al. [118] employed quartz crystal microweighing to investigate the effect of the surface hydroxylation on the adsorption rate of ODPA on aluminum films. It was shown that the adsorption velocity depends on the OH-density of the surface and can be directly influenced by plasma modification. Wapner et al. [109] applied water soluble aminopropylphosphonic acids as short chain adhesion promoting molecules on aluminum alloy surfaces from dilute aqueous solutions and from a liquid adhesive film and showed excellent filiform corrosion resistance. Maege et al. [111] investigated the adsorption of amino functionalized long-chain organo-phosphonic acids on pure aluminum substrates and have shown an equivalent corrosion protection and an improved adhesion to model coatings in comparison to chromated surfaces. Pahnke et al. [110] showed the effective coupling of benzophenone containing organophosphonates to oxide covered aluminum surfaces which opens the way of adhesion promotion to organic layers via a photochemical reaction. There have been many spectroscopic, microscopic, and theoretical studies of thin film interactions and molecular configurations at the bulk water/substrate interface [119] [121]. However, the microscopic details of how the water interacts with a polar surface covered with a hydrophobic monolayer is still not fully understood. An incorporation of water at the organic/oxide interface promotes wet de-adhesion of organic layers which are bound to the surface via van der Waals forces. It is of high interest to understand the origin of the high molecular adhesion forces of hydrophobic organophosphonate monolayers on oxide covered surfaces which might be based on the barrier properties for water or the water resistant interfacial chemical bond. To analyse the barrier properties of ODPA SAMs on oxide covered aluminum, a combination of in-situ FTIR-spectroscopy under grazing incidence and in-situ QCM was applied in the here presented studies. Water adsorption isotherms were measured by means of the QCM on oxide covered PVD aluminum films and on adsorbed self-assembled monolayers of ODPA. After a H<sub>2</sub>O-plasma modification of the aluminum surface, the isotope exchange was measured in-situ by means of time-resolved IRRAS in a D<sub>2</sub>O containing gas phase. The surface energies of both prepared states of the samples, bare aluminum oxide and ODPA self-assembly film covered one, were characterized by means of static contact angle measurements.

## 5.2. Experimental

### 5.2.1. Sample Preparation

Aluminum layers were deposited on quartz crystals and on glass by physical vapour deposition (PVD). Both types of samples were coated with 250 nm aluminum layer (Al 99.99 %) using electron beam evaporation (Univex 450, Leybold AG). During the evaporation the layer thickness was monitored by a QCM (Inficon XTC). Prior to film deposition the samples were thoroughly cleaned in a mixture of hydrogen peroxide (30 %, Merck, Germany) and ammonia (25 %, Merck, Germany) (1:1) for 60 minutes at 80 °C, afterwards rinsed with de-ionized water and dried in a stream of nitrogen. The chemical composition of the oxide layer on freshly evaporated aluminum changes on a time scale of several days [140]. With regard to possible industrial in-line applications deposited layers were used within 24 hours after preparation for each series of measurements. The ODPAs on the aluminum oxide surfaces were prepared by solution self-assembly under ambient conditions and then transferred into high vacuum environment. Substrates were ultrasonically cleaned in abs. ethanol (> 99.9 %, Merck, Germany) for 10 minutes before immersing into a 1 mM ethanolic solution of ODPAs for 24 h. After rinsing with ethanol the samples were dried in a stream of nitrogen.

### 5.2.2. Surface Chemistry

The experimental setup for the plasma treatment, in-situ IRRAS, the measurements of the water adsorption by QCM and the plasma characterization by OES is shown in figure 5.1. The sample can be mounted on two different holders which are moved by a stepper motor along the chamber axis. One of the sample holders is a flat carriage, mainly used for IRRAS and the other one is capable of hosting quartz crystal resonators of 10 MHz. For a uniform modification of the surface the sample can be moved through the plasma zone with a constant velocity which determines the time of exposure. A more detailed description of the plasma generation is given elsewhere [123]. The base pressure of the chamber before flushing with the working gases was ensured to be in the range of  $10^{-4}$  mbar. The pressure of the corresponding gas atmosphere during all plasma modifications was adjusted to 0.3 mbar. Pure gases were used for

## 5. Formation and Stability I

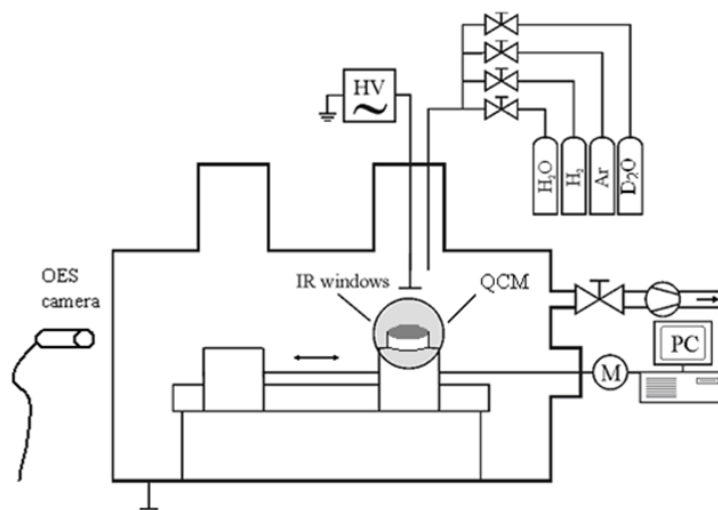


**Figure 5.1.:** Schematic drawing of the experimental setup including plasma treatment, OES, in-situ IRRAS and in-situ QCM.

the experiments, argon and hydrogen in the quality 5.0 by Air Liquid. A closed flask with a high precision valve was filled with ultra pure water and was used for water plasma modifications. The water was frozen by dipping in liquid nitrogen and the residual gas content was pumped down before usage. For the adjustment of the water vapor atmosphere in the plasma chamber at  $0.3 \text{ mbar}$ , the water partial pressure was used and the pumping system was throttled.

### 5.2.3. Surface Analysis

#### Polarization Modulation Infrared Reflection Absorption Spectroscopy

PM-IRRAS measurements were performed on a step scan interferometer (Bruker Vertex 70) at a resolution of  $4 \text{ cm}^{-1}$  and  $80^\circ$  relative to the substrate surface normal. For p-polarization of the IR light an aluminum wire grid was used and modulated at  $100 \text{ kHz}$  with a ZnSe Photo-Elastic-Modulator (PEM, Bruker PMA-50). Light reflected from the sample was focused with a ZnSe lens onto a cryogenic mercury cadmium telluride (MCT) detector. All presented spectra were recorded from 512 single scans.

## 5. Formation and Stability I

### **Infrared Reflection Absorption Spectroscopy**

The plasma chamber which is implemented in a FTIR spectrometer (Digilab, FTS 3000) allows an in-situ analysis of the modified surface by FT-IRRAS. The infrared beam is guided by a set of mirrors and transmitted through ZnSe windows onto the sample. The IR beam is reflected under  $80^\circ$  to a liquid nitrogen cooled MCT detector. All presented spectra were recorded using a resolution of  $4\text{ cm}^{-1}$  and originate from a co-addition of 256 single scans. A discrete polarization modulation was performed to further enhance the sensitivity for the surface species and to eliminate the gas phase absorption of residual water and carbon dioxide in the spectrometer [124] [125].

### **Quartz Crystal Microbalance**

For the in-situ measurement of mass adsorption on the surface a custom made QCM for crystals with a with a resonance frequency of about  $10\text{ MHz}$  was designed and implemented in the in-situ FTIR cell [126]. The QCM with a resonance frequency of  $10\text{ MHz}$  is sensitive to mass changes down to nanograms (sensitivity factor  $225.96\text{ Hz} \times \text{cm}^2 \times \mu\text{g}^{-1}$ ). The accuracy of the QCM is primarily limited by the temperature dependence of the quartz resonance frequency.

### **Optical Emission Spectroscopy**

An OES was installed outside the chamber to characterize the plasma chemistry. By OES it is possible to produce analysis of the plasma composition with high accuracy [127]. During the plasma modifications, the OES collimator (Plasus EmiCon) is directly positioned in front of a quartz glass window of the plasma chamber.

### **Static Contact Angle Measurement**

The contact angles of water, di-iodomethane and ethylene glycol on the surfaces were measured by means of the sessile-drop method at three different points using a goniometer (OCA 20, Dataphysics, Germany). For the determination of the surface energy water, di-iodomethane, and ethylene glycol were used. Their corresponding values of  $\gamma_s$  and  $\gamma_l$  are summarized in table 7.1.  $\gamma_s$  and  $\gamma_l$  denote the solid surface energy and the liquid surface

## 5. Formation and Stability I

**Table 5.1.:** Liquid surface tensions (at 298 K) of the used liquids for the determination of the substrate surface free energy; The data are from the database in the software SCA 2.0.

Energy [ $mJ/m^2$ ]	water	di-iodomethane	ethylene glycol
$\gamma_l$	<b>72.1</b>	<b>50.0</b>	<b>48.0</b>
$\gamma_l^d$	<b>19.9</b>	<b>47.4</b>	<b>29.0</b>
$\gamma_l^p$	<b>52.2</b>	<b>2.6</b>	<b>19.0</b>

tension, respectively. The superscripts d and p refer to the dispersion force and polar force components, respectively.

## 5.3. Results and Discussion

### 5.3.1. Plasma Surface Chemistry on Aluminum

Native oxide aluminum grows according to the Cabrera-Mott mechanism [138]. Adsorbed oxygen and hydroxide ions produced by electron-impact induced chemistry at the interface between the oxide and the plasma volume, induce a strong electric field across the oxide layer that drives ionic migration through the film. Depending on the specific mobilities of the species, either  $Al^{3+}$  ions move towards the oxide surface or oxygen ions towards the metal/oxide interface. The transport of electrons is considered to be independent of the ionic motion and fast in comparison to the ion transport [139]. Figure 5.2 shows a PM-IRRAS spectrum of a native passive film of a PVD aluminum film. The spectrum illustrates that the metal surface is covered with an oxyhydroxide film and adsorbed atmospheric organic contaminations. Known methods for the organic contaminations removal are etching with piranha solution (conc.  $H_2SO_4/30\%H_2O_2$ , 3:1), electrochemical potential cycling, UV photooxidation, ozonolysis, thermal desorption, and plasma cleaning [135] [136] [137] [138]. Of these, the first two are wet chemical processes which bear the danger of contamination by the reagents used and thus are very unfavorable for most applications. The same may be true for the argon plasma method but has not been investigated sufficiently yet. As an alternative, water plasma can be used. In contrast to the inert argon, water plasma is chemically reactive and reacts with the organic contaminations to form gaseous products during the cleaning process. These fragments

## 5. Formation and Stability I

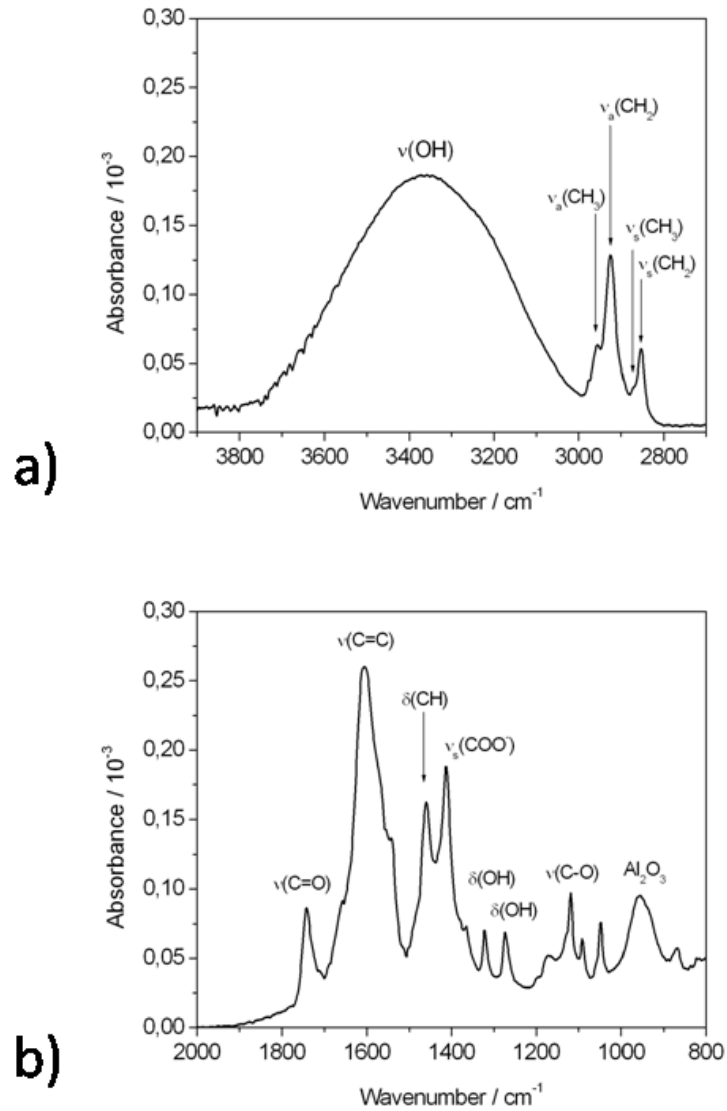


**Figure 5.2.:** PM-IRRAS spectrum of a native passive film covered PVD aluminum film.

were volatile enough to be pumped away by the continuous gas flow. Therefore, no further cleaning process, such as rinsing, is necessary. This makes plasma cleaning an attractive method for surface treatment. To achieve a surface with reduced carbon contamination each sample was initially cleaned in an argon/hydrogen plasma. This cleaning step leads to a

## 5. Formation and Stability I

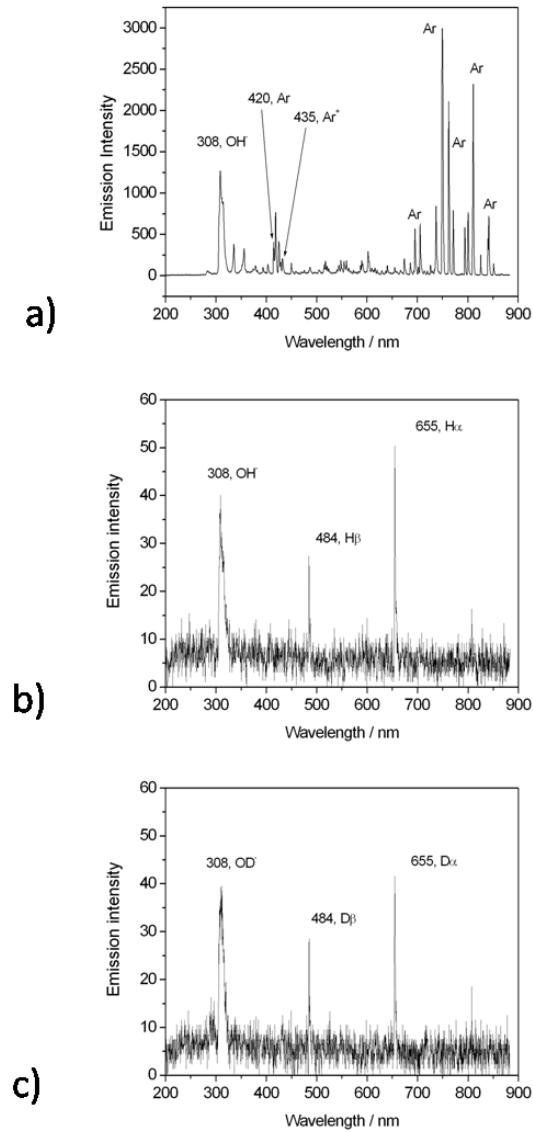


**Figure 5.3.:** Optical emission spectra of a) Ar/H<sub>2</sub>-Plasma, b) H<sub>2</sub>O-Plasma and c) D<sub>2</sub>O-Plasma.

removal of residual organic contaminations and carbonates or organocarboxylates and a decrease of the amount of hydroxides within the native oxide layer [118]. In figure 5.3 OES of a) Ar/H<sub>2</sub>-plasma, b) H<sub>2</sub>O-plasma and c) D<sub>2</sub>O-plasma are presented. Spectra of the water plasma are dom-

## 5. Formation and Stability I

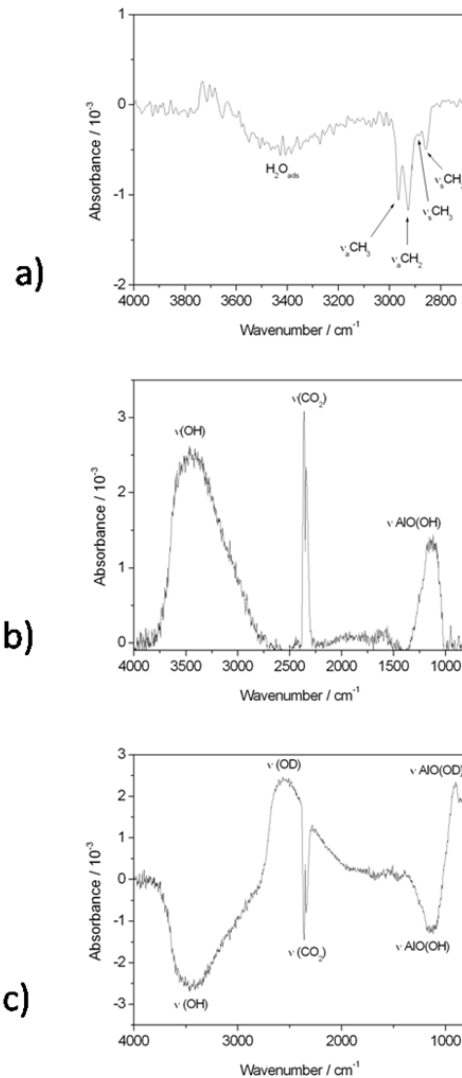


**Figure 5.4.:** (a) In-situ FT-IRRAS of an oxide covered aluminum surface after 120 s Ar/H<sub>2</sub>-plasma modification with the surface of the as prepared PVD aluminum film (b) In-situ FT-IRRAS of an oxide covered Al surface after a 120 s H<sub>2</sub>O-plasma and (c) a subsequent exposure to a 120 s D<sub>2</sub>O-plasma.

inated by a main peak centred at 308 nm belonging to the OH<sup>-</sup> / OD<sup>-</sup> species. At 655 nm and 484 nm, two sharp lines of hydrogen / deu-

## 5. Formation and Stability I

terium,  $H_\alpha$  and  $H_\beta$   $D_\alpha$  and  $D_\beta$ , can be seen clearly. It is remarkable that  $\text{OH}^-$  is the most active species of hydrogen in the Ar/ $\text{H}_2$ -plasma, which is concluded from intensity ratio of the peaks. One reason might be the pressure region of  $10^{-4}$  and thus a quite high rest of oxygen and water in the chamber to react with the hydrogen. Furthermore the OES of the water plasma shows why it will be able to clean a surface from organic contaminations without problems. Induced from the plasma voltage the water is fragmented into its most reactive parts.

In figure 5.4 the in-situ IRRAS data of an aluminum coated quartz crystal surface after the Ar/ $\text{H}_2$ -plasma are shown. In accordance with the PM-IRRAS data the difference spectrum shows the removal of hydroxyls and organic contaminations. The in-situ IRRAS data after a subsequent water plasma treatment are presented in figure 5.4 b). Moreover, the spectrum after the exposure of the  $\text{H}_2\text{O}$  plasma treated surface to a  $\text{D}_2\text{O}$  plasma is shown in figure 5.4 c) for comparison. After the  $\text{H}_2\text{O}$  plasma the surface is enriched in hydroxyl groups as indicated by the positive peaks  $1100\text{ cm}^{-1}$ . The proton exchange reaction is clearly reflected by the decrease in the OH-peak between  $3000$  and  $3600$  and the increase in the peak intensity between  $2000$  and  $2700\text{ cm}^{-1}$ . The spectral region between  $3700$  and  $3800\text{ cm}^{-1}$  includes the vibration modes of terminal hydroxyls, bridging hydroxyls, hydrogen bonded hydroxyls and water ( $3200$ - $3500\text{ cm}^{-1}$ ). The broad asymmetric absorption band in the spectrum a) has its maximum at  $3500\text{ cm}^{-1}$ . The missing  $\text{H}_2\text{O}$  deformation peaks at  $1500\text{ cm}^{-1}$  indicate that the surface is almost free of adsorbed water layers on top of the hydroxide surface layer. The finger print region between  $600\text{ cm}^{-1}$  and  $1400\text{ cm}^{-1}$  shows that the hydroxyls of  $\text{AlOOH}$  layer are exchanged with OD groups.

### 5.3.2. In-situ Quartz Crystal Microweighing during $\text{H}_2\text{O}$ and $\text{D}_2\text{O}$ Plasma Treatment of Aluminum Films.

To complement the in-situ FT-IRRAS data for the plasma treatments the QCM frequency changes were measured simultaneously. In figure 5.5 the QCM transients during Ar/ $\text{H}_2$  and  $\text{H}_2\text{O}$  plasmas are shown. The Ar/ $\text{H}_2$ -plasma leads to an increase of the frequency by about  $23\text{ Hz}$  proving the desorption of contaminations and hydroxides. The frequency change during the plasma-on time can be explained by the electronic conductivity of the plasma which influences the overall impedance of the quartz.

## 5. Formation and Stability I

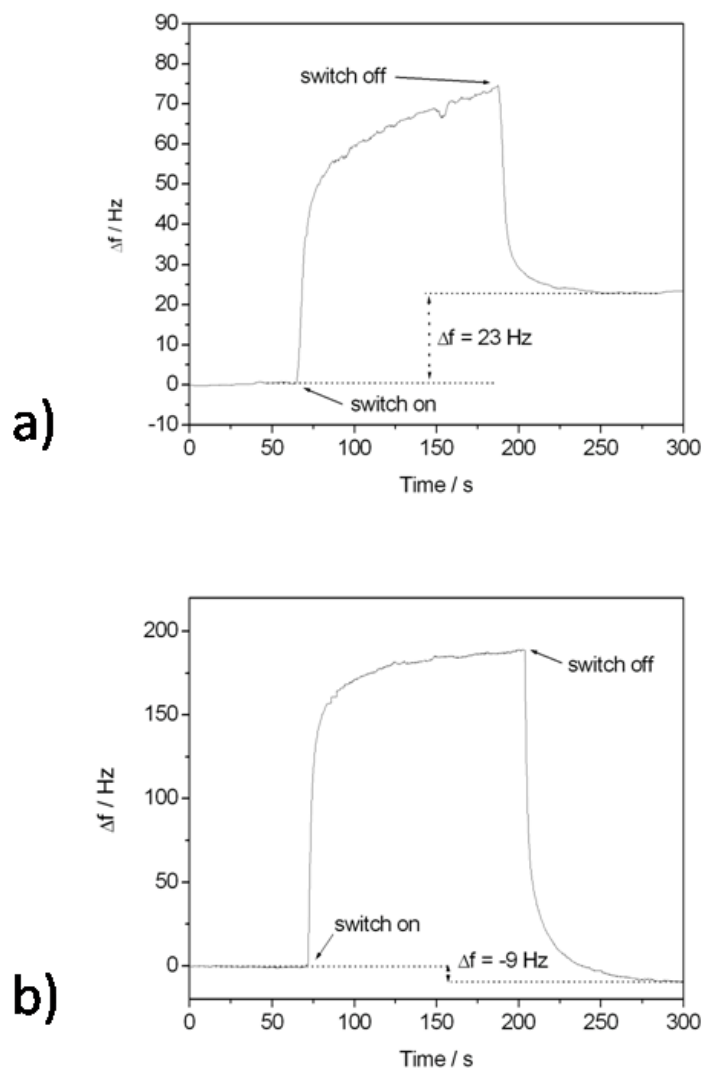


**Figure 5.5.:** QCM-transients during a) Ar/H<sub>2</sub>-plasma treatment and b) H<sub>2</sub>O-plasma treatment of an oxide covered Al-film.

During the H<sub>2</sub>O-plasma treatment the frequency is shifted negatively by 9 Hz indicating the increase of the oxyhydroxide film thickness in agreement with the in-situ FT-IRRAS data (figure 5.4). Assuming a density of the oxide of  $3.98 \text{ g} \times \text{cm}^{-3}$  the frequency change would correspond to an increase of the oxide thickness by 0.29 nm.

## 5. Formation and Stability I

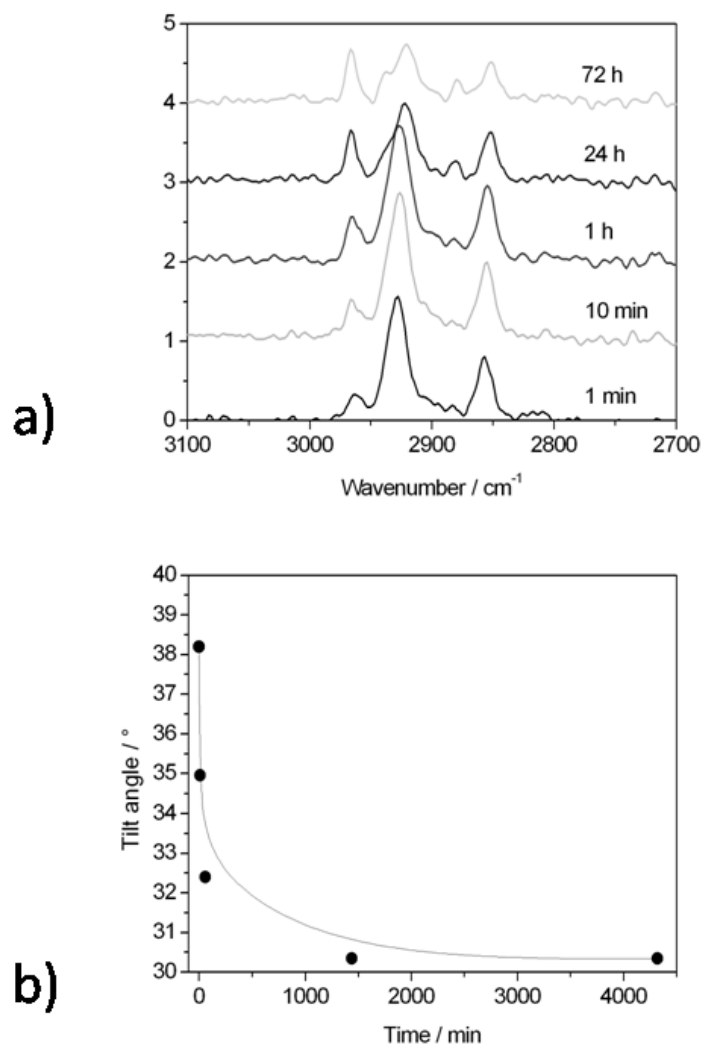


**Figure 5.6.:** Peak area ratio of the asymmetric stretching vibration bands of CH<sub>2</sub> and CH<sub>3</sub> illustrating the time dependence of the self organization process.

### 5.3.3. Adsorption of Octadecylphosphonic Acid on the Oxide Covered Aluminum

The adsorbed ODPA monolayers on oxide covered aluminum were characterized ex-situ by means of PM-IRRAS. In figure 5.6 a) the obtained

## 5. Formation and Stability I

spectra are shown. With increasing time of adsorption, the CH<sub>2</sub> bands decrease while the CH<sub>3</sub> bands increase. For a rectangular adsorbed molecule no intensity would be expected for the CH<sub>2</sub> groups because of the missing transition dipole moment in the direction normal to the investigated surface. The change of the CH<sub>2</sub>/CH<sub>3</sub> peak area ratio, shown in figure 5.6 b), demonstrates the development of the self-assembly process. The organization process takes several days, the spectra in figure 5.6 b) show that the self-assembly of the film improves with the time of adsorption and after 72 h the organization process is close to the reachable optimum.

A geometrical estimation [130] from these ratios is

$$\frac{I_{CH_2}}{I_{CH_3}} = \frac{n \cdot 2 \cdot \cos \cdot (90^\circ - \alpha)^2}{3 \cdot \cos \cdot (35^\circ - \alpha)^2} \quad (5.1)$$

where  $I_i$  is the intensity of the according CH valence vibration bands,  $n$  accords to the CH chain length and is the angle between the alkyl chain axis and the surface normal. After 24 h of adsorption the alkyl chain has reached an angle of 31° with respect to the surface normal. During the self organization process, solvents surrounding molecules are ousted, the chains stretch and finally arrange densely packed. The final reached state is high stable by the strong van der Waals interactions. In relation to the corrosion it is expected that densely packed films improve the corrosion protection, as they inhibit for electrolytes to enter the metal surface effectively.

The PM-IRRAS data of the ODPa monolayer formed on the oxide covered aluminum surface are shown in two characteristic wavenumber regions. The missing P-O-H stretching vibrations and the presence of the PO<sub>3</sub><sup>2-</sup> stretching mode at 1089 cm<sup>-1</sup> in the spectrum indicate the deprotonation of the acid and the ionic bond formation between the phosphonate group and the Al<sup>3+</sup> ions in the surface.

The measurement of the water contact angle is one of the most sensitive techniques to probe the monolayer quality [140] [141]. The surface energy of the solid substrate can also be estimated by such measurements. The static contact angles of different liquids on the oxide covered aluminum surface and the ODPa monolayer covered surfaces shown in table 7.2 were measured as a basis for the calculation of the surface energy of the respective surface as shown in table 7.3. As described by Wenzel, the surface energy is generally related to the combined effects of

## 5. Formation and Stability I

surface chemistry and surface topography [142]. However, the deposited Al-films showed an extremely small roughness so that the topographic effect was negligible. In the case of the investigated ODPA monolayers,

**Table 5.2.:** Static contact angles of different liquids on the bare  $\text{Al}_2\text{O}_3$  covered surface Al-surface and ODPA monolayers adsorbed on the oxide covered surface.

	$\text{Al}_2\text{O}_3$	ODPA
<b>Water</b>	<b>60.6°</b>	<b>119.2°</b>
<b>di-iodomethane</b>	<b>49.5°</b>	<b>97.0°</b>
<b>ethylene glycole</b>	<b>45.6°</b>	<b>94.1°</b>

the main factors influencing the surface energy are the ordering as well as the homogeneity of the monolayers. The dense packing of the  $\text{CH}_3$  group terminated alkyl chain leads to a reduction of the surface energy to a value of  $11.2 \text{ mJ/m}^2$  (Table 7.3). This value and the contact angle of water of about  $119^\circ$  indicate the formation of a monolayer that completely covers the surface and exhibits well ordering. The strongly polar surface of the oxyhydroxide is converted to a completely unipolar surface.

**Table 5.3.:** Surface energy of  $\text{Al}_2\text{O}_3$  and ODPA calculated by the contact angle measurement.

<b>Energy [<math>\text{mJ/m}^2</math>]</b>	$\text{Al}_2\text{O}_3$	ODPA
$\gamma^p$	<b>20.3</b>	<b>0.4</b>
$\gamma^d$	<b>20.7</b>	<b>10.8</b>
$\gamma$	<b>41.0</b>	<b>11.2</b>

### 5.3.4. Dependence of the Adsorption Isotherms of $\text{D}_2\text{O}$ on the Surface Chemistry

Figure 5.7 shows the comparison of the adsorption isotherms of  $\text{D}_2\text{O}$  on ODPA monolayer covered  $\text{H}_2\text{O}$  plasma treated aluminum films. Prior to the measurements, the chamber was purged with dry nitrogen leading to a measured relative humidity of less than 5 %. After reaching a stable frequency with no detectable shift over more than 60 minutes the relative

## 5. Formation and Stability I

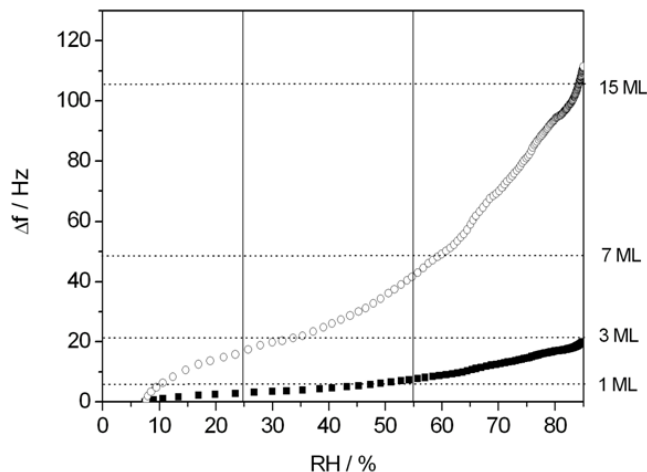


**Figure 5.7.:** Illustration of the adsorption isotherms of  $D_2O$  on a bare hydroxylated oxide covered aluminum film (white dots) and such a surface covered with a monolayer of ODPA (black dots) (left ordinate: frequency change, right ordinate: equivalent monolayers of water assuming a monolayer density of  $0.32 \times 10^{15}$  water molecules per  $cm^2$ ).

humidity was increased by bubbling a nitrogen gas flow through three reservoirs of pure water. The resulting increase in the relative humidity was recorded directly at the exit of the in-situ cell. Simultaneously, the frequency change was recorded. It took about 60 minutes until the relative humidity in the chamber increased to a final value of about 80 %. In agreement with the literature, we considered one monolayer of water to cause a frequency change of 6 Hz for 10 MHz quartz crystals [125]. The difference in the induced frequency changes directly reflected the different amounts of  $D_2O$  adsorbed on the two surfaces. Both surfaces showed a BET like adsorption isotherm. However, the ODPA monolayer significantly reduced the slope of the isotherm and the resulting water layer thickness at high relative humidities.

For the hydrophilic surface, the isotherm determined from the QCM follows the typical BET isotherm curve of water. The measured data were in good agreement with previously reported data for other hydrophilic surfaces [119] [130]. In figure 5.5 b) three regions can be distinguished. Up to 25 % r.h. the adsorption isotherm increases rapidly and then

## 5. Formation and Stability I

retards corresponding to a Langmuir like behaviour. Above 25 % r.h. the multilayer formation starts.

For the hydrophobic ODPA covered surface the Langmuir type region extends up to relative humidities of 40 %. The reason for the reduced adsorption of surface water layers are the strongly reduced interaction energies between water and the methyl terminated aliphatic ODPA layer. No hydrogen bonds as in the case of the hydroxylated oxide surface can be formed and pure van der Waals forces influence the monolayer adsorption.

### 5.3.5. Self-Assembled Monolayer as Isotopic Barrier

In order to study if the reduced interaction of water with the ODPA modified surface is accompanied by an effective barrier property for water, a water plasma treated oxide covered aluminum surface and an additionally ODPA monolayer covered surface were subjected to a partial pressure of D<sub>2</sub>O of 0.3 *mbar*. The prepared samples were transferred to the in-situ FT-IRRAS chamber and the D<sub>2</sub>O partial pressure was adjusted to 0.3 *mbar*. By time resolved FT-IRRAS measurements the isotopic exchange on both surfaces was monitored. In figure 5.8 the comparison of the development of the intensities of the O-D and O-H vibration are shown. The triangular hollow data points in figure 5.8 show the evolution of the  $\nu(\text{OD})$  peak at 2550  $\text{cm}^{-1}$  of the bare oxide surface. The isotopic exchange process comes to saturation within about 3 hours for the bare oxide covered surface. The ODPA monolayer did not significantly inhibit the proton exchange reaction keeping considering that the exact hydroxyl amount after the adsorption of ODPA on the surface is not well known. At least no significant delay in the proton exchange was observed. However, the constant signal of the CH-peak (see figure 5.8) and the unchanged phosphonate peak form and intensity show that the water adsorption does not lead to any de-adhesion of the organophosphonate monolayer. Only after the plasma etching step the monolayer is completely removed. Figure 5.9 shows the IRRAS measurement after D<sub>2</sub>O plasma treatment and exchange reaction which indeed corresponds to the last data points of the phosphonate covered oxide in figure 5.8. In the region of 2750 – 3050  $\text{cm}^{-1}$  the negative peaks belongs to symmetric and asymmetric vibrations of the CH<sub>2</sub> chain with CH<sub>3</sub> termination due to the removal of the monolayer. Additionally, the removal of phosphonate groups are assigned to the broad peak centered at 1100  $\text{cm}^{-1}$  as seen on

## 5. Formation and Stability I

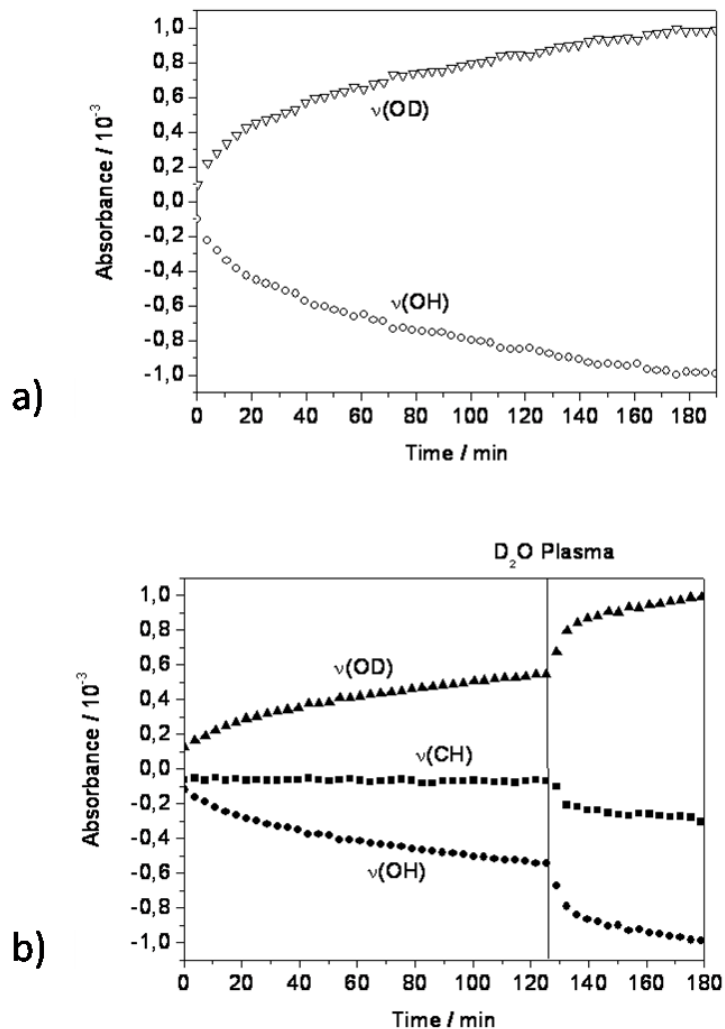


**Figure 5.8.:** D<sub>2</sub>O adsorption on bare (a) and ODPA covered (b) aluminum surfaces measured by means of time resolved in-situ IRRAS. In case of the ODPA covered surface a plasma etching step of 120 s was undertaken to remove the monolayer.

figure 5.9. A desorption/adsorption mechanism as possible mechanism for the isotopic exchange of H<sub>2</sub>O/D<sub>2</sub>O in the AlO(OH) surface through the barrier of a self-assembled monolayer cannot be excluded based of the constant ODPA infrared signal during the ongoing exchange since

## 5. Formation and Stability I

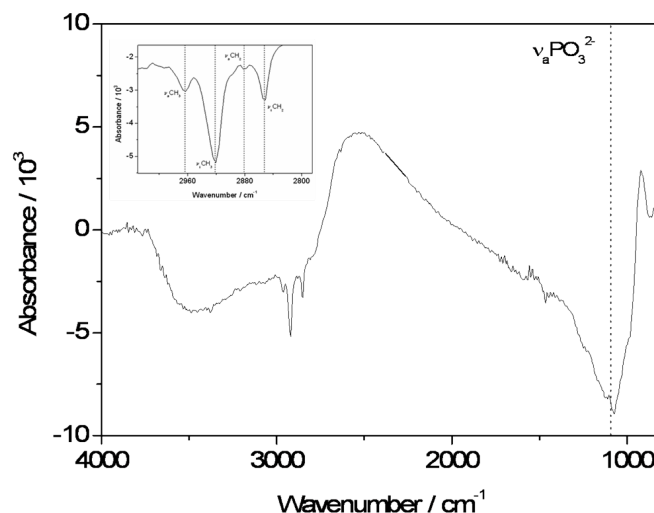


**Figure 5.9.:** IRRAS of phosphonate covered surface after treatment with  $D_2O$  plasma. Negative peaks belonging to the vibrations of the removed hydrocarbon and phosphonates.

the time to measure a spectrum is orders of magnitude larger than the expected interfacial reactions. Most importantly, although the less than two nanometer thin well ordered monolayer cannot inhibit the diffusion of water to the hydrophilic oxide surface no resulting desorption at the high water activities is observed.

### 5.4. Conclusions

The combined in-situ FT-IRRAS and QCM measurements allowed the evaluation of the barrier properties of ODPA monoalyers and the influence on the water isotherm formation on the ODPA surface. Both aspects are of high relevance for adhesion phenomena related to organophosphonates.

Measurements by means of the QCM revealed the significant decrease of the slope of the water adsorption isotherm on oxide covered aluminum induced by the adsorbed ODPA monolayer. This behaviour could be explained by the low surface energy of the well ordered ODPA film and

## 5. Formation and Stability I

the negligible polar component of its surface energy. Ex-situ and in-situ FT-IRRAS measurements proved the self assembly of the ODPA monolayer and the interfacial ionic bond formation between the phosphonate and Al-ions.

While the water layer can be significantly reduced the proton exchange based on a diffusion of water through the monolayer can not be effectively inhibited. However, even though an increased water activity is occurring in the neighborhood of the phosphonate group binding to surface Al-ions no protonation and no de-adhesion of the monolayer was observed. This proves that the stability of organophosphonates on Al-oxide surfaces is based on the high interfacial bond strength in humid environments and rather not on the barrier properties of the attached alkyl chains.

Much work has been done to get at the binding mechanism at the interfaces of aluminum and phosphonic acids. Interpretation of the actual presented work clearly has proved the deprotonated state of the ODPA being adsorbed on the aluminum surface. Furthermore water was no more able to reprotonate the ODPA.

### 5.5. Outlook

The in-situ working techniques which have been shown up in this chapter can easily be transferred to other interfaces. The crystals of the QCM are cheap and can be equipped by PVD techniques with many metal and oxide surfaces. Thus, kinetics of SAMs will be an interesting working field for the future any way.

# 6. Formation and Stability of Phosphonic Acid Self-Assembled Monolayers on Amorphous and Single Crystalline Aluminum Oxide Surfaces in Aqueous Solution

## 6.1. Introduction

Molecular adhesion forces at interfaces between organic coatings or adhesives and engineering metals are governed by physisorption or chemisorption of macromolecules or adhesion promoting additives on these passive film surfaces. In this context an understanding of the surface chemistry as well as molecular binding mechanisms on a fundamental level is important for adhesion promotion on oxide covered metal substrates [143] [144]. As almost all engineering metals are covered by a native oxide film, especially the combined understanding of the structure of these oxide films as well as their corresponding interface chemistry in the presence of macromolecules is of crucial importance for the design of polymer/metal composites [145] [146] [147]. Aluminum alloys, which are covered by a passive oxide film, are used in wide range of applications ranging from the aviation industry, to automotive and construction industry. Adhesive joining of such alloys and the application of organic coatings for corrosion protection is of high technological importance [146] [149].

The adsorption of phosphonic acid self-assembled monolayers on aluminum oxide surfaces is of substantial interest, because  $\alpha$ - $\omega$ -bifunctional phosphonate monolayers have been shown to act as adhesion promoting molecules [146]. The bifunctionality enables the binding of the phospho-

## 6. Formation and Stability II

nic acid or its anion to the oxide surface while the second group (e.g. amine or epoxy) leads to a chemical binding reaction with the organic phase of the adhesive or coating. It could be shown that for oxide covered aluminum alloys organo-phosphonic acids form very stable monolayers on aluminum alloys covered with an amorphous thin oxide film [147]. Several recent studies focussed on engineering aspects of the related interfacial chemistry [148] [149] [150]. It could be shown that the adsorption rate of ODPa is strongly depending on the OH-density of the surface which can be influenced by plasma modification [150]. Maeger et al. investigated the adhesion of the different organophosphonates on aluminum alloys and assumed an acid-base interaction with a tridentate binding [150]. Wapner et al. used short a chain aminopropylphosphonic acid (APPA) as adhesion promoting molecule on aluminum alloy surfaces and showed that they can be also used as additives in adhesives [148].

Despite the considerable interest in phosphonic acid based adhesion promoters, only very few investigations have been focussing on a fundamental understanding of the chemical binding of phosphonic acids to aluminum oxide surfaces and their long term stability against desorption in competition with water. However, one of the most important step towards an improvement of adhesive technology based on phosphonate adhesion promoters is necessarily to deeply understand the binding mechanisms on different oxide surfaces as well as the kinetics of individual processes taking place during the self-assembly as well as during ageing and de-adhesion of phosphonic acid interfacial layers. In this context, the stability of the formed monolayers in the presence of high water activities is of high practical interest for improving wet-adhesion and corrosion resistance. Water adsorption as such has been studied quite intensively on the different single crystal aluminum oxide surfaces by theoretical [151, 152, 153] as well as experimental studies [154] [155].

However, the focus of the here presented study was to improve the knowledge of the binding of organophosphonic acid molecules on aluminum oxide surfaces by studying a selected series of aluminum oxide surfaces with distinctly different morphologies and atomic structures. The combined study of two different amorphous surfaces oxide films on aluminum and gold as well as two different single crystalline Al-oxide surfaces with respect to the adsorption and desorption of ODPa SAMs allowed a differential understanding of the interfacial binding and de-sorption mechanisms in aqueous environments.

## 6.2. Experimental

### 6.2.1. Sample Preparation

Four different types of aluminum oxide surfaces were used and coated with a monolayer of ODPa molecules. All chemical reagents were of analysis grades and were used without any further purification unless mentioned else wise in the text. The different sample types were prepared as follows:

**Type 1:** Pure aluminum samples (Al 99.99%) were prepared by melting and casting the metal under argon atmosphere. Afterwards, the samples were cut into pieces of  $10 \times 10 \times 3 \text{ mm}^3$  and the surface was polished with diamond paste of a corn radius of  $1 \mu\text{m}$  and ultrasonically cleaned in abs. ethanol (> 99.9%, Merck, Germany) for 10 minutes. After rinsing with ethanol the samples were dried in a stream of nitrogen.

**Type 2:** Pure aluminum oxide layers were deposited onto Au-coated (100 nm, with an adhesion promotion layer of 2 nm Cr) silicon wafer substrates by means of PVD of  $\text{Al}_2\text{O}_3$  (Univex 450, Leybold AG). During the evaporation the layer thickness was monitored by a QCM (Inficon XTC). Prior to film deposition the samples were thoroughly cleaned in a mixture of hydrogen peroxide (30%, Merck, Germany) and ammonia (25%, Merck, Germany) (1 : 1) for 60 minutes at  $80 \text{ }^\circ\text{C}$ , afterwards rinsed with de-ionized (DI) water and dried in a stream of nitrogen. To ensure a completely oxidated aluminum layer, the samples were further treated with an oxygen plasma after the deposition.

**Type 3-4:** Sapphire wafers with the surface orientation (0001) and (1 – 102) were purchased from Mateck (Mateck GmbH, Germany). Before annealing the crystals were immersed into 85% phosphoric acid for 1 minute, rinsed with deionized water and dried in a stream of nitrogen. The sapphire crystals were then annealed in ambient air at  $1400 \text{ }^\circ\text{C}$  for 24 h. For the polar surfaces these annealing conditions were shown to give aluminum terminated  $\text{Al}_2\text{O}_3(0001)$  surfaces and hydroxide stabilized surfaces [176] [177]. The annealing procedures were leading to surfaces with large terraces as evidenced by AFM. Low energy electron diffraction (LEED) confirmed the atomic scale ordered structure on these surfaces.

## 6. Formation and Stability II

XPS-spectra in figure 6.1 show a comparison of the  $O1s$  core-level spectra at  $10^\circ$  takeout angle of the photoelectrons for as-prepared surfaces. Two species of oxygen - in the form of hydroxide and of oxide - were detected for all surfaces, showing that all surfaces have a comparable composition in terms of hydroxide to oxide ratio.

The ODPA monolayers on these four types of aluminum oxide surfaces were prepared by solution self-assembly under ambient conditions. Substrates were ultrasonically cleaned in abs. ethanol ( $> 99.9\%$ , Merck, Germany) for 10 minutes before immersing into a  $1\text{ mM}$  ethanolic solution of ODPA for  $24\text{ h}$ . Afterwards the samples were thoroughly rinsed with ethanol and dried in a stream of nitrogen.

### 6.2.2. Static Contact Angle Measurements

The static contact angle of water was measured by means of the sessile-drop method using an OCA 20 goniometer (Dataphysics, Germany). The reported contact angles were measured at five different locations on each sample with DI-water and the averaged values are reported.

### 6.2.3. Atomic Force Microscopy

AFM topography experiments were performed with a JPK NanoWizards AFM (JPK Instruments AG, Berlin, Germany) in a dry nitrogen atmosphere using a custom-made liquid-cell that allows perfect control of the environment. The system is equipped with a homemade anti-noise and -vibration box, which enables perfect conditions for imaging with a very low noise level. The z-piezo of the AFM was calibrated with a 1-D array of rectangular  $\text{SiO}_2$  steps with a height of  $18.6\text{ nm}$  (TGZ01 from  $\mu$ -Masch). The xy-piezoes were internally calibrated with integrated capacitive position sensors. The in-situ images were recorded in constant force and constant amplitude mode using silicon sensors (CONTR obtained from NanoWorld, typical tip radius less than  $10\text{ nm}$ ,  $k = 0.1 - 0.3\text{ N/m}$ ). In constant force mode the force set-point was allowed to be at maximum  $2\text{ nN}$  in order to minimize any scanning induced effects. In constant amplitude mode the amplitude was damped to  $90\%$  with respect to the free amplitude.

#### 6.2.4. Polarization Modulation Infrared Reflection Absorption Spectroscopy

PM-IRRAS measurements were performed on a step scan interferometer (Bruker Vertex 70) at a resolution of  $4\text{ cm}^{-1}$  and  $80^\circ$  relative to the substrate surface normal. For p-polarization of the IR light an aluminum wire grid was used and modulated at  $100\text{ kHz}$  with a ZnSe Photo-Elastic-Modulator (PEM, Bruker PMA-50). Light reflected from the sample was focused with a ZnSe lens onto a cryogenic mercury cadmium telluride (MCT) detector. All presented spectra were recorded from 512 single scans. As reference a respective clean alumina surfaces was used as background and subtracted from the sample data.

#### 6.2.5. Diffuse Reflectance Infrared Fourier Transform Spectroscopy

DRIFT measurements were performed with the Harrick Praying Mantis measurement cell continuously floated with nitrogen, in a Bruker V70 spectrometer with a deuterated triglycine sulfate (DTGS) detector. As reference the respective clean sapphire surface was used as background and subtracted from the sample data. The resolution of the presented data is  $4\text{ cm}^{-1}$  and 512 scans were integrated for each measurement.

### 6.3. Results

The fundamental approach was to combine analytical studies of the adsorption as well as desorption of ODPa in competition with water on a series of selected aluminum oxide surfaces, which differ in their atomic arrangements and electronic structure. This concept allowed a comparative understanding of the interfacial chemistry between the adsorbing phosphonic acid and the aluminum oxide especially with respect to the competition with water adsorption on the oxide surface.

Two different amorphous surfaces, which only differed in the supporting bulk substrate, were studied. One system consisted of a native oxide film with a thickness of  $2 - 3\text{ nm}$  [156] as grown as a native passive film on aluminum under atmospheric conditions. For comparison a  $250\text{ nm}$  thick evaporated amorphous aluminum oxide film was deposited on a Au-coated silicon wafer surface. As single crystalline substrates, two dif-

## 6. Formation and Stability II

ferent single crystalline sapphire surfaces with a distinctly different local geometry of the atomic arrangements were used. The polar  $\text{Al}_2\text{O}_3(0001)$  surface and the non-polar  $\text{Al}_2\text{O}_3(1-102)$  surface were used [170] [171]. Both surface orientations were already discussed in the literature with an emphasis on the  $\text{Al}_2\text{O}_3(0001)$  orientation. The behaviour of adsorbed ODPa monolayers was analyzed on all these surfaces allowing for a comparative understanding of the adsorption and desorption chemistry even in competition with water.

The formation of the ODPa SAMs was characterized by means of PM-IRRAS on the amorphous films on metal substrates and DRIFTS on the single crystalline oxides. The desorption in aqueous solution was comparatively investigated by means of AFM, static contact angle measurements as well as DRIFTS and PM-IRRAS measurements. The results reproducibly revealed several results which can be rationalized in terms of the distinct differences of the oxide surface structures. In the following the results on the different surfaces are presented and finally commonly discussed in terms of a comparative study.

### 6.3.1. Adsorption of Octadecylphosphonic Acid Monolayers on Aluminum Oxide Surfaces

In general, mean orientation, packing density and interfacial bond formation of the self assembled monolayer can be analyzed by means of grazing incidence FTIR spectroscopy. In the present case PM-IRRAS is suitable for the analysis of ODPa monolayers on aluminum oxide films on a metal substrate. Therefore, sample type 1 and 2 could be analyzed by PM-IRRAS. For ODPa monolayers on single crystalline oxide surfaces diffuse reflectance spectroscopy was performed. This method allows for the analysis of the interfacial bond formation as well. In contrast to PM-IRRAS, this technique does not contain information about the orientation of the self-assembled molecules [178]. In the following section the spectra of ODPa monolayers formed on the four types of substrates are discussed. Spectra of the adsorbed films were compared to spectra of the free phosphonic acids measured by means of ATR. The respective FTIR spectra are presented in figure 6.2. The peak assignments are listed in table 6.1.

## 6. Formation and Stability II

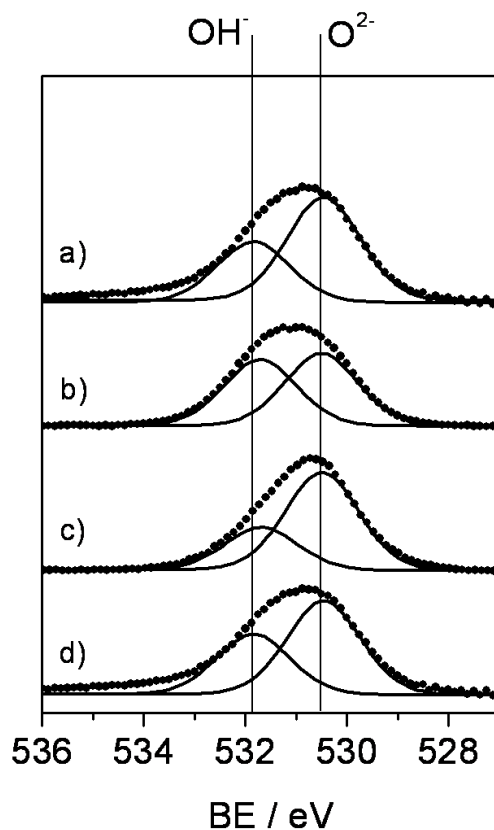


**Figure 6.1.:** XPS data analysis focused on the hydroxide to oxide ratio. For this reason the C1s peak of the aliphatic groups was shifted to a binding energy of 285 eV. The figure shows the O1s core level spectra of a native oxide covered aluminum surface (a), a physical vapor deposited oxide covered aluminum surface (b), of a single crystalline Al<sub>2</sub>O<sub>3</sub>(0001) surface (c), and of a single crystalline Al<sub>2</sub>O<sub>3</sub>(1-102) surface (d). The measured O1s transition envelopes several peaks with different binding energies due to different chemical environments. The O<sup>2-</sup>-contribution of the oxide and the OH<sup>-</sup>-contribution of the hydroxide appear in the range of 530 – 534 eV. In accordance with the literature an excellent curve fitting was obtained with symmetric components of equal full width at half-maximum (fwhm).

## 6. Formation and Stability II

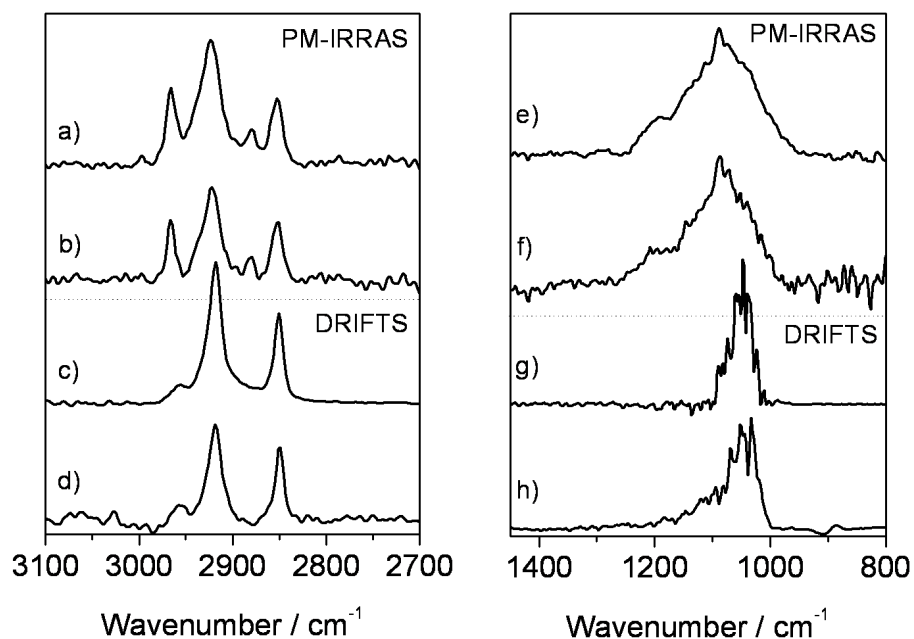


**Figure 6.2.:** a,e) PM-IRRAS data of an ODPA monolayer adsorbed on oxide covered aluminum in the corresponding wavelength regions; b,f) show the PM-IRRAS spectrum of an ODPA monolayer adsorbed on PV deposited aluminum oxide; c,g) DRIFTS data of ODPA adsorbed on a  $\text{Al}_2\text{O}_3(0001)$  single crystal, corresponding wavelength regions; d,h) show DRIFTS of monolayer on  $\text{Al}_2\text{O}_3(1-102)$  single crystal surface.

6. Formation and Stability II

**Table 6.1.:** Assignment for FTIR-peaks as observed in the spectra in figure 6.2. All values are given in  $cm^{-1}$ .

Vibration Mode	PM-IRRAS of ML on native oxide covered Al	PM-IRRAS of ML on PVD oxide covered Al	DRIFT of ML on Al <sub>2</sub> O <sub>3</sub> (0001)	DRIFT of ML on Al <sub>2</sub> O <sub>3</sub> (1 – 102)	Lit.
$\nu_{as}(\text{CH}_3)$	2965	2966	2957	2958	[149, 150]
$\nu_{as}(\text{CH}_2)$	2923	2922	2918	2918	[149, 150]
$\nu_{as}(\text{CH}_3)$	2880	2879	-	-	[149, 150]
$\nu_s(\text{CH}_2)$	2853	2853	2850	2849	[149, 150]
$\nu(\text{P} = \text{O})$	1194	1207	-	1190	[149, 150]
$\nu(\text{P} - \text{O})$	1129	1137	-	1121	[149, 150]
$\nu_{as}(\text{PO}_3^{2-})$	1089	1085	1087	1069	[149, 150]
$\nu_s(\text{PO}_3^{2-})$	1046	1039	1049	1031	[149, 150]

## 6. Formation and Stability II

PM-IRRAS data of the ODPa monolayer on native-grown, oxide covered aluminum 6.2, a,e and aluminum oxide on gold substrate 6.2, b,f clearly show that ODPa could be immobilised as an organophosphonate self-assembled monolayer on these oxide surfaces. The spectral region of the CH<sub>2</sub> and CH<sub>3</sub> stretching vibrations shows, that the peak ratio  $A(\text{CH}_3)/A(\text{CH}_2)$  is significantly increased in the adsorbed state in comparison to a bulk spectrum of ODPa [149] [150]. This is a clear indication that the ODPa is not only forming a monolayer but that a self-assembly process takes place leading to a mean upright orientation of the aliphatic chain of the ODPa. The mean inclination angle can be derived from the peak-ratio [162] and was calculated to be 30° for ODPa adsorbed on oxide covered aluminum. The mean orientation moreover indicates that the packing density is quite high which is confirmed by water contact angle measurements (see below).

Moreover the phosphonic acid functionality appears to be deprotonated. In 6.2, d it can be seen, that the peaks of the free acid group (P – OH), which would appear in the range from 900 – 980  $\text{cm}^{-1}$  are clearly absent. For the further discussion the broad phosphonate band with a maximum at about 1089  $\text{cm}^{-1}$  was considered in more detail. It can be observed, that the stretching peaks of the P = O group and the PO<sub>3</sub>-group are present in the spectrum of all ODPa films adsorbed on amorphous alumina. In combination with the studied stability towards desorption in aqueous environment, which will be discussed in detail below, one specific type of binding towards the alumina surfaces is most plausible. We conclude that the binding on both of the amorphous alumina is mainly governed by mono- or bi-dentate condensation of the phosphonate onto the respective oxide surfaces, which is consistent with the disappearance of the P – OH vibrations and the detected P = O stretching vibrations. The DRIFT spectra of ODPa adsorbed on Al<sub>2</sub>O<sub>3</sub>(0001) and Al<sub>2</sub>O<sub>3</sub>(1 – 102) are presented in 6.2, c, g and 6.2, d, h, respectively. First, these spectra clearly indicate the immobilization of the phosphonate. Due to the physical principle of this scattering method the signal of the CH<sub>2</sub>/CH<sub>3</sub> vibrations within the range from 2800 – 3000  $\text{cm}^{-1}$  does not contain orientation dependent information. Nevertheless, the matching peak positions are a clear indicator for the immobilization of an ODPa self-assembled monolayer on both single crystal surfaces.

However, the spectral region of the phosphonate groups provides detailed information on the formed interfacial bonds as measured by DRIFTS.

## 6. Formation and Stability II

For the  $\text{Al}_2\text{O}_3(0001)$  surface the spectrum (6.2, g) indicates an interfacial bond formation based on ionic binding between the deprotonated phosphonic acid group and the Al-ions in the oxide surfaces, based on the disappearance of the peaks assigned to P – OH as well as P = O stretching vibrations. Only  $\text{PO}_3^{2-}$  stretching vibrations could be detected, which is consistent with an ionic binding mechanism. In contrast the spectra of the  $\text{Al}_2\text{O}_3(1 - 102)$  surface (6.2, h) still show the presence of the asymmetric P – O vibration as well as weak P = O stretching vibrations, indicating a similar type of binding as concluded for both amorphous aluminum oxide films. Based on the presented FTIR-data interfacial binding appears to be based on a purely ionic mechanism only on the  $\text{Al}_2\text{O}_3(0001)$  surface. On the other substrates the binding mechanism of ODPA is most likely based on a mono or bidentate condensation of ODPA onto the surfaces at suitable binding position.

### 6.3.2. Stability of Octadecylphosphonic Acid Self-Assembled Monolayers on Aluminum Oxide Surface in an Aqueous Environment

Molecular desorption of the self-assembled monolayers of ODPA was investigated by means of in-situ AFM, water static contact angle measurements, and FTIR-spectroscopy. In-situ AFM was performed to image changes of the topography of the ODPA SAM on the respective Al-oxide surface in an aqueous solution. The contact angle measurements were done to provide information on the average surface energy which reflects the coverage and degree of orientation of the adsorbed ODPA monolayers. FTIR measurements led to information on the amount of adsorbed ODPA after immersion in aqueous solutions and the degree of orientation in the case of PM-IRRAS data.

#### Characterization and Stability by Static Water Contact Angle Measurements

Contact angle measurements were used to confirm the formation of self-assembled film on the various substrates. For three types of samples the static contact angle after preparation of the SAM yielded high contact angles of  $115 - 120^\circ$ . Only the polar  $\text{Al}_2\text{O}_3(0001)$  surface was leading to a slightly lower value of  $108^\circ$ . This is consistent with recent observa-

## 6. Formation and Stability II

tion of Brukman et al. [173] who used similar preparation conditions of the crystal. Another study with differently pretreated crystals (shorter annealing time) gave lower values, which were assumed to result from different phases, which co-exist on the crystals [179]. In the present case the slightly lower value compared to the other substrates could be caused by a minority phase as well, which can however not be answered conclusively.

The stability of the self-assembled monolayers of ODPA with respect to competition with water on the studied substrate surfaces was investigated by measuring the contact angle as function of the immersion time in ultra-pure water. After each immersion step of 10 minutes duration, the samples were dried in a stream of nitrogen and the static water contact angle was measured characterising the state of the self-assembly film. The resulting contact angle transients are shown in figure 6.3.

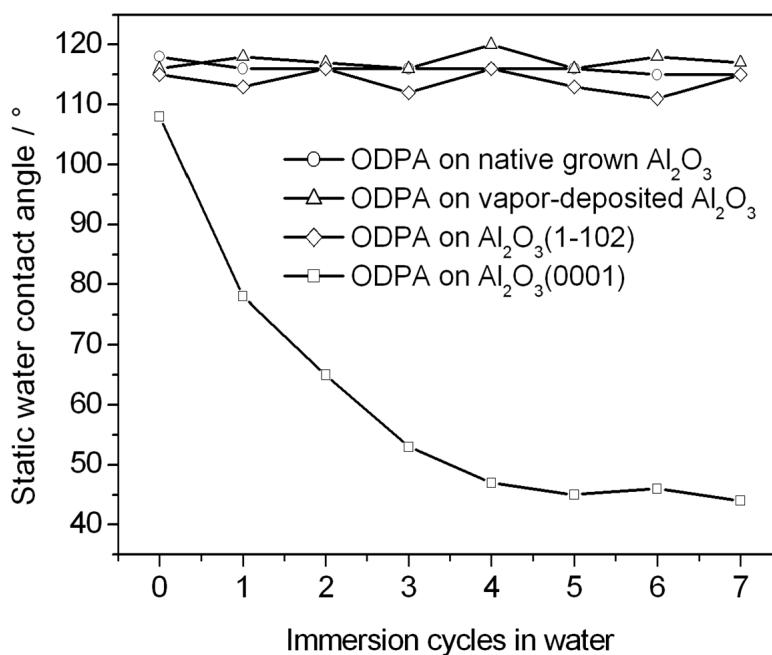


**Figure 6.3.:** Static contact angle of water for ODPA adsorbed on native grown  $\text{Al}_2\text{O}_3$  (circle), vapor-deposited  $\text{Al}_2\text{O}_3$  (triangle), single-crystalline  $\text{Al}_2\text{O}_3(1 - 102)$  (diamond) and single-crystalline  $\text{Al}_2\text{O}_3(0001)$  (square).

Obviously, the static water contact angle on the ODPA covered  $\text{Al}_2\text{O}_3(0001)$

## 6. Formation and Stability II

surface was observed to quickly decrease with the time of immersion, finally resulting in a contact angle of  $45^\circ$  which was about that for a bare  $\text{Al}_2\text{O}_3(0001)$  surface. In contrast, static water contact angle measurements obtained for ODPA covered surfaces of both amorphous oxide films and the  $\text{Al}_2\text{O}_3(1-102)$  orientation showed constant values of  $110-120^\circ$  over the tested time of immersion, indicating a stable functionalization with hydrophobic ODPA self-assembled monolayers. These measurements indicated that the hydrophobic ODPA monolayers after adsorption from ethanol solution form a dense and self-assembled monolayer as indicated by the water contact angles of  $110^\circ$  and higher. On the polar  $\text{Al}_2\text{O}_3(0001)$  surface the decrease of the contact angle indicates the dissolution of the ODPA monolayer into the aqueous phase or at least the severe deterioration of the ordered self-assembly film. For all other analysed surfaces, it was not even possible to decrease the contact angle by immersion in water and simultaneous exposure to ultrasonic acoustic irradiation.

### **Characterization of Octadecylphosphonic Acid Monolayer Stability by Means of in-situ Atomic Force Microscopy**

The in-situ microscopic studies aimed at a more detailed understanding how the ODPA films desorbed from the  $\text{Al}_2\text{O}_3(0001)$  surface. In-situ AFM studies of the ODPA monolayer stability in ultra-pure water perfectly imitated the situation of the immersion cycles (see above) and allowed for a nanoscopic investigation of the desorption mechanism or stability of the ODPA monolayer on the respective substrates. The imaging was done at room temperature and was always done according to the following protocol: First the surfaces were imaged in a solution of absolute ethanol, which does not lead to desorption of the self-assembled monolayer (the monolayer was formed in this solvent) [160]. Subsequently, ultra-pure water was introduced into the cell using a syringe pump. This setup allows for imaging at exactly the same position in different environments (the exact details of the setup were described elsewhere [161]). For the study of the desorption mechanism the water-flow was set to a constant value of  $500 \mu\text{l}/\text{min}$  (cell volume about  $500-700 \mu\text{l}$ ).

The first remarkable finding was, that the self assembled monolayer on the  $\text{Al}_2\text{O}_3(0001)$  surface was desorbing immediately after changing from ethanol to water. One has to keep in mind that the solubility of ODPA is much higher in ethanol than in water, which shows that the solubility in

## 6. Formation and Stability II

this case does not cause such a desorption process. However, as shown in the following the low solubility of ODPA in water influence the desorption path-way. Topographically, the desorption process could obviously be detected by the formation of islands on the whole surface as can be seen in figure 6.4, B. Most islands have a height of about 2.3–2.5 *nm* corresponding to the expected height of the self-assembly film. This clearly indicated residuals of the self-assembly film. Interestingly, some of these islands are spherical in shape and have a height of exactly two times the length of an ODPA molecule indicating the formation of micelle-like structures at the oxide/water interface; with one ODPA-layer binding to the surface with the phosphonic acid functionality and one physisorbed ODPA-layer on top with the phosphonic acid pointing into the solution leading to a hydrophobic alkyl chain-core, as depicted in the model in figure 4. Moreover, the height histogram in figure 6.4 shows, that these micelle-like islands are typically about 50 – 60 *nm* wide. This proves, that the adsorption of the ODPA in competition with water is clearly unfavourable on this polar surface, supporting the contact angle measurements. Moreover, the formation of the micelle-like islands, which stay adsorbed at the interface clearly reflects that ODPA cannot dissolve easily into water due to the nonpolar character of the alkyl chain. Hydrophobic interactions between alkyl-chains are consequently more favourable compared to adsorption of the phosphonic acid functionality onto the surface. In competition with water the ODPA molecules can dissolve into the aqueous phase, however due to the low solubility they immediately form a second layer on the pre-existing ODPA-SAM and stay physisorbed. In order to further support this assumption the dielectric constant of the medium was lowered again by returning to an ethanol solution. It was observed, that the micelle-like islands disappeared after changing to ethanol solution as can be seen in figure 6.3, B. This clearly reflects the fact that the formed ODPA micelles can be dissolved easily into ethanol solutions under such non-equilibrium conditions of a continuous flow. In contrast to the in-situ observations on Al<sub>2</sub>O<sub>3</sub>(0001) surfaces all other aluminum oxide surfaces did not show any formation of micelle-like islands at the interface to the aqueous phase. No desorption of the ODPA molecules could be observed for any of the other aluminum oxide surfaces with the AFM as can be seen in figures 6.5 and 6.6 for the other sample types proving the contact angle studies. Interestingly, ex-situ force-modulated AFM-images of native oxide sur-

## 6. Formation and Stability II

faces on aluminum before and after immersion in water for 10 minutes showed differences in the topography as well as phase shifts. In figure 6.5, C, D a comparison of AFM topographies for a native aluminum ox-

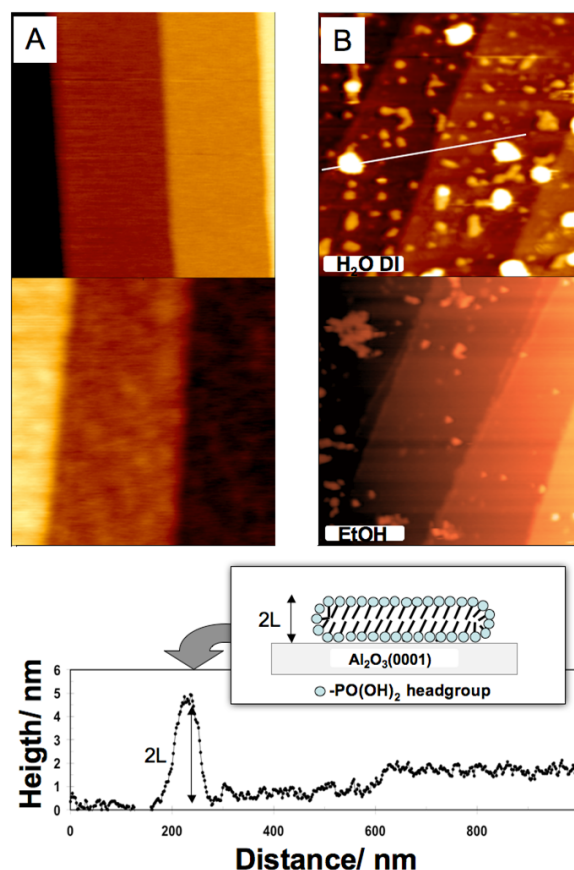


**Figure 6.4.:** All images are  $1\mu\text{m}^2$ . (A) AFM-topography of a single-crystalline  $\text{Al}_2\text{O}_3(0001)$  surface (top) with and (bottom) without ODPA-SAM (both taken in EtOH). The step-heights are typically about  $1\text{ nm}$ . (Btop) In-situ AFM topography of ODPA-covered  $\text{Al}_2\text{O}_3(0001)$  single crystal surface in water indicates formation of micelle-like ODPA-bilayer islands at the solid/liquid interface as indicated by the height histogram and within the model at the lower left corner. (Bbottom) Consequent in-situ imaging in ethanol solution revealed that these micelle-like islands can be dissolved.

## 6. Formation and Stability II

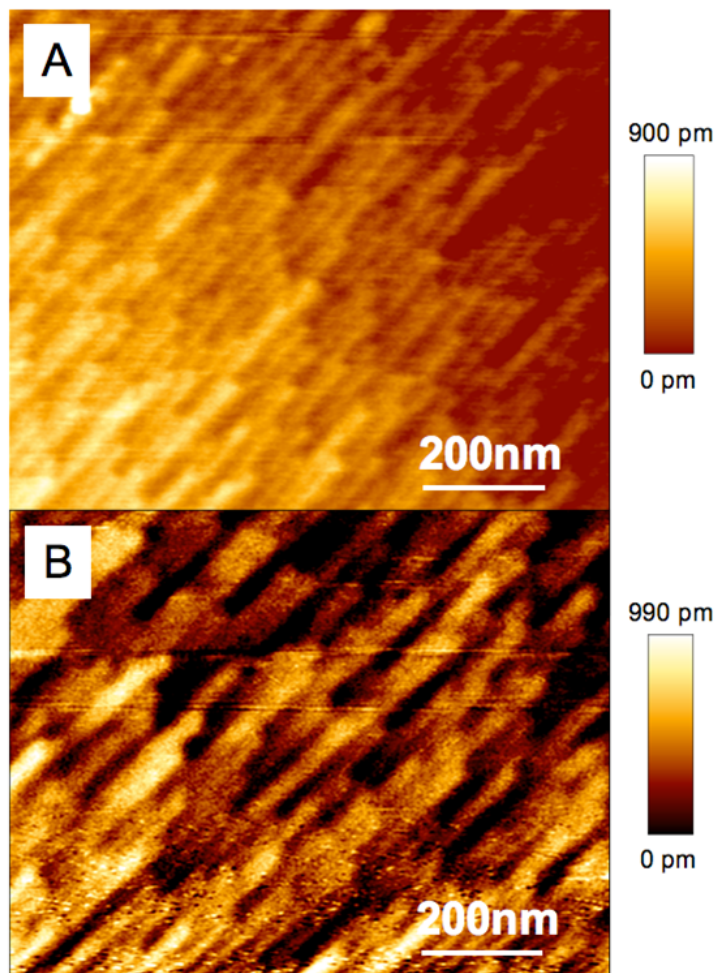


**Figure 6.5.:** (A) AFM-topography of a single-crystalline  $\text{Al}_2\text{O}_3(1-102)$  surface with ODPA-SAM recorded in EtOH. (B) AFM-topography of a single-crystalline  $\text{Al}_2\text{O}_3(1-102)$  surface with ODPA-SAM recorded after changing into aqueous medium. No significant structural differences or micelle formation could be detected.

ide surface covered with ODPA before and after immersion into water is shown. The AFM results clearly show a difference in surface topography. We interpret such a topographic change as a result of the diffusion of water and oxygen through the monolayer towards the interface inducing an increase of the passive film thickness. Since the contact angle did

## 6. Formation and Stability II

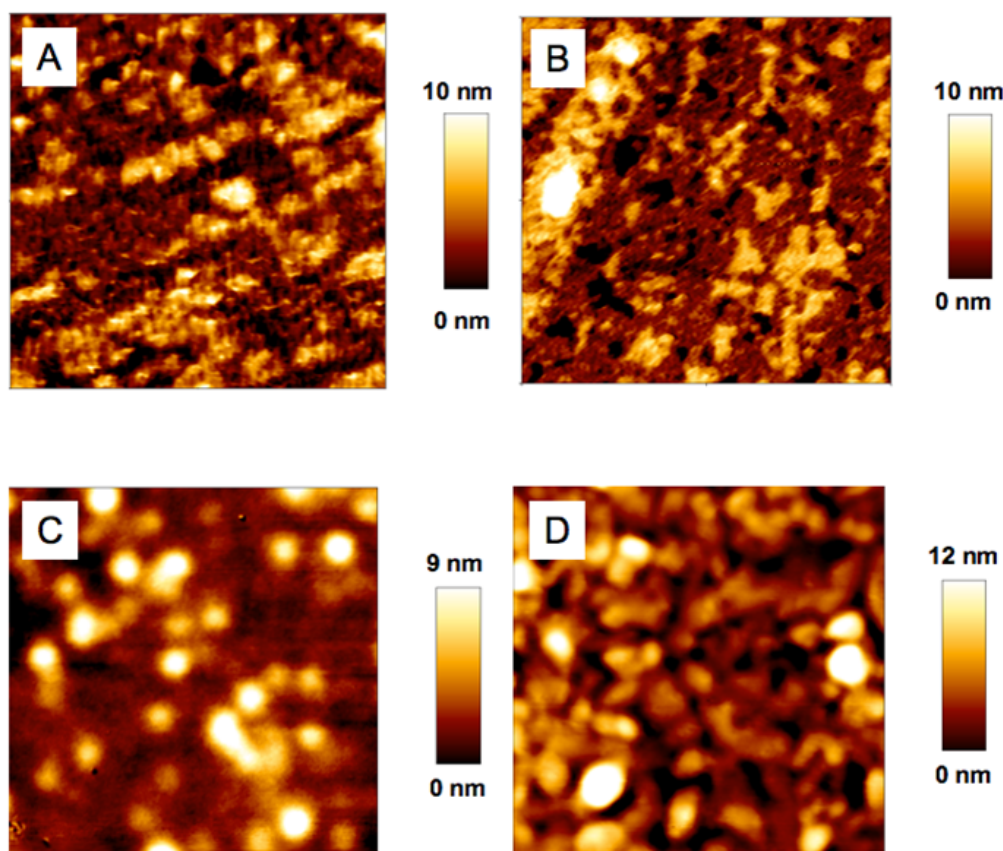


**Figure 6.6.:** (A) AFM-topography of an amorphous  $\text{Al}_2\text{O}_3$  surface with ODPA-SAM. (B) AFM-topography of an amorphous  $\text{Al}_2\text{O}_3$  surface with ODPA-SAM recorded after changing into aqueous medium. No significant structural differences or micelle formation could be detected. (C) AFM-topography of a native  $\text{Al}_2\text{O}_3$  surface grown on bare aluminum covered with ODPA-SAM as recorded in EtOH. (D) AFM-topography of the native grown  $\text{Al}_2\text{O}_3$  after immersing into water. The surface topography was changing significantly, leading to a roughening of the surface morphology. However, no micelles could be detected in-situ. In comparison with the IR and contact angle data, this may indicate a possible corrosive attack at the Al/ $\text{Al}_2\text{O}_3$  interface.

## 6. Formation and Stability II

not change and thereby indicated that ODPA is not desorbed from the surface, the growth of the oxide film below the ODPA monolayer seems to occur at the  $\text{Al}_2\text{O}_3/\text{Al}$ -interface [149].

Consequently, the reported AFM results support the conclusions of the static contact angle measurements, showing that ODPA desorbs only from the polar  $\text{Al}_2\text{O}_3$  (0001) surface. On the other studied surfaces the ODPA is immobilized on the surface even in competition with water.

### 6.3.3. Fourier Transform Infrared Spectroscopy of Octadecylphosphonic Acid Covered Surfaces after Immersion in Water

The progressive loss of surface coverage could be further confirmed by monitoring the intensity reduction of the characteristic peak heights of the FTIR spectra. As shown in figure 6.7, a, DRIFT spectra were measured for the ODPA monolayer formed on the  $\text{Al}_2\text{O}_3(0001)$  surface before and after several immersion cycles in water. After the immersion of the SAM in water, the intensity of the peaks corresponding to methylene stretching vibrations was reduced to approximately 20% of the initial intensity. This observation is consistent with the AFM and contact angle measurements, which show monolayer desorption over time with some ODPA remaining on the surface in island like structures (see figure 6.3). In contrast, FTIR spectra, which have been obtained for SAMs of ODPA on the other substrates before and after immersion did not show a significant decrease in the peak intensity. In figure 6.6,b the PM-IRRA spectra are shown for the ODPA film on native amorphous  $\text{Al}_2\text{O}_3$  covered aluminum. After the immersion of the SAM in DI-water the peak height of the  $\text{CH}_2$ -stretching vibrations were increased while the  $\text{CH}_3$ -peak areas kept almost constant. The increase in the  $\text{CH}_2$  to  $\text{CH}_3$  peak ratio indicates that the mean tilting angle of the self-assembly increases from  $30^\circ$  before immersion towards  $34^\circ$  after immersion.

## 6. Formation and Stability II

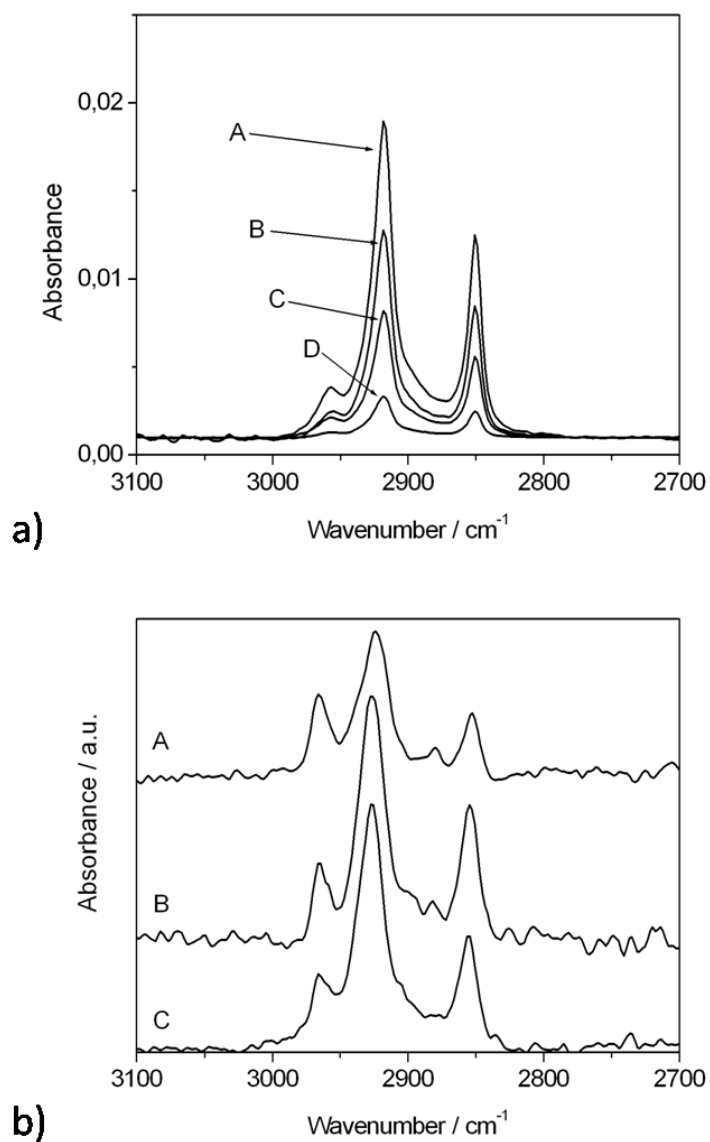


**Figure 6.7.:** a) DRIFT spectra of ODPA adsorbed on single-crystalline Al<sub>2</sub>O<sub>3</sub>(0001) before (A) and after one (B), two (C) and after three (D) water immersion cycles; b) PM-IRRAS spectra of ODPA adsorbed on native grown Al<sub>2</sub>O<sub>3</sub> on aluminum before (A), after (B) one and after (C) three water immersion cycles.

## 6.4. Discussion

The intriguing question is, why ODPA cannot be adsorbed stable onto polar  $\text{Al}_2\text{O}_3(0001)$  surfaces in competition with water but on all other investigated surfaces the binding is stable towards water immersion or at least the surface remains the high hydrophobicity which indicates the immobilisation of ODPA at the surface. We think that the three main arguments can explain these distinct behaviours; adsorption free energies of ODPA in competition with water, adsorption geometries and resulting interfacial bonding types:

First, first principles thermodynamics [153] and molecular dynamics [151] both predicted that a fully hydroxylated  $\text{Al}_2\text{O}_3(0001)$  surface can be expected as equilibrium termination at high water chemical potentials, which is in good agreement with experimental studies [163]. Calculated as well as experimental adsorption energies of water on the Al-terminated  $\text{Al}_2\text{O}_3(0001)$  surface consistently revealed quite high values in the range of 1.1 eV per water molecule. In comparison, on metal surfaces typically adsorption energies of water are ranging in between 0.1 – 0.4 eV/ $\text{H}_2\text{O}$  [164] [165]. On other oxide and hydroxylated oxide surfaces like e.g.  $\text{TiO}_2$ , -quartz, cristobalite or kaolinite surfaces values of 0.4 eV/ $\text{H}_2\text{O}$  [166], 0.5 eV/ $\text{H}_2\text{O}$  [167], 0.5 – 0.7 eV/ $\text{H}_2\text{O}$  [168] and 0.57 eV/ $\text{H}_2\text{O}$  [169] have been reported, respectively. The very high values for the  $\text{Al}_2\text{O}_3(0001)$  surface clearly indicate the highly favourable adsorption of water on the aluminum terminated  $\text{Al}_2\text{O}_3(0001)$  surfaces leading to fully hydroxylated surfaces. Therefore, the adsorption of water on these  $\text{Al}_2\text{O}_3(0001)$  surfaces is energetically strongly favourable and the resulting hydroxylated surfaces can be considered to be thermodynamically extremely stable [153]. Unfortunately, no values for the adsorption (free) energies of phosphonic acids on the aluminum terminated and hydroxid-stabilized surfaces are available. From our experimental results we however conclude, that the adsorption free energy of phosphonic acids onto the aluminum terminated surface as well as onto the hydroxylated polar  $\text{Al}_2\text{O}_3(0001)$  surface is considerably lower compared to the adsorption energy of water, leading to a desorption of the self-assembly film. Second, even though there is no thermodynamic data available for the adsorption of ODPA or some other phosphonic acid an examination of the surface geometry can give a first indication why the adsorption energies on the polar surface are much lower in comparison to the other surfaces by simply evaluating the possible steric arrangement of phos-

## 6. Formation and Stability II

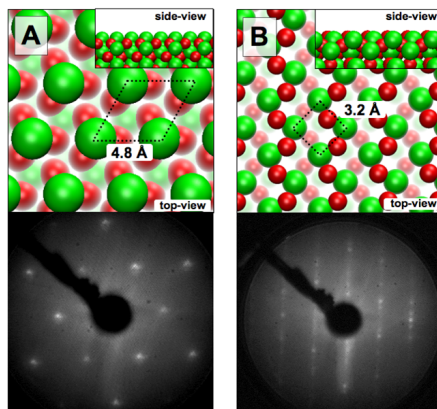


**Figure 6.8.:** (A) top: Top view on the atomic structure of the  $\text{Al}_2\text{O}_3(0001) - \text{Al}$  surface. The small inlet represents a side view. The polar surface only consists of Al-atoms and thus highly reactive Lewis-acid sites. Bottom: LEED pattern recorded at  $60 \text{ eV}$  showing the hexagonal symmetry of the single crystalline surface. (B) top: Top view on the atomic structure of the non-polar  $(1 - 102)$  surface. The small inlet represents a side view, showing the non-polar mixed Al-O termination in the expected ratio. On both surfaces the spatial arrangements in terms of Al-Al (as indicated) as well as Al-O distances significantly differ. Thus simple steric arguments discriminate a stable binding of phosphonic acid on the polar surface as well. Bottom: LEED pattern recorded at  $87.2 \text{ eV}$  showing the cubic symmetry of the single crystalline surface. It can be seen clearly, that the surface additionally exhibits a superstructure into one main direction. The additional spots along the direction suggest either a  $4 \times 1$  or a  $6 \times 1$  reconstruction as it was observed in previous studies as well [174]. An alternate explanation leading to this superstructure pattern might be a non-isotropic Ostwald-ripening as the surface is annealed (see [175]). Due to charging problems it was however not possible to conclusively determine the superstructure. HAS experiments might be a good alternative [174].

## 6. Formation and Stability II

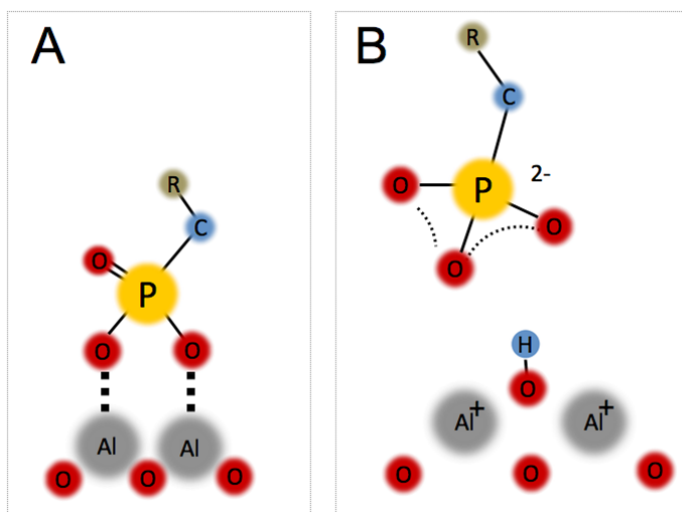


**Figure 6.9.:** (A) Al-Phosphonate binding based on condensation reaction and subsequent coordination (if sterically allowed). In the presented case it is a bidentate binding. (B) Al-Phosphonate binding based on entire deprotonation and subsequent ionic attraction of the respective groups.

phonic acids groups binding on these surfaces. In figure 6.8 the atomic structures of the polar and the non-polar  $\text{Al}_2\text{O}_3$  surface are depicted. For comparison, the  $-\text{PO}(\text{OH})_2$  distances within the phosphonic acid group are around  $2.8 \text{ \AA} - 3 \text{ \AA}$ . It is obvious that the binding distances of the phosphonic acid are not comparable to the Al-Al distances ( $4.8 \text{ \AA}$ ) and/or hydroxide distances on the hydroxide stabilized polar surface. In contrast, on the non-polar (1-102) surface the distances between surface aluminum atoms ( $3.2 \text{ \AA}$ ) is comparable to the distances in the phosphonic acid. This clearly shows that steric arguments discriminate a stable binding based on a condensation reaction of phosphonic acid onto the polar surface as well. For both amorphous surfaces it can arguably be expected that a variety of different types of adsorption sites with unsaturated and dangling bonds are present on the surface, allowing for a stable binding in terms of steric arguments. Finally, the IR-data together with the observed behaviour in aqueous solution indicate a weaker bonding of the ODPAs towards the  $\text{Al}_2\text{O}_3(0001)$  surface, which is based on purely ionic forces between the phosphonate group and a positively charged hydroxylated surface. It can be assumed that the  $\text{PO}_3^{2-}$  adsorbs

## 6. Formation and Stability II

on the protonated hydroxylated  $\text{Al}_2\text{O}_3(0001)$  surface. In contrast, on the other surfaces additionally  $\text{P} = \text{O}$  stretching modes in the absence of  $\text{P-OH}$  vibrations could be detected. It can arguably be expected that an ionic bonding is less stable towards water compared to e.g. an interfacial bonding based on a condensation reaction onto the surface. That means for an  $\text{Al}_2\text{O}_3(1-102)$  and amorphous surface that during the adsorption of the phosphonic acid group the surface hydroxyls are protonated and desorb as water from the surface while the phosphonate group is coordinated to the surface  $\text{Al}^{3+}$  ions. Either a mono-dentate or bi-dentate condensation would be consistent with the IR-data and will be subject to further detailed studies. In figure 6.9 a schematic representation of the different binding situations - ionic binding and coordination binding - as present on the various alumina surfaces is shown.

## 6.5. Conclusions

In summary it was shown that the adsorption of octadecylphosphonic acid on aluminum surfaces is based on different types of interfacial bondings between the surface and the ODPA, which strongly depends on the present surface orientation and thereby local geometries. The stability of the resulting bonding is based on three competing influences, namely interfacial bonding types, adsorption free energies in competition with water and involved adsorption geometries.

The stability of ODPA self-assembly films towards water was investigated on four different model substrates. This comparative study revealed, that ODPA SAMs are stable on (1) native aluminum oxide on a metal support as well as (2) on amorphous aluminum oxide and (3) on  $\text{Al}_2\text{O}_3(1-102)$ . In contrast, ODPA films are not stable in water on (4) the single crystalline  $\text{Al}_2\text{O}_3(0001)$  surfaces and immediately form micelle-like islands at the solid/liquid interface after immersion. This suggests, that the adhesion free energies as well as the local atomic arrangements at the surface play a crucial role for the formation of a stable self-assembly film on aluminum oxide. For the amorphous surfaces also the formation of an insoluble surface salt has to be considered based on the presented results. Concluding, the results suggest an extremely important role of the local atomic structure of the aluminum oxide surface with regards to the formation of stable organophosphonic acid films in competition with water. For technological applications it has to be considered, that polar aluminum oxide surfaces should possibly be avoided if high stability of the binding is desired and vice versa. A comparative approach as presented in this work is expected to be valuable not only for the system at hand but also for other relevant systems. The understanding and discussion of the underlying physical driving forces for adhesion and de-adhesion becomes straightforward, based on this differential approach. Moreover a direct comparison with state-of-the-art *ab initio* based results is possible.

## 6.6. Outlook

In this chapter, ODPA has been successfully adsorbed on four different surfaces of aluminum oxide. Two of them were single crystalline and two them were amorphous. Going this way it was possibly in the end, to

## *6. Formation and Stability II*

understand in a better way which reasons cause the strength of the oxide covered aluminum // ODPa interface. In a next step, the usage of single crystalline model systems now enables the research to make the step to quantum mechanical modeling.

# 7. Formation and Stability of Organophosphonic Acid Monolayers on ZnAl Alloy Coatings

## 7.1. Introduction

The corrosion resistance and the adhesion of organic coatings on oxide covered surfaces is of high importance and is mainly determined by the alloy composition [180], the surface chemistry of the alloy [181] and the composition of the organic coating [182]. To substitute anodizing processes or chromate layers, recently adhesion promoting, ultra-thin films [183] or even monomolecular layers like self-assembled monolayers (SAMs) of organophosphonic acids have been investigated as new advanced interfacial layers for polymer coated aluminum alloys [184].

Aluminum is added to the zinc bath to improve corrosion resistance by either allowing for the formation of a pure zinc overlay for galvanic protection by inhibiting the formation of FeZn phases or by introducing multiphase microstructures in the overlay coating. In each case, the resulting microstructures produce coatings that offer corrosion resistance by a combination of galvanic and barrier protection with corrosion products that in some cases are passive [185].

Hot dip galvanizing (HDG) is the most prominent procedure to coat flat steel with a protective Zn – 0.5% – Al alloy coating. During the galvanizing process, the steel strip moves through hot zinc melt containing small additional amounts of aluminum. The latter process leads to the formation of a very thin FeAl-alloy layer at the interface between steel and the metal alloy coating, thus preventing the formation of brittle FeZn-alloys. The addition of aluminum to the zinc melt also leads to the formation of a native aluminum rich oxyhydroxide passive layer on the surface during

## 7. Formation and Stability III

cooling of the liquid zinc alloy coating. Such Al-surface enrichments have been detected and reported in various papers [186].

Different amounts of aluminum can be added to the Zn bath resulting in ZnAl surface coatings with characteristic microstructure and protective properties.

The ZnAl alloy with 5% aluminum has a complex microstructure [187]. Zn – 5% – Al mainly crystallizes in two different phases, which can be determined by the aluminum amount. For the properties of Zn – 5% – Al it is desirable to maximise the amount of the phase with higher amount of aluminum, allowing the coating to have maximum homogeneity. The unique microstructure of the Zn – 5% – Al is one reason for its increased corrosion resistance. The ZnAl eutectic retains the cathodic protection capability but shows a better intrinsic corrosion resistance due to the development of an adherent aluminum oxide layer over exposed areas [188]. Zn – 55% – Al, is a zinc alloy with even better corrosion resistance which is attributed to the high aluminum content of the coating which allow the formation of comparatively dense, passive layers in corrosive environments.

For the direct binding of organic coatings to ZnAl coated steel, it is a promising approach to combine a ZnAl alloy with increased corrosion resistance and a stable passive film with a strongly bonded dense adhesion promoting monolayer.

Recent studies proved the applicability of phosphonate monolayers as adhesion promoters on aluminum [190] [191] [192]. For aluminum alloy substrates adhesion promoting organophosphonic acid monolayers such as - -aminophosphonic acid were shown to provide excellent adhesion and corrosion resistance of applied epoxy primers and adhesives [190]. Pahnke et al. presented a technique to specifically connect a benzophenone derivative to a hydrocarbon chain on the one hand and adhering it by a phosphonic acid anchor to an aluminum surface on the other hand [193]. Studies focussing on engineering aspects of phosphonate chemistry on aluminum oxides [194] demonstrated that the adsorption velocity of ODPa is strongly depending on the OH-density of the surface which can be directly influenced by plasma modification [195].

Consequently, the focus of this study was to transfer this knowledge to the surface chemistry of ZnAl alloy coatings as the even more widespread technical alloy by studying a selected series of alloy surfaces with distinct different morphologies and atomic structures. The combined study

## 7. Formation and Stability III

of three different ZnAl alloy coatings with various bulk compositions, as well as the adsorption and the desorption of ODPa in competition with water allows a differential understanding of the binding of phosphonic acid molecules towards such complex oxide surfaces.

A profound characterisation of the oxide surface, the adsorption and desorption of ODPa was done by a set of complementary local and integral techniques such as static contact angle measurement data, polarization modulation infrared reflection absorption spectroscopy, X-ray spectroscopy and Time-of-Flight Secondary Ion Mass Spectroscopy.

## 7.2. Experimental

### 7.2.1. Materials

If not indicated otherwise, all chemicals were of p.a. grade (pro analysis) and were used as supplied without any further purification. Three ZnAl coatings with different amounts of aluminum, Zn–0.5%–Al, Zn–5%–Al and Zn–55%–Al were provided by the Dortmunder Oberflächencentrum (TKS-DOC). Pure aluminum samples (Al 99.99 %) were prepared by melting and casting the metal under argon atmosphere. ODPa and abs. Ethanol were provided by Merck, Germany.

### 7.2.2. Sample Preparation

The samples were cut into pieces of  $10 \times 10 \times 1 \text{ mm}$  and ultrasonically cleaned in abs. ethanol for 10 minutes. After rinsing with ethanol the samples were dried in a stream of nitrogen. Cross sections of the alloy coatings are shown in figure 7.1. Pure aluminum samples (Al 99.99 %) were prepared by melting and casting the metal under argon atmosphere. Afterwards, the samples were cut into pieces of  $10 \times 10 \times 3 \text{ mm}$  and the surface was polished with diamond paste of a corn radius of  $1 \mu\text{m}$  and ultrasonically cleaned in abs. ethanol for 10 minutes. After rinsing with ethanol the samples were dried in a stream of nitrogen. The ODPa monolayers on the aluminum oxide surfaces were prepared by solution self-assembly under ambient conditions. Substrates were ultrasonically cleaned in abs. ethanol for 10 minutes before immersing into a  $1 \text{ mM}$  ethanolic solution of ODPa for  $24 \text{ h}$ . After rinsing with ethanol the samples were dried in a stream of nitrogen.

### 7. Formation and Stability III

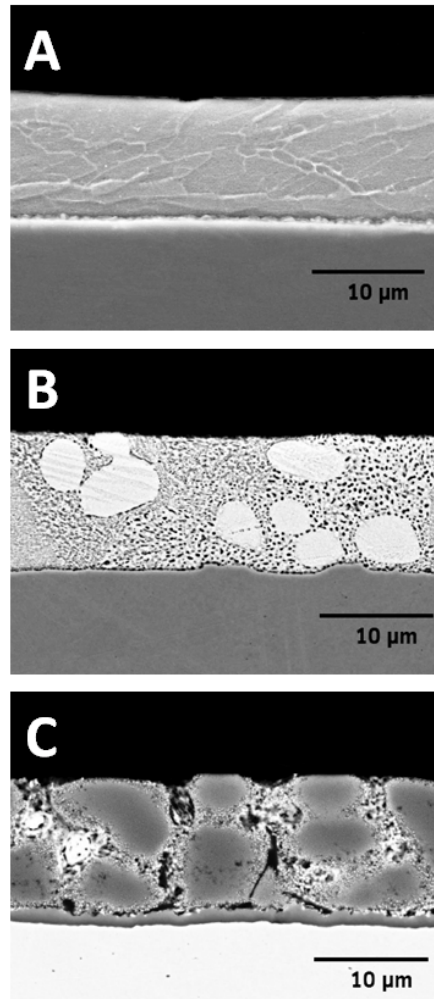


**Figure 7.1.:** (A) Cross-section of Zn – 0.5% – Al with a FeZn-Outburst between the substrate and the coating; starting with the substrate on the bottom, the ZnAl alloy on the top and a thin Fe<sub>2</sub>Al<sub>5</sub> layer in between. (B) Cross-section of Zn – 5% – Al, including light and dark phases in the coating. The dark parts have been identified as delta-phases [199], containing more iron. (C) Cross-section of Zn – 55% – Al. Main features of this coating are a high number of Zn- and Si-dendrites passing through the ZnAl alloy body.

### 7.2.3. Scanning Electron Microscopy

Scanning Electron Spectroscopy images were recorded by means of a NEON 40 FE-SEM (Carl Zeiss SMT AG, Oberkochen, Germany). For Energy Dispersive X-ray (EDX) spectroscopy imaging an UltraDry Silicon Drift X-ray detector from Thermo Scientific was used. Both the imaging and the element analysis were obtained using an acceleration voltage of 5.0 *kV*. The chemical composition analyses of the employed substrates as measured by means of EDX are listed in table 7.1.

**Table 7.1.:** Chemical analysis of the employed alloys by means of EDX

Element [atm %]	Zn-0.5%-Al	Zn-5%-Al	Zn-55%-Al	Aluminum
Al	0.5	5.0	55.0	99.9
Zn	98.5	93.0	40.0	< 0.1
Si	< 0.1	< 0.1	1.6	< 0.1
Fe	0.5	0.2	< 0.1	< 0.1
C	< 0.1	< 0.1	< 0.1	< 0.1
O	0.3	0.3	0.3	< 0.1

### 7.2.4. X-ray Photoelectron Spectroscopy

XPS analyses were performed by means of a Quantum 2000 Scanning ESCA Microprobe (Physical Electronics, USA) spectrometer equipped with a concentric hemispherical analyzer and using an Al  $K_{\alpha}$  X-ray source (15 *KeV*, filament current 20 *mA*). Samples were investigated under ultrahigh vacuum conditions ( $10^{-9} - 10^{-8}$  *mbar*). Spectra were taken at 45° take-off angle with respect to the surface. A sample area of 100  $\mu m \times 100 \mu m$  was analyzed with a pass energy of 46.95 *eV* for survey detailed elemental scans. Sputter depth profiles were recorded with an argon ion sputter gun on an area of 2  $\times$  2 *mm* at an acceleration voltage of 2 *kV*. The spectra obtained were analysed using CASA XPS software, surface sensitivity factors used to determine the atomic concentration were taken from the MultiPak Version 6.0 software (supplied by Physical Electronics). To correct sample charging, the spectra were shifted to set the C-C/C-H components of the C 1s peak at a binding energy of 285 *eV*.

### 7.2.5. Polarization Modulation Infrared Reflection Absorption Spectroscopy

PM-IRRAS measurements were performed by means of a FTIR-spectrometer (Bruker Vertex 70) at a resolution of  $4\text{ cm}^{-1}$  and a reflection angle of  $80^\circ$  relative to the substrate surface normal. For p-polarization of the IR light an aluminum wire grid was used and modulated at  $100\text{ kHz}$  with a ZnSe Photo-Elastic-Modulator (PEM, Bruker PMA-50). Light reflected from the sample was focused with a ZnSe lens onto a cryogenic mercury cadmium telluride (MCT) detector. All presented spectra were recorded from 512 single scans.

### 7.2.6. Static Contact Angle

The static contact angle of water was measured by means of the sessile-drop method using a goniometer (OCA 20, Dataphysics, Germany). Contact angles were measured at five different locations on each sample with DI-water and the average values are reported.

### 7.2.7. Time-of-Flight Secondary Ion Mass Spectroscopy

The analysis was carried out on a gridless reflectron-based ToF-SIMS V (ION-TOF GmbH, Muenster, Germany) equipped with a Bismuth-cluster ion source. All spectra and images were obtained using  $\text{Bi}_3^+$  primary ions at  $25\text{ keV}$  energy in the high current bunched mode with a mass resolution of  $m/\Delta m = 6000$ . The beam diameter was about  $3\text{--}5\ \mu\text{m}$  and all measurements were made under static conditions (primary ion dose  $< F_{PI} = 5 \times 10^{12}\text{ ions cm}^{-2}$ ) on an area of  $400 \times 400\ \mu\text{m}^2$  with  $256^2$  pixel.

## 7.3. Results and Discussion

### 7.3.1. Characterization of the ZnAl Alloy Coating Surfaces

The surface chemistry of the employed alloys was studied by means of complementary spectroscopic and microscopic techniques. Figure 7.2 illustrates the lateral distribution in the outer region of the ZnAl alloy coatings as measured by means of EDX. Zn – 0.5% – Al alloy coating

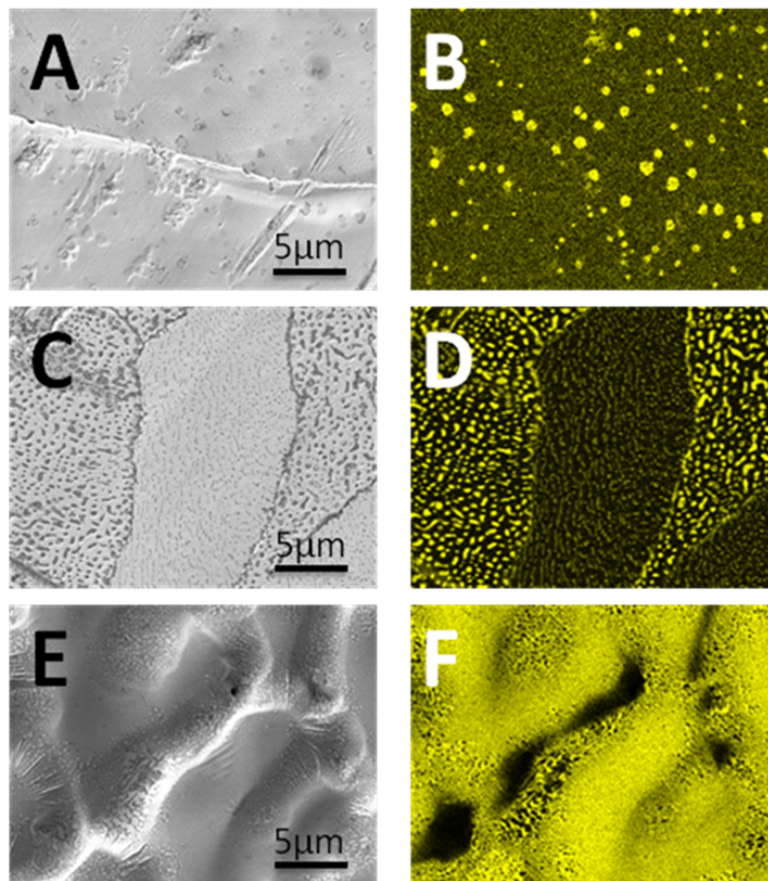


**Figure 7.2.:** ZnAl-alloyed coatings as analyzed by EDX mapping of aluminum. A, C and E show the electron pictures of Zn – 0.5% – Al, Zn – 5% – Al and Zn – 55% – Al, and B, D and F the corresponding Al element mappings.

### 7. Formation and Stability III

(see figure 7.2 A and B shows a homogeneous distribution of its alloying elements. In figure 7.2 C and D the EDX mapping of Zn – 5% – Al shows the existence of two main phases. As observed in figure 7.2 E and F the Zn – 55% – Al coating does not consist of a homogeneous Si-Al-Zn alloy layer but comprises of characteristic spangles with aluminum-rich dendrites, Zn-rich interdendritic regions and a fine dispersion of Si particles [201]. The PM-IRRAS absorption bands within these range represent the vibration modes of AlOOH ( $1100\text{ cm}^{-1}$ ),  $\text{Al}_2\text{O}_3$  ( $950\text{ cm}^{-1}$ ) and OH-adsorbed on  $\text{Al}_2\text{O}_3$  [202] [203]. The exact wavenumbers of these vibration

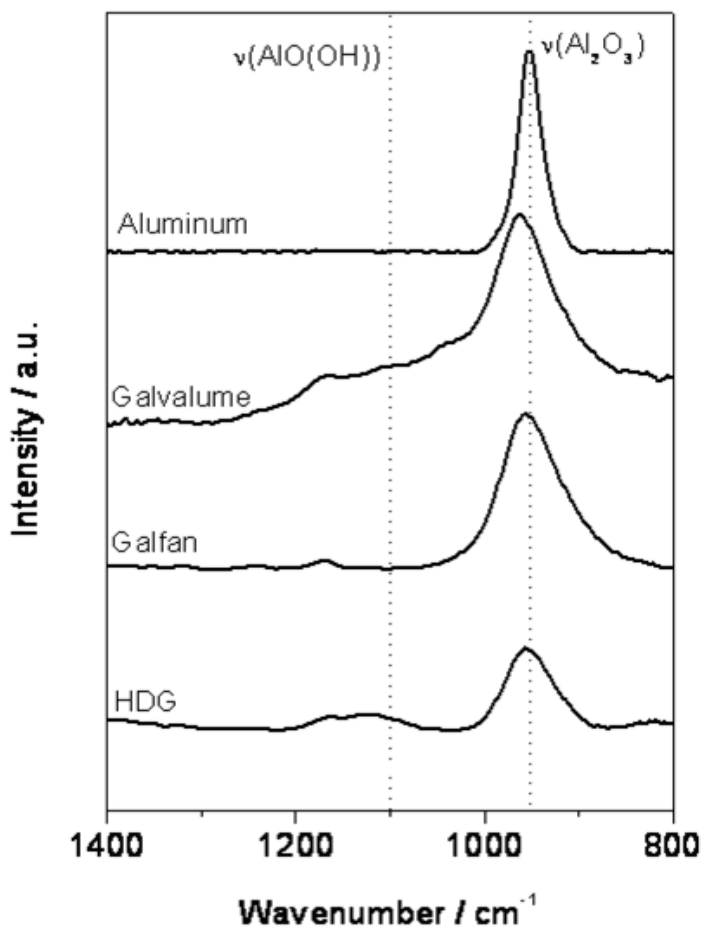


**Figure 7.3.:** PM-IRRAS data of the employed alloy surfaces and an oxide covered aluminum surface.

### 7. Formation and Stability III

modes, shown in figure 7.3, depend on the local chemical environment of the hydroxyls [204].

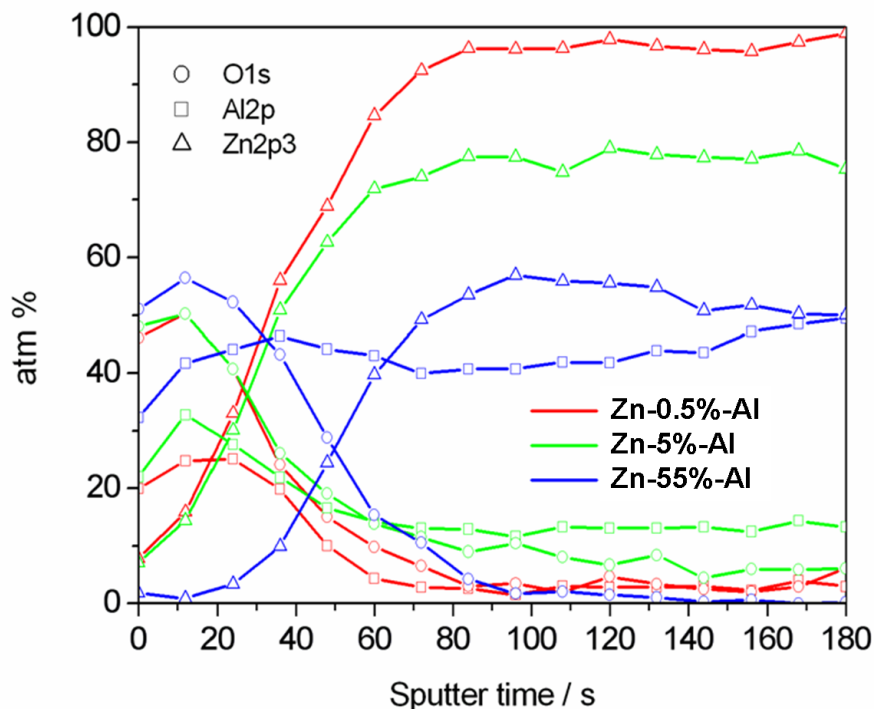


**Figure 7.4.:** XPS sputter profile of Zn–0.5%–Al, Zn–5%–Al and Zn–55%–Al, reference sputter rate:  $R(\text{SiO}_2) = 5.6 \text{ nm}/\text{min}$ .

Complementary to the FTIR-measurements, the alloy surfaces were characterized by means of XPS sputter profiles (see figure 7.4). The surface oxide structure was proven to be essential for the binding of the applied organophosphonic acids [195]. Within the first two nm the Zn–0.5%–Al surface mainly comprises of an aluminum oxihydroxide at a ratio of 2:3 which points at  $\text{Al}_2\text{O}_3$  composition. Within the first 3 nm the surface of Zn–5%–Al mainly comprises of an aluminum oxide at a ratio of 2:3 which points at  $\text{Al}_2\text{O}_3$  composition. The zinc content is nearly negligible and increases at the expense of the oxygen signal after 5 nm. The aluminum amount stays stable. In agreement with literature data it can be expected that ZnAl alloy interphases are formed [205]. The surface oxide structure of Zn–55%–Al mainly consists of an aluminum oxide for the first 4–5 nm which has an  $\text{Al}_2\text{O}_3$  composition. The zinc content is negligible and increases at after 5 nm. The aluminum amount

### 7. Formation and Stability III

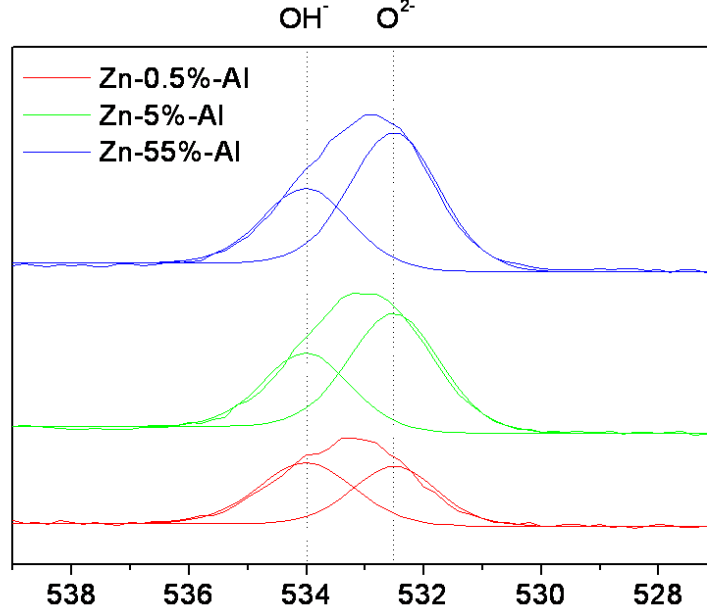


**Figure 7.5.:** XP O1s detail spectra of the employed alloys.

stays stable. The oxide layer thickness  $d$  of the native oxide aluminum film was calculated from the angle-resolved x-ray electron spectroscopy (AR-XPS) intensities  $I_{mo}$  of the Al  $2p_{1_{ox}}$  and  $I_m$  of the Al  $2p_{1_{met}}$  in the following way [206]:

$$d = \lambda_{mo} \cdot \cos\theta \cdot \ln \left[ \left( \frac{D_m \cdot \lambda_m}{D_{mo} \cdot \lambda_{mo}} \right) \cdot \left( \frac{I_{mo}}{I_m} \right) + 1 \right] \quad (7.1)$$

where  $D_{mo}$  ( $6.024 \times 10^{22} \text{ atoms cm}^{-3}$  [206]) and  $D_m$  ( $4.605 \times 10^{22} \text{ atoms cm}^{-3}$  [206]) are the atomic densities of metal atoms in the oxide film and in the underlying metal substrate, respectively,  $\lambda_{mo}$  ( $2.679 \text{ nm}$  [206]) and  $\lambda_m$  ( $2.579 \text{ nm}$  [206]) are the corresponding inelastic mean free paths of the electrons, and is the angle between surface normal and direction of emitted electrons. With the measured values a native oxide layer thickness of  $d = 2.1 \text{ nm}$  was obtained. For estimation of the hydroxyl function density on the surface the O1s-peak was investigated concerning the contribution of oxides and hydroxides (see figure 7.5). Compared to native aluminum oxide surfaces the hydroxide amount appeared to be in the same range for Zn – 0.5% – Al, Zn – 5% – Al and Zn – 55% – Al.

## 7. Formation and Stability III

The  $\text{OH}^-/\text{O}^{2-}$  ratio was estimated to be 1.1 for Zn – 0.5% – Al, 0.8 for Zn – 5% – Al and 0.6 for Zn – 55% – Al, according to the calculation procedure established by [195]. For adhesion promoting molecules with hydrophilic anchor group this improves the formation of a dense SAM [195].

**Table 7.2.:** XPS Analysis of Zn – 0.5% – Al, Zn – 5% – Al and Zn – 55% – Al.

	Zn-0.5%-Al	Zn-5%-Al	Zn-55%-Al
Oxide layer thickness [nm]	2.3	2.8	4.6

### 7.3.2. Adsorption of Octadecylphosphonic Acid Monolayers

Prior to the adsorption of the ODPa, no intensities of phosphor atoms could be observed in the XP spectrum. XP spectra after immersing the ZnAl substrates in a 1 mM ODPa solution for 24 h (followed by an intense rinse with pure EtOH) are shown in figure 7.6. The corresponding peak positions and atomic concentrations based on the curve fitting are listed in table 7.3. The surface composition with a phosphor concentration of about 8% for Zn – 5% – Al and Zn – 55% – Al and about 12% for the Zn – 0.5% – Al shows that the ODPa could be irreversibly adsorbed on all alloy surfaces.

The P2s peak just proves the existence of the adsorbed phosphonate group but does not provide further information on the structure of the adsorbed molecule, as the binding energies of P-CH<sub>3</sub>, P-OCH<sub>3</sub> and P=O surface species are almost similar (ranging from 192.5 to 192.7 eV referring to Davies and Newton [208]).

In figure 7.7 analysis of the employed alloys before and after the adsorption of ODPa on the surface by means of ToF-SIMS are shown. The ToF-SIMS imaging shows that in accordance with the observed Al<sub>2</sub>O<sub>3</sub>-passive film covered surface of the Zn-alloys with higher aluminum contents also the ODPa coverage is almost perfect. In the case of the Zn – 0.5% – Al alloy, variations in the surface composition were observed. However, the ToF-SIMS analysis only provides information on the outermost atomic surface layer and does not reflect the thickness of the film, the orientation of the monolayer or the state of interfacial binding.

## 7. Formation and Stability III

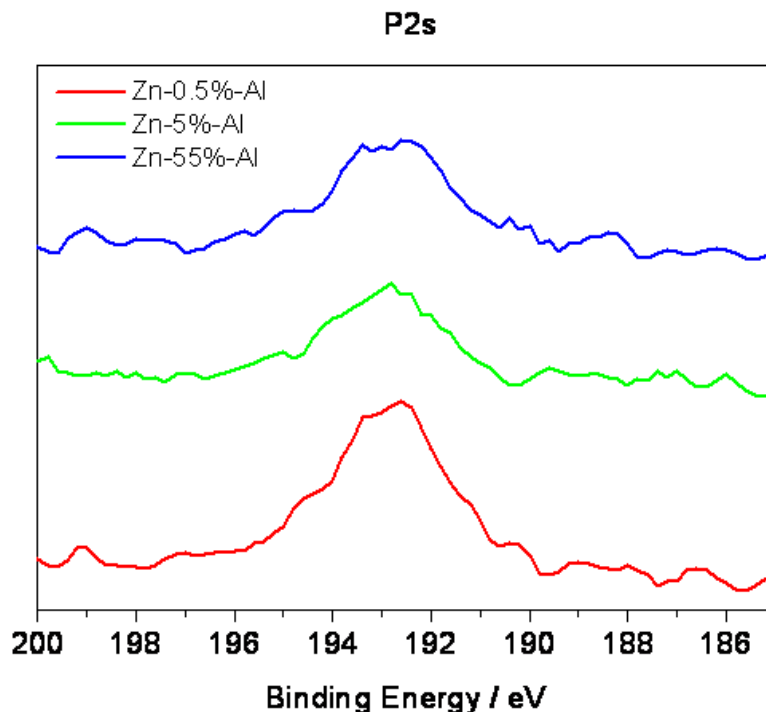


**Figure 7.6.:** XP P2s detail spectra of the employed alloys after adsorption of ODPA.

The adsorption of the phosphonate adhesion promoter on the ZnAl alloy surfaces occurs via acid base interaction. The state of binding of the self-assembled ODPA monomers could be characterized ex-situ by means of PM-IRRAS. The interaction can be determined by studying the shift of peaks assigned to P=O and P-O-H in the infrared spectrum. Changes in these values are indicative of changes in the bond strength and therefore conformation of the head group [211]. A clear correlation between the packing density of the adsorbed ODPA molecules and the structure and thickness of the passive films on the alloy substrates has been observed based on the PM-IRRAS studies. In figure 7.8 the PM-IRRAS spectra of the ODPA adsorbed on the employed ZnAl alloy surfaces are shown. The presence of the  $\text{PO}_3^{2-}$  stretch mode at  $1089\text{ cm}^{-1}$  in the spectrum is indicative of the deprotonation of the phosphonic acid group [211]. A remarkable difference between Zn – 0.5% – Al on the one hand, and Zn – 5% – Al and Zn – 55% – Al on the other hand is that the intensity of the ODPA spectrum is by a factor of two higher for Zn – 0.5% – Al

### 7. Formation and Stability III

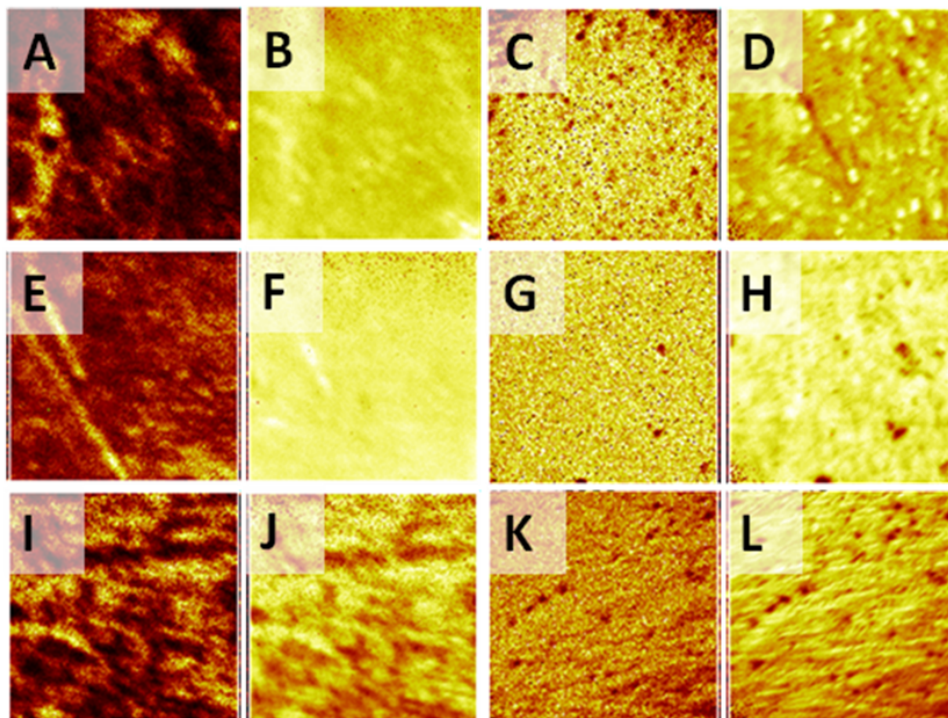


**Figure 7.7.:**  $100 \times 100 \mu\text{m}$  ToF-SIMS mappings of Al and  $\text{PO}_3$  after the adsorption of ODPA on the alloy surfaces. (A) to (D) show the results for the Zn-0.5%-Al surface. The surface composition is inhomogeneous including dark areas with less concentration and even holes. (E) to (H) show the Zn-5%-Al surface after the monolayer adsorption. Apart from very few defects, an ODPA SAM was observed. (I) to (L) show surface chemistry image after the adsorption of ODPA on Zn-55%-Al. Also here only few defects were observed and the surface was covered nearly completely by the monolayer.

as substrate both for the CH stretch-vibrations and the  $\text{PO}_3^{2-}$  stretch-vibrations. Moreover, the CH deformation mode at  $1450 \text{ cm}^{-1}$  only appears for the Zn-0.5%-Al substrate.

To get information on the mean orientation of the adsorbed ODPA molecules a simple calculation was performed according to the method

## 7. Formation and Stability III

**Table 7.3.:** Chemical analysis of the employed alloys by means of XPS

Element [atm %]	Zn – 0.5% – Al	Zn – 5% – Al	Zn – 55% – Al
C1s	65.2	48.4	36.5
O1s	15.7	25.2	25.8
P2s	12.3	7.2	8.8
Zn2p3	0.4	0.3	-
Al2p	6.3	18.7	28.8

established by Allara [210]. The ratio between the peak intensity of the asymmetric stretching vibrations of the methylene and the methyl group

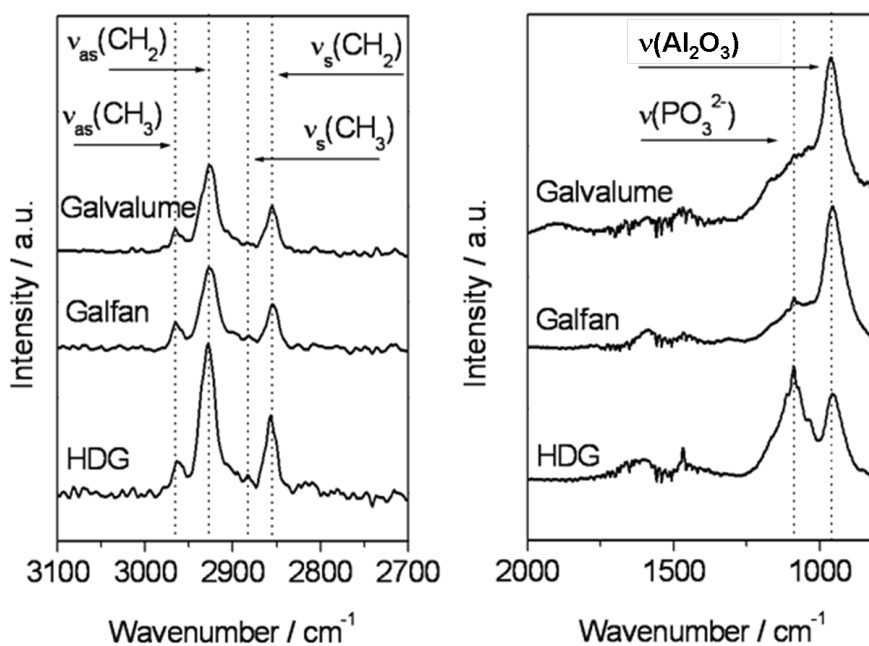


**Figure 7.8.:** PM-IRRAS spectra of ODPA adsorbed on the employed ZnAl alloy surfaces.

## 7. Formation and Stability III

correlate with the mean inclination angle according to [210]

$$\frac{I_{CH_2}}{I_{CH_3}} = \frac{n \cdot 2 \cdot \cos \cdot (90^\circ - \alpha)^2}{3 \cdot \cos \cdot (35^\circ - \alpha)^2} \quad (7.2)$$

where  $I_i$  is the intensity of the according CH asymmetric stretching vibration bands,  $n$  accords to the  $CH_2$  chain length and is the angle between the alkyl chain axis and the surface normal. After 24 *h* of adsorption the alkyl chain has reached an angle of  $33^\circ$  with respect to the surface normal on Zn – 5% – Al and Zn – 55% – Al, which is close to the azimuth angle of ODPA on oxide covered aluminum in the range of  $30^\circ$ . These angles prove the self-assembly process and indicate a dense packing of the alkyl chains interacting with each other via van der Waals forces.

On Zn – 0.5% – Al as substrate the azimuth angle is larger than  $40^\circ$ . In conjunction with the higher observed film thickness this indicates that ODPA does not build a SAM on the oxide covered Zn – 0.5% – Al surface but precipitation layers are formed due to the dissolution of Zn-ions during the adsorption of the phosphonic acid.

The roughness values of the ODPA covered substrates as measured by means AFM is are given in table 7.4.

**Table 7.4.:** AFM surface analysis of Zn – 0.5% – Al, Zn – 5% – Al and Zn – 55% – Al.

	Zn-0.5%-Al	Zn-5%-Al	Zn-55%-Al
Roughness RMS [nm]	532.0	66.0	119.0

### 7.3.3. Stability of Octadecylphosphonic Acid Monolayers

The stability of the adsorbed ODPA films was studied in aqueous solutions. Water contact angle measurements were performed to study the hydrophobicity of the respective surfaces before and after the immersion in water for defined periods of time. Such water contact angles are a simple and reliable source of information concerning the state of ordering of adsorbed long chain aliphatic monolayers with non-polar terminating group such as  $CH_3$ . The ODPA film covered surfaces were discontinuously immersed in DI water for 10 *min* per immersion step. The static

## 7. Formation and Stability III

contact angles of water were measured and plotted as a function of immersion cycles for all studied surfaces. The resulting tendencies are shown in figure 7.9.

It was observed that the static contact angle of water taken of the precipitation layers formed on Zn-0.5% - Al was decreasing significantly, finally resulting in a contact angle of  $60^\circ$  as measured for a clean substrate. In contrast, contact angle measurements obtained SAM covered surfaces of the native grown aluminum, the Zn - 5% - Al and the Zn - 55% - Al keep stable over several immersion cycles. It was not even possible to decrease the contact angle due to immersion into water and simultaneous exposure to ultrasonic acoustic irradiation.

These results clearly reveal the impact of heterogeneity of the surface structure on the molecular desorption of ODPa in competition with water. For amorphous alumina films it can arguably be expected that a variety of different types of adsorption sites with unsaturated and/or dangling bonds are present on the surface due to the amorphous character of the atomic structure at the surface. This structural character consequently leads to strong binding of phosphonic acid towards the surface.

### 7.4. Conclusions

For the ZnAl alloy coatings Zn - 0.5% - Al (HDG), Zn - 5% - Al (Galfan) and Zn - 55% - Al (Galvalume) it was shown that all investigated surface properties are based on the bulk composition of the coating. We found that the ratio of zinc to aluminum in the coating directly influences the formation and composition of the passive films on the surface and thereby the surface chemistry.

The adsorption of ODPa on oxide covered surfaces has been investigated on Zn - 0.5% - Al, Zn - 5% - Al and Zn - 55% - Al. While the passive film of Zn - 5% - Al and Zn - 55% - Al consists of closed oxide covered aluminum, the one on Zn - 0.5% - Al was shown be more mixed oxide containing also parts of ZnO. The adsorption of ODPa on Zn - 0.5% - Al surfaces thus leads to precipitation layers.

The stability of ODPa adsorbed on the ZnAl alloy coatings in competition with water confirmed the idea of very different surface chemistries of the aluminum oxide covered surfaces and the mixed oxide covered surfaces. While the SAMs build up dense packages on the aluminum oxide

### 7. Formation and Stability III

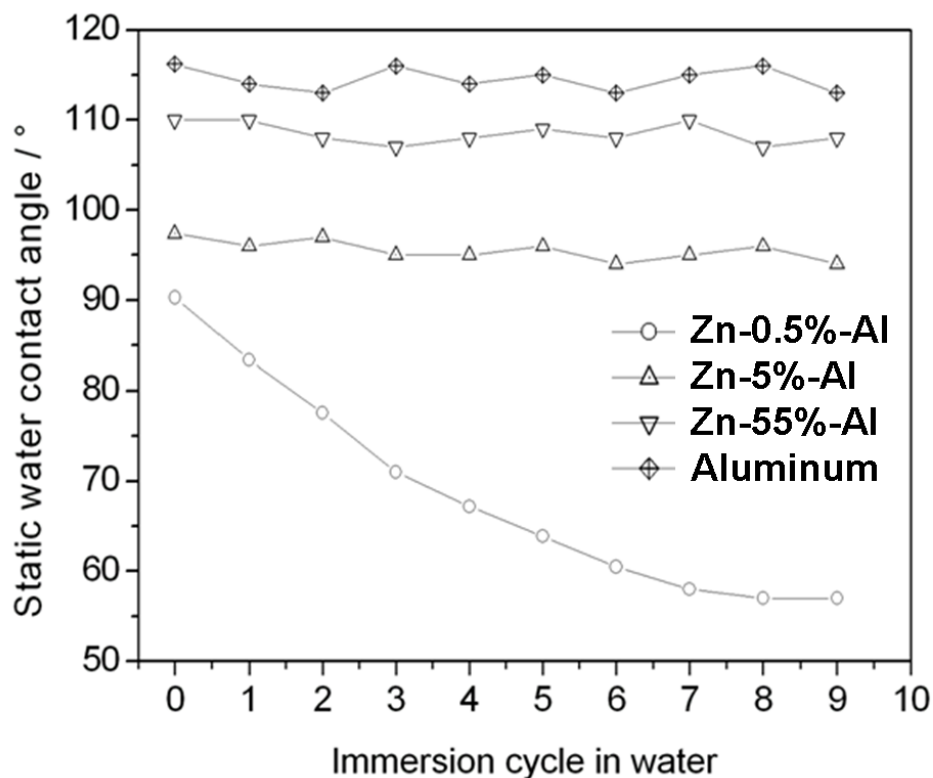


**Figure 7.9.:** Mean values of static contact angle of water on ODPA covered Zn – 0.5% – Al, Zn – 5% – Al, Zn – 55% – Al and native oxide covered aluminum.

and resist the water, the precipitation layers on the mixed oxide surfaces do not give any prevention in the competition with water.

Concluding, the results suggest an extremely important role of the alloy composition, the surface chemistry of the alloy and the composition of the organic coating with regards to the formation of stable phosphonic acid films.

In relation to the corrosion it is expected that densely packed films improve the corrosion protection, as they inhibit for electrolytes to enter the metal surface effectively.

To summarize, for Zn – 5% – Al and Zn – 55% – Al, the spectra confirm the model of the acid-base interactions between phosphonic acids and oxide covered aluminum surfaces due to the shift of the P=O peak

## 7. Formation and Stability III

and the disappearance of the peaks attributed to P-O-H stretching. The driving force is the formation of a self-assembled monolayer.

In contrast, the mixed oxide covered surface, like Zn – 0.5% – Al, does not form a SAM but a precipitation layer. During this process,  $\text{Zn}^{2+}$  is etched out of the surface and coordinated by the ODPAs. Due to the rising concentration close to the oxide/liquid interface, the ODPAs/Zn-salt precipitates. The layer formation stops when the surface salt has built up a dense layer and no more Zn-ions are solved.

### 7.5. Outlook

The investigations of industrial systems HDG, Galfan and Galvalum has been more difficult than the research on single crystalline model systems and the reproducibility of results came out to be much lower. Nevertheless, the direct cooperation with industry partners is necessary. For the fields of ZnAl alloys and phosphonic acids it has been shown, that phosphonic acid could be able to serve as adhesion promoter. Next steps in the fundamental and industrial research can be to find production mechanism including already the organic coating, and get an real overview about producing costs.

# 8. Water Adsorption on the $\alpha$ -Al<sub>2</sub>O<sub>3</sub>(0001) Surface

## 8.1. Introduction

The interaction of water with solid surfaces is fundamental to research in various fields ranging from atmospheric chemistry to corrosion and heterogeneous catalysis. Despite substantial research efforts, however, precise information on the water geometry at the atomic level often seems elusive, for the ubiquitous liquid phase [212, 213] as well as for many cases of substrate-supported thin water films and clusters prepared in the laboratory [214, 215, 216, 217, 218, 219, 220].

The interaction of water with aluminum oxide has found interest because of the extensive use of this material, e.g., as a catalyst as well as a catalyst support, and by its role in environmental chemistry. Moreover, the well defined Al-terminated  $\alpha$ -Al<sub>2</sub>O<sub>3</sub>(0001) surface is a widely studied model for water interaction with metal oxide surfaces. Experimentally, most studies propose water dissociation on the Al-terminated  $\alpha$ -Al<sub>2</sub>O<sub>3</sub>(0001) surface. This was concluded from high-resolution electron-energy-loss spectroscopy (HREELS) studies [221] as well as thermal desorption experiments (TDS) [222, 223]. X-ray photoemission experiments [224] were interpreted to indicate water dissociation in particular at surface defect sites. Early ultraviolet photoelectron spectra, on the other hand, seem to indicate molecular adsorption of water at room temperature [225]. Also the mobility of the adsorbed molecules on the  $\alpha$ -Al<sub>2</sub>O<sub>3</sub>(0001) surface seems to be a somewhat open question. In Ref. [223] a low mobility of the hydroxyl groups at the surface was stated, in contrast to the interpretation of dynamic scanning force microscopy images of the water exposed  $\alpha$ -Al<sub>2</sub>O<sub>3</sub>(0001) surface [226]. Theoretically, most *ab initio* studies agree on the stability of the dissociative vs the molecular adsorption [227, 228, 229] while one cluster study [230] found little difference between the energies of molecular and dissociative adsorp-

## 8. Water Adsorption on the $\alpha$ - $\text{Al}_2\text{O}_3(0001)$ Surface

tion of water. A recent density functional theory (DFT) study compares the energetics of a wide range of adsorption geometries for various coverages [231]. However, this comparison does not include the possibility of a dissociative adsorption as concluded from many experimental studies. Also, the change of the surface composition upon adsorption is not considered in these studies, despite early indications for the high stability of the oxygen-terminated surface in the presence of water [234, 233, 232]. This is confirmed in a very recent study by Ranea *et al.* [235] that finds the fully hydroxylated surface to be the thermodynamic ground state in the presence of water, but concluded that the actual surface composition will depend strongly on the sample history.

Here we present a comprehensive comparison of the adsorption energetics of both molecularly and dissociatively adsorbed water for various coverages based on density functional theory. Potential energy surfaces for surface adsorbed water molecules, hydrogen and hydroxyl groups are presented to address the controversial issue of surface mobility. In addition, the adsorption energetics is also addressed experimentally, by temperature programmed desorption (TPD) spectroscopy.

### 8.2. Theory

The calculations are performed using DFT within the generalized gradient approach (GGA) as implemented in the Vienna *Ab initio* Simulation Package (VASP) [236]. The electron-ion interaction is described by the projector-augmented wave scheme [237]. The electronic wave functions are expanded into plane waves up to a kinetic energy of 360 eV. The surface is modeled by periodically repeated slabs. Each supercell consists of 18 atomic layers within  $(2 \times 2)$  periodicity plus the adsorbed water and a vacuum region equivalent to 18 Å. The 15 uppermost layers as well as the adsorbate degrees of freedom are allowed to relax until the forces on the atoms are below 20 meV/Å. The Brillouin zone integration is performed using  $2 \times 2 \times 1$  Monkhorst-Pack meshes. We use the PW91 functional [238] to describe the electron exchange and correlation energy within the GGA. It describes the hydrogen bonds in solid water (ice Ih) in good agreement with experiment [239, 240].

### 8.3. Experimental

Experimentally, after cleaning with concentrated phosphoric acid (85%), rinsing with water and drying in a stream of nitrogen, the sapphire crystal was annealed in air in a high purity furnace at about 1600 K for 24 hours. The annealing produced a surface with large terraces ( $> 1\mu\text{m}$ ) as evidenced by atomic force microscopy (AFM) and low energy electron diffraction (LEED), cf. Fig. 8.1. The ultra high vacuum (UHV) system consists of a pumping system and the vacuum vessel. All parts of the vacuum vessel are made of high-grade steel. Besides the pressure gauge a manipulator onto which a sample can be mounted for studies of its surface properties and a quadrupole mass spectrometer (QMS) is attached to the chamber. Vacuum was maintained by two turbo molecular pumps backed by a rotary oil pump. The sample manipulator is based on a rotatable rod that can be moved horizontally and screws allow the accurate positioning of the sample. The manipulator also has electrical feedthroughs with ceramic insulation for connecting the sample to a power supply for resistive heating and two thermocouple wires to a temperature controller. Temperatures of up to approximately 1000 K can thus be obtained at the single crystal sample. The heating power is regulated by a temperature controller that reads the voltage of a thermocouple welded to the side of the sample. The different surface coverages of water were achieved just before transferring the sample to UHV. One sapphire sample was taken fresh from the furnace (movement time through ambient air till UHV transfer about 2 min). Second sample was put into liquid water for one minute and the last one was activated in low temperature water plasma for the same time. The TPD experiment were driven with a heating rate  $\beta$  of  $1\text{ Ks}^{-1}$ .

### 8.4. Results and Discussion

While the corundum structure of bulk  $\alpha$ - $\text{Al}_2\text{O}_3$  has a rhombohedral symmetry, the atomic positions are usually given in terms of a hexagonal unit cell. The Al-terminated  $\alpha$ - $\text{Al}_2\text{O}_3(0001)$  surface has  $p3$  symmetry, i.e., a threefold rotational axis through the Al-ions and no mirror planes. In good agreement with previous studies [241, 242], we find upon structural relaxation of the clean surface that the outermost Al-ions move toward the bulk, ending up almost in plane with the O-atoms, cf. Fig. 8.2.

## 8. Water Adsorption on the $\alpha\text{-Al}_2\text{O}_3(0001)$ Surface

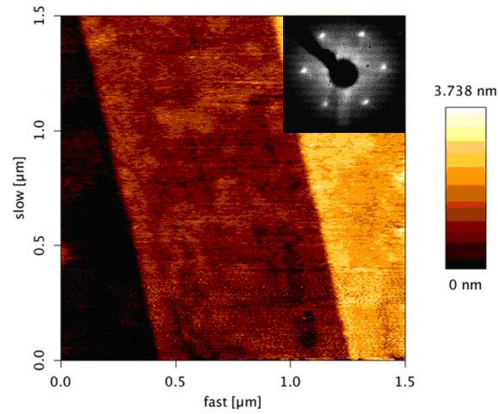


**Figure 8.1.:** AFM topography of the single crystalline  $\alpha\text{-Al}_2\text{O}_3(0001)$  surface. Step heights are typically about 1 nm. The inset shows LEED pattern recorded at 60 eV representing the hexagonal symmetry of the surface.

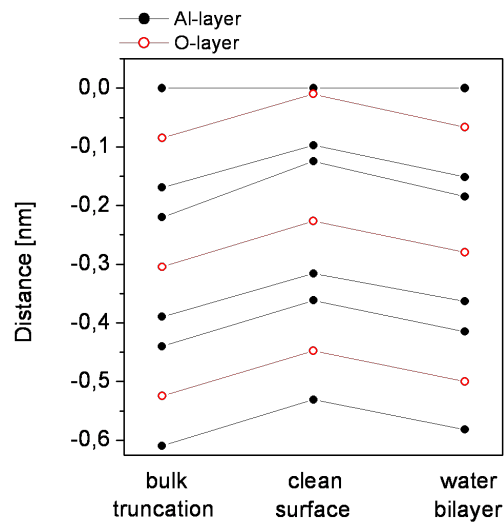


**Figure 8.2.:** Schematic side view of the bulk and slab state indicating the vertical surface relaxation of Al (solid) and O (dashed) layers. The zero line corresponds to the outmost surface atom.

## 8. Water Adsorption on the $\alpha$ - $\text{Al}_2\text{O}_3(0001)$ Surface

We start the adsorption study by determining the potential energy surfaces (PES) for (a) single water monomers, (b) hydrogens in the presence of a surface adsorbed hydroxyl group and (c) hydroxyl groups in the presence of a surface adsorbed hydrogen on the clean, Al-terminated  $\alpha$ - $\text{Al}_2\text{O}_3(0001)$  surface, respectively. Apart from the lateral position of one adsorbate atom, the structural degrees of freedom of both substrate and adsorbate were fully relaxed in these calculations. The calculated data are shown in Fig. 8.3. In order to account for the fact that energy barriers hinder the free rotation of surface adsorbed water molecules, the minimum energy geometry for every PES sampling point was obtained by probing different molecular starting orientations. As can be seen in Fig. 8.3, the energy landscape experienced by molecularly adsorbed water monomers as well as dissociated hydrogens or hydroxyl groups is rather corrugated, with maximum energy differences/minimum diffusion energy barriers of 0.54/0.48 eV, 1.54/0.66 eV, and 1.54/1.31 eV. These data clearly support the view of a rather low mobility, in particular of the hydroxyl groups, at the surface [223]. The diffusion barriers for water monomers are somewhat lower, but still substantial.

Starting, from the low energy adsorption configuration of single water monomers on the  $(2\times 2)$  surface unit cell, the water coverage was systematically increased to eight molecules. The corresponding lowest-energy structures for the respective coverage on the Al-terminated surface are denoted by  $\text{AT}n$  in the following, where  $n$  corresponds to the number of molecules per  $(2\times 2)$  surface unit cell. Among others, the adsorption configurations from Ref. [231] as well as (partially) dissociated adsorption models were probed. In addition, we calculate the energetics of the fully hydroxylated (gibbsite-like) surface that can be understood as the triple hydrogenation of the non-stoichiometric O-terminated  $\alpha$ - $\text{Al}_2\text{O}_3(0001)$  surface [243, 235]. It is denoted as FH in the following. Also the adsorption of an  $n$  additional water monomers on top of this structure, denoted as  $\text{FH}n$ , is considered.

In order to compare adsorption models with different water coverages, the thermodynamic grandcanonical potential

$$\Omega(\mu_i) = F_{surf}(n_i) - \sum_i n_i \mu_i \approx E_{surf}(n_i) - \sum_i n_i \mu_i \quad (8.1)$$

needs to be calculated [244], where  $F_{surf}(n_i)$  is the surface free energy which we approximate by the total surface energy  $E_{surf}(n_i)$  at zero tem-

## 8. Water Adsorption on the $\alpha\text{-Al}_2\text{O}_3(0001)$ Surface

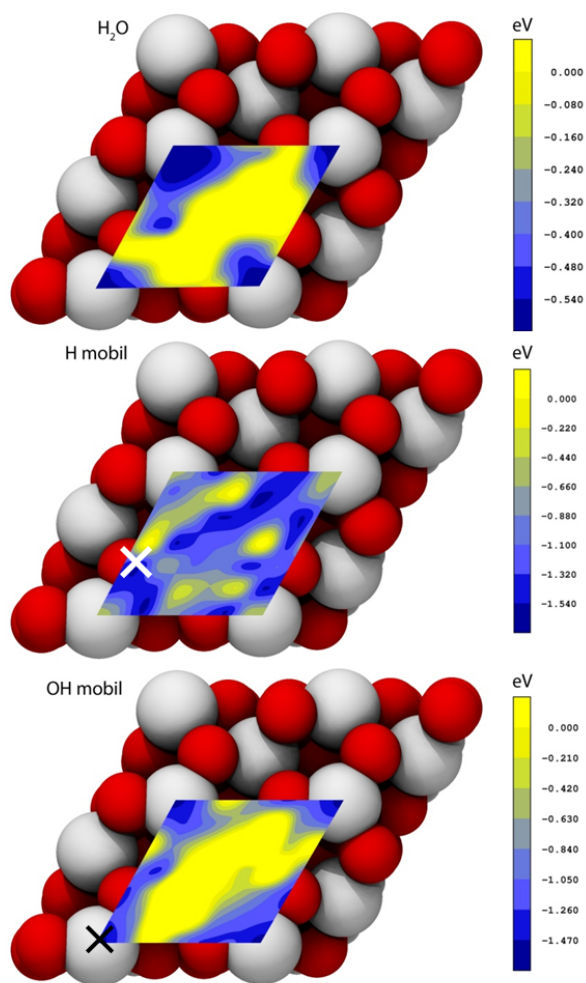


**Figure 8.3.:** Potential energy surfaces for (a) single water monomers, (b) hydrogens in the presence of OH groups (black cross), and (c) hydroxyl groups in the presence of H (white cross) on the  $\alpha\text{-Al}_2\text{O}_3(0001)$  surface, respectively.

## 8. Water Adsorption on the $\alpha$ - $\text{Al}_2\text{O}_3(0001)$ Surface

perature, assuming similar entropy contributions for different adsorption configurations. The number of adsorbate molecules is represented by  $n_i$ . Figure 8.4 shows the resulting phase diagram in the dependence of the water chemical potential. Two important values of  $\mu^{\text{H}_2\text{O}}$  are indicated. Extreme water-rich conditions are marked by the vertical line at  $\Delta\mu = 0$ . This value corresponds to a  $\text{Al}_2\text{O}_3$  surface in equilibrium with bulk water, approximated here by calculations for ice Ih [240]. Lower values of  $\Delta\mu$  indicate an increasingly dry environment. The zero temperature calculation for gas-phase water molecules is indicated. At finite temperatures, entropy corrections will lower the respective value of  $\mu$  for the surface in equilibrium with a reservoir of water vapor [245] and also slightly affect the relative stability of different surface phases, see, e.g. Refs. [243, 246]. The inclusion of the fully hydroxylated surfaces [235] in the phase diagram seemingly introduces an additional degree of freedom: The stability of these structures will depend on the chemical potential of the surface liberated Al. It may, for example diffuse into the bulk material or desorb as  $\text{Al}(\text{OH})_3$ , while the remaining protons of the water molecules adsorb on the three O subsurface atoms that originally bonded to the now released Al atom. From a thermodynamic perspective, the Al atoms are in any case in equilibrium with bulk  $\text{Al}_2\text{O}_3$ , even if the particle exchange with the bulk material is kinetically hindered and may be slow.

As expected, for low values of the water chemical potential the clean  $\text{Al}_2\text{O}_3$  surface is stable. As the environment gets more and more humid, a variety of water-adsorbed surface structures may be observed. Considering first the adsorption on the Al-terminated surface, the adsorption models AT1 and AT3, are stable for a very small window of preparation conditions, while the full monolayer (AT4) and the bilayer (AT8) structure are stable for a relatively wide range of water-rich and extreme water-rich conditions. This sequence, however, does not correspond to the thermodynamic ground state of the surface that is characterized by the fully hydroxylated surface. The stability of the fully hydroxylated surfaces reflects the strength of the H-OAl bond and is consistent with the negative enthalpy of formation of the  $\alpha\text{-Al}_2\text{O}_3 + 3 \text{H}_2\text{O} \leftrightarrow 2\text{Al}(\text{OH})_3$  reaction at ambient conditions. As pointed out already in Ref. [235], however, the formation of the FH structures is expected to be kinetically hindered and the actual surface phase will strongly depend on the sample history.

Low coordination of surface Al-ions on clean  $\alpha\text{-Al}_2\text{O}_3(0001)$  makes

8. Water Adsorption on the  $\alpha\text{-Al}_2\text{O}_3(0001)$  Surface

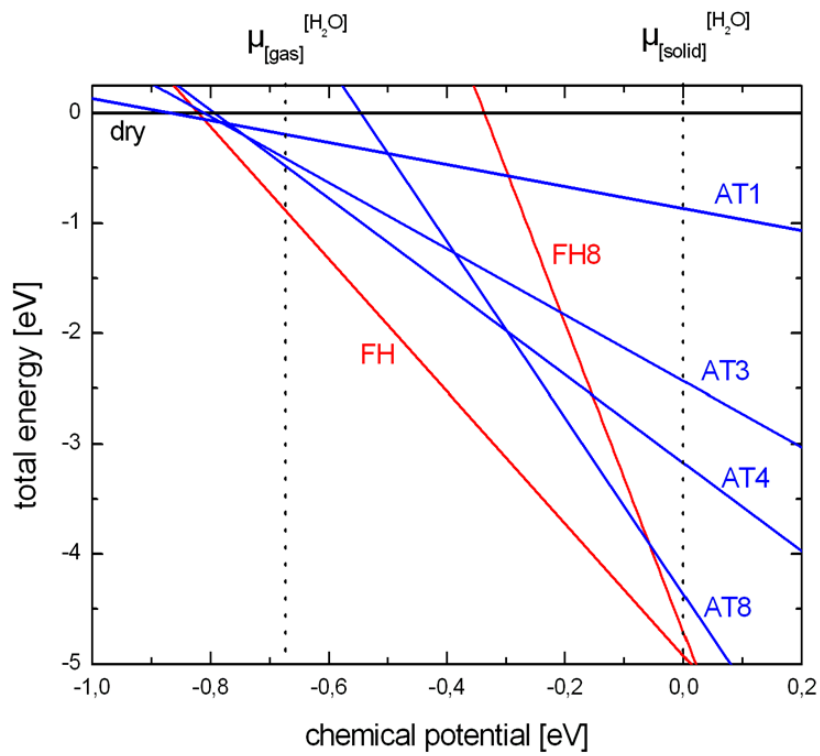


**Figure 8.4.:** Calculated phase diagram of the  $\alpha\text{-Al}_2\text{O}_3(0001)$  surface in dependence on the water chemical potential  $\Delta\mu$  given with respect ice Ih.

## 8. Water Adsorption on the $\alpha$ -Al<sub>2</sub>O<sub>3</sub>(0001) Surface

these sites strong lewis acids, i.e. electron acceptors, which readily adsorb molecules like H<sub>2</sub>O, that can add electron-density. The dissociative adsorption is primarily heterolytic in nature. Adsorbed H<sub>2</sub>O dissociating can be viewed as splitting into H<sup>+</sup> and OH<sup>-</sup>, with the proton transferred to a nearby surface site in a 1-4 mechanism [227]. For all coverages, adsorption of H<sub>2</sub>O significantly disrupts the clean  $\alpha$ -Al<sub>2</sub>O<sub>3</sub>(0001) surface geometry. The adsorption pulls the surface Al-ion out of its relaxed surface position and elongates its three bonds to neighboring oxygen ions. Bonds between this Al-ion and second-layer O-ions are significantly longer, and they are elongated even beyond the bulk values, cf. Fig. 8.2. That a relatively isolated H<sub>2</sub>O molecule prefers to adsorb dissociatively on  $\alpha$ -Al<sub>2</sub>O<sub>3</sub>(0001), even in the absence of defects, differs from the behavior predicted in an earlier study of H<sub>2</sub>O on MgO(100) [247]. In that case, dissociative adsorption was favored in the vicinity of a step, but molecular adsorption was more stable on the ideal surface.

The most relevant structures from the surface phase diagram are shown in Figs. 8.5 and 8.6. For low water coverages on Al-terminated surfaces, single dissociated molecules (AT1) are stable. The ground-state geometry calculated here corresponds to the 1-2 geometry discussed in Ref. [227]. It is energetically nearly degenerate with the 1-4 structure. The latter structure, however, requires a substantially lower activation energy [227]. Interestingly, if all surface Al atoms are occupied by hydroxyl groups, additional water molecules do not dissociate but form hydrogen bonds with the pre-adsorbed H and OH groups, see Fig. 8.6. Hexagons form (AT8) that are somewhat reminiscent of the water hexagons formed on many metal surfaces [217, 220]. In contrast to the latter, however, the hexagon structures formed on  $\alpha$ -Al<sub>2</sub>O<sub>3</sub>(0001) consist of alternating dissociated and intact molecules, which might explain some of the experimental ambiguities discussed above. It is interesting to note that a recent theoretical study by Scheffler and co-workers found similarly a crossover to a mixed molecular and dissociative adsorption mode with increasing water chemical potential for water adsorption on Fe<sub>3</sub>O<sub>4</sub>(0001) [248]. Also shown in 8.5 and 8.6 are the fully hydroxylated surface (FH) and the adsorption of an additional water bilayer on top (FH8).

Fig. 8.7 shows the adsorption energy per molecule for the adsorption structures AT1 - AT8 calculated as

$$E_{ads} = \frac{(E_n - E_0) - n \times E_{H_2O}}{n}. \quad (8.2)$$

8. Water Adsorption on the  $\alpha\text{-Al}_2\text{O}_3(0001)$  Surface

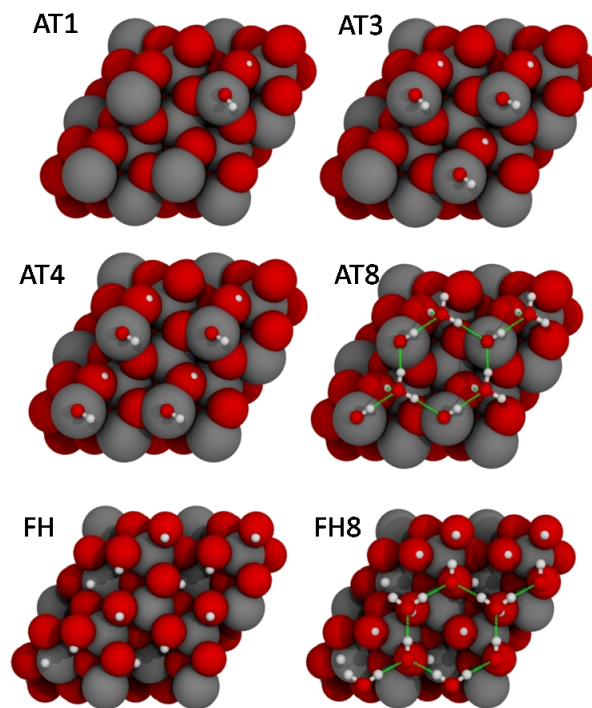


**Figure 8.5.:** Schematic top view of relevant adsorption structures.

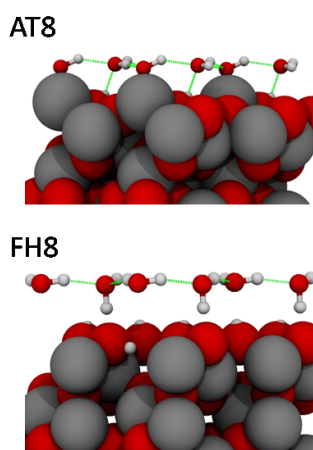


**Figure 8.6.:** Schematic side view of a water bilayer adsorbed on the Al-terminated (AT8) or fully hydroxylated (FH8) surface.

## 8. Water Adsorption on the $\alpha$ - $\text{Al}_2\text{O}_3(0001)$ Surface

We find the relative adsorption energy to vary only moderately between the different adsorption geometries. This indicates that the surface-molecule interaction is dominant over the molecule-molecule interaction. A closer look at the adsorption energies shows two additional trends: A slight decrease of the adsorption energy with increasing coverage of dissociated molecules is followed by a somewhat more pronounced decrease as soon as the molecularly adsorption starts for coverages above one water molecule per primitive surface unit cell (AT4). Overall we find a variation between about 1.5 and 1.2 eV for the adsorption energy. The lower limit agrees well with the calculations of Ranea *et al.* [231], who considered exclusively molecularly adsorbed water. Also the energy difference between molecularly and dissociatively adsorbed water is close to the earlier calculations which state about 0.43 eV for the low-coverage regime [227].

Also shown in Fig. 8.7 are the differential binding energies  $E_{TDS}$  calculated as

$$E_{TDS} = E_n - E_{n-1} - E_{\text{H}_2\text{O}}. \quad (8.3)$$

Here we calculated a somewhat larger spread between 0.8 and 1.6 eV for adsorption on the Al-terminated surface. This spread gets even larger if the energy is considered to either extract one water monomer from the FH structure (about 2.5 eV) or to remove water monomers adsorbed on top of the fully hydroxylated surface (about 0.6 eV), see square symbols in Fig. 8.7. In case of the fully hydroxylated surface the trend that water adsorption in excess of the monolayer structures leads to a decrease of the adsorption energy is even more pronounced than for the metal-terminated surface, see Ref. [246].

The adsorption energetics was also studied using TPD measurements of differently water-treated  $\alpha$ - $\text{Al}_2\text{O}_3(0001)$  surfaces, see Fig. 8.8. The thermal desorption feature is dominated by a well-defined main peak centred around 350 K. In order to extract desorption kinetic parameters, a Redhead - based analysis has been applied to the desorption threshold region [249]. By assuming a preexponential factor of  $10^{13} \text{ s}^{-1}$  and using the Redhead equation with heating rates of  $\beta = 1 \text{ K s}^{-1}$ , respectively (determined from the differential of the experimental heating curve of the sample at the peak temperatures), enthalpies of 0.9 to 1.5 eV for the desorption peak were determined. This is in very good agreement with the calculated differential binding energies of 0.8 to 1.6 eV for the AT adsorption models and close to earlier TDS work that reported a range

## 8. Water Adsorption on the $\alpha\text{-Al}_2\text{O}_3(0001)$ Surface

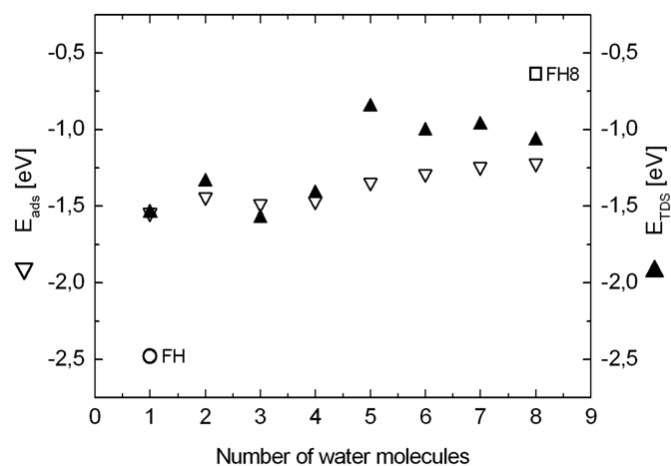


**Figure 8.7.:** Calculated adsorption energy per water molecule for the adsorption configurations AT1 - AT8 as well as FH, FH1, and FH8 models.

of 1.0 to 1.8 eV [223].

Fig. 8.8 demonstrates that  $\text{H}_2\text{O}$  desorbs over a wide range of temperatures from 300 to 450 K. This range of desorption temperatures corresponds to a variation of desorption energies as found in our calculation for the AT8 model (and related, disordered structures) that contain both dissociatively and molecularly adsorbed water. From the TPD data we would therefore conclude that the different surface treatments studied here lead (at least locally) to structures similar to AT8. The low surface mobility of water related to the highly corrugated PES may kinetically stabilize such structures even for low coverages. However, we cannot completely exclude surface defects such step edges [250, 251] to contribute to the broadening of the TPD peak. The excellent  $(1\times 1)$  LEED pattern as well as our AFM data, cf. Fig. 8.1, indicates, though, that surface defects are not the main reason for the broadening. The adsorption energies concluded from the TPD experiments are clearly not compatible with the calculations for the FH models. While the removal of an water molecule from the FH surface requires an energy of about 2.5 eV, water in excess on top of the FH structure is very weakly bound, with adsorption energies only slightly larger than 0.5 eV. These values

## 8. Water Adsorption on the $\alpha\text{-Al}_2\text{O}_3(0001)$ Surface

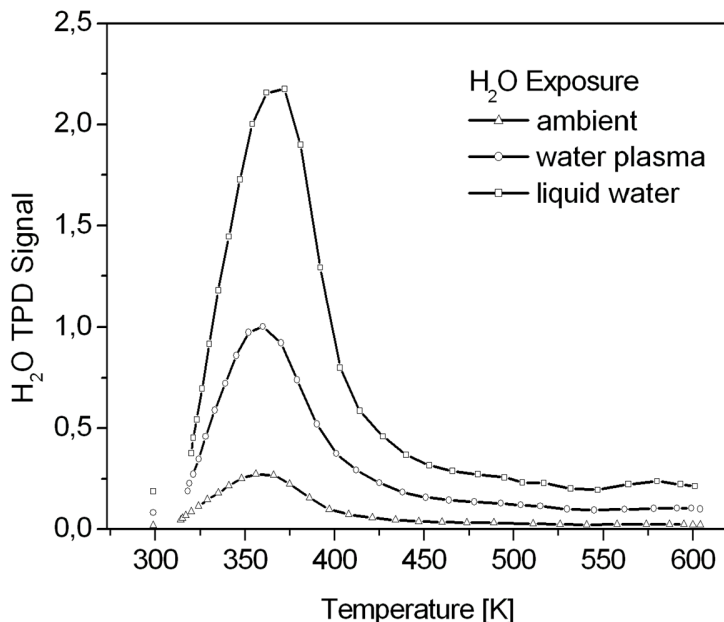


**Figure 8.8.:** TPD spectra of  $\text{H}_2\text{O}$  from the  $\alpha\text{-Al}_2\text{O}_3(0001)$  surface recorded after various  $\text{H}_2\text{O}$  exposures at 298 K. The heating rate was  $1 \text{ Ks}^{-1}$ .

are outside the range of 0.9 to 1.5 eV obtained from the desorption peak.

## 8.5. Conclusions

To summarize, DFT-GGA calculations as well as TPD spectroscopy for water adsorbed on the clean  $\alpha\text{-Al}_2\text{O}_3(0001)$  surface were performed. For low water coverages dissociated single water molecules are energetically most favored on the Al-terminated surface. The PES for both intact water molecules as well as water fragments adsorbed on  $\alpha\text{-Al}_2\text{O}_3(0001)$  is highly corrugated, indicating a low surface mobility. Increasing the water coverage on the Al-terminated surface favors complex structures consisting of both dissociated and intact water monomers. The corresponding variation of the adsorption energy per atom is in good accord with our TPD data. The thermodynamic ground-state of the surface is fully hydrogenated. The corresponding adsorption energies, however, are either too large (fully hydroxylated surface) or too low (adsorption

### 8. *Water Adsorption on the $\alpha$ - $Al_2O_3(0001)$ Surface*

on top of the fully hydroxylated surface) to account for our TPD data. We therefore conclude that the adsorption kinetics is very important and that therefore the actual surface composition will depend on the sample history.

## 9. Overall conclusions and Outlook

The corrosion resistance and the adhesion of organic coatings on oxide covered surfaces are of high importance and are mainly determined by the alloy composition, the surface chemistry of the alloy and the composition of the organic coating. To substitute anodizing processes or chromate layers, adhesion promoting, ultra-thin films or even monomolecular layers like self-assembled monolayers of organophosphonic acids have been investigated as new advanced interfacial layers for polymer coated aluminum alloys.

As a first step the water and subsequent argon plasma modification of native oxide covered aluminum was studied by in-situ IRRAS. These measurements in combination with ex-situ XPS showed that a water plasma treatment increases the density of hydroxides in the oxide surface layer while a subsequent argon plasma transforms the hydroxides to oxides. The combination of ex-situ IRRAS and XPS with QCM measurements of the adsorption process of ODPAs as well on native oxide covered aluminum as on plasma modified films has shown a strong dependence of the adsorption kinetics on the density of hydroxyl functions on the oxide covered aluminum surface. By the increase in the surface hydroxyl density the adsorption kinetics can be accelerated. Such an acceleration can be explained by the adsorption of the phosphonic acid via surface hydrogen bonds prior to the condensation reaction leading to the finally adsorbed phosphonate.

QCM investigations revealed that the amount of gas phase water adsorbing on a oxide covered aluminum surface is much higher than on a ODPAs monolayer covered one. One reason is the dependence of the adsorption energy on the surface termination.

IRRAS measurements have shown that isotopic plasmas of  $H_2O$  and  $D_2O$  can reversibly exchange the protons in native oxide covered aluminum. This isotope exchange in the oxide covered aluminum surface can be full-

## 9. Overall conclusions and Outlook

filled by gas overflow.

A SAM of ODPA can decrease the isotopic exchange rate, but cannot stop it. By means of IRRAS it was found that the proton exchange does not modify the ODPA barrier while a short water plasma treatment completely destroys it.

OES and XPS have been employed to characterize the effect of water plasma on a SAM. The optical emission spectra have shown that the most active species in the water plasma is hydrogen. This makes the water plasma a favorable cleaning agent against organics, which is confirmed by the XPS investigations.

For different industrial relevant steel coatings it was shown that the adsorption of ODPA on aluminum oxide covered surfaces is based on an acid-base reaction of the surface and the ODPA. The driving force for the formation of the monolayer is an acid-base type of interaction. The investigations have shown that Galfan, Galvalume and aluminium have a close aluminum oxide surface.

On ZnO covered surfaces precipitation layers are more stable than SAMs. This was shown for the Zn – 0.5% – Al (HDG) surface.

The results of the stability of ODPA adsorbed on the ZnAl alloy coatings in competition with water confirmed the idea of very different surface chemistries of the aluminium oxide covered surfaces and the zinc oxide covered surfaces. While the SAMs build up dense packages on the aluminum oxide and resist the water, the precipitation layers on the zinc oxide surfaces do not give any prevention in the competition with water. The results suggest an extremely important role of the alloy composition, the surface chemistry of the alloy and the composition of the organic coating with regard to the formation of stable phosphonic acid films in competition with water.

The stability of ODPA self-assembly films towards water was investigated on four different model substrates. This comparative study revealed, that ODPA SAMs are stable on (1) native aluminum oxide on a metal support as well as (2) on amorphous aluminum oxide and (3) on  $Al_2O_3(1-102)$ . In contrast, ODPA films are not stable in water on (4) the single crystalline  $Al_2O_3(0001)$  surfaces and immediately form micelle-like islands at the solid/liquid interface after immersion. This suggests that the adhesion free energies as well as the local atomic arrangements at the surface play a crucial role for the formation of a stable self-assembly film on aluminum oxide. For the amorphous surfaces also the formation of an

## 9. Overall conclusions and Outlook

insoluble surface salt has to be considered based on the presented results. The stability of the resulting bonding is based on three main competing influences, namely

- (1):** the interfacial bonding type.
- (2):** the adsorption free energy in competition with water.
- (3):** the adsorption geometries.

Concluding, the results suggest an extremely important role of the local atomic structure of the aluminum oxide surface with regard to the formation of stable phosphonic acid films in competition with water. For technological applications it has to be considered, that polar aluminium surfaces should possibly be avoided if high stability of the binding is desired and vice versa. A comparative approach as presented in this work is expected to be valuable not only for the surface-adhesive system at hand but also for other relevant surface-adhesive systems. The understanding and discussion of the underlying physical driving forces for adhesion and de-adhesion becomes straightforward, based on this differential approach. Moreover a direct comparison with state-of-the-art ab initio based results is possible.

DFT-GGA calculations as well as TPD spectroscopy for water adsorbed on the clean  $\alpha$ -Al<sub>2</sub>O<sub>3</sub>(0001) surface were performed successfully. For low water coverages dissociated single water molecules are energetically most favored. Increasing the water coverage, however, favors complex structures consisting of both dissociated and intact water monomers. The corresponding variation of the adsorption energy per atom is in good accord with our TPD data. The PES for both intact water molecules as well as water fragments adsorbed on  $\alpha$ -Al<sub>2</sub>O<sub>3</sub>(0001) is highly corrugated, leading to a low surface mobility.

Rational design and advancement in materials science will ultimately rely on an atomic-scale understanding of the targeted functionality. In macroscopic systems of technological relevance, this functionality typically results from the interplay of a large number of distinct atomic-scale processes. This makes quantitative calculations challenging, since it requires not only to compute many individual elementary processes with high accuracy to reach the aspired predictive power, but also to appro-

## 9. Overall conclusions and Outlook

priately account for the statistical mechanics of the interplay of all these processes. Unfortunately the timeframe of molecular dynamics (MD) is limited to a few nanoseconds and cannot encompass all of the involved processes, such as diffusion and segregation. Kinetic Monte Carlo (KMC) techniques on a rigid lattice are, on the other hand, especially fit for the simulation of these phenomena.

But when should a scientist consider quantum mechanical modeling? The example given in this work suggests a successful comparison of theoretical and experimental work. Afterwards, the modeling can be extended to situation, where measuring is impossible. This way, one can start predicting properties of materials and their failure by atomistic modeling based on experimental data. In the future, another relevant consideration for industrial cooperation will be the question what can be calculated and at what cost? From an economic point of view, quantum mechanical modeling has enormous advantage over the experimental chemistry. While there is just one kind of apparatus needed to calculate all physical properties that are related to the total energy, completely different experimental set ups are required to measure them.

In the end, only a combination of basic research on the one hand, and direct cooperation with industry on the other hand, can be the key for fundamental comprehension and adequate progress.

# Bibliography

- [1] R D'Agostino, Plasma deposition, treatment, and etching of polymers. 1990, Boston: Acad. Press.
- [2] G Grundmeier, P Thiemann, J Carpentier, N Shirtcliffe, M Stratmann, Thin Solid Films **446**, 61 (2004).
- [3] G Grundmeier, M Stratmann, Applied Surface Science **141**, 43 (1999).
- [4] NJ Shirtcliffe, M Stratmann, G Grundmeier, Surface and Interface Analysis, 2003. 35(10): p. 799-804. **14**, 663 (1999).
- [5] AR Marder, Progress in Materials Science **45**, 191 (2000).
- [6] GJ Harvey, PN Richards, Metals Forum **6**, 234 (1983).
- [7] D Coutsouradis, FE Goodwin, J Pelerin, AF Skenazi, A Davin, Stahl und Eisen **104**, 1073 (1984).
- [8] SJ Makimattila, EO Ristolainen, M Sulonen, VK Lindroos, Scripta Metallurgica **19**, 211 (1985).
- [9] JH Selverian, AR Marder, MR Notis, Journal of Materials Engineering **9**, 133 (1987).
- [10] M Giza, P Thissen, G Grundmeier, Langmuir **24**, 8688 (2008).
- [11] I Maege, E Jaehne, A Henke, HJP Adler, C Bram, C Jung, M Stratmann, Progress in Organic Coatings **34**, 1 (1998).
- [12] J Pahnke, J Ruhe, J. Macromol. Rapid Commun. **25**, 1396 (2004).
- [13] K Wapner, M Stratmann, G Grundmeier, International Journal of Adhesion and Adhesives **28**, 59 (2008).
- [14] P Thissen, M Valtiner, G Grundmeier, submitted to Langmuir.

## *Bibliography*

- [15] A Marmier, A Lozovoi, MW Finnis, *Journal of the European Ceramic Society* **23**, 2729 (2002).
- [16] G Renaud, *Surface Science Reports* **32**, 1 (1998).
- [17] T Suzuki, S Hishita, K Oyoshi, R Souda, *Surface Science* **437**, 289 (1999).
- [18] C Barth and M Reichling, *Nature* **414**, 54 (2001).
- [19] J Wang, A Howard, RG Egdell, JB Pethica, JS Foord, *Surface* **6**, 597 (2007).
- [20] C Niu, K Shepherd, D Martini, J Tong, JA Kelber, DR Jennison, A Bogicevic, *Surface Science* **465**, 163 (2000).
- [21] JA Kelber, CY Niu, K Shepherd, DR Jennison, A Bogicevic, *Surface Science* **446**, 76 (2000).
- [22] V Maurice, N Fremy, P Marcus, *Surface Science* **581**, 88 (2005).
- [23] E Gillet, B Ealet, *Surface Science* **273**, 427 (1992).
- [24] MA Schildbach, AV Hamza, *Surface Science* **282**, 306 (1993).
- [25] M Gillet, A Al Mohammed, K Masek, E Gillet, *Thin Solid Films* **374**, 134 (2000).
- [26] TP Trainor, PJ Eng, GE Brown, IK Robinson, M De Santis, *Surface Science* **496**, 238 (2002).
- [27] AR Marder, *Progress in Materials Science* **45**, 191 (2000).
- [28] SF Radtke, DC Herrschaft, *Journal of the Less-Common Metals* **93**, 253 (1983).
- [29] GJ Harvey, PN Richards, *Metals Forum* **6**, 234 (1983).
- [30] D Coutsouradis, FE Goodwin, J Pelerin, AF Skenazi, A Davin, *Stahl und Eisen* **104**, 1073 (1984).
- [31] SJ Makimattila, EO Ristolainen, M Sulonen, VK Lindroos, *Scripta Metallurgica* **19**, 211 (1985).

## *Bibliography*

- [32] ST Bluni, MR Notis, AR Marder, *Acta Metallurgica et Materialia* **43**, 1775 (1995).
- [33] SJ Makimattila, *Scandinavian Journal of Metallurgy* **15**, 224 (1986).
- [34] ST Bluni, AR Marder, JI Goldstein, *Materials Characterization* **33**, 93 (1994).
- [35] JH Selverian, AR Marder, MR Notis, *Metallurgical Transactions A* **20**, 543 (1989).
- [36] JH Selverian, AR Marder, MR Notis, *Journal of Electron Microscopy Technique* **5**, 223 (1987).
- [37] JH Selverian, AR Marder, MR Notis, *Journal of Materials Engineering* **9**, 133 (1987).
- [38] WC Bigelow, DL Pickett, WA Zisman, *Journal of Colloid Science* **1**, 513 (1946).
- [39] RG Nuzzo, DL Allara, *Journal of the American Chemical Society* **105**, 4481 (1983).
- [40] I Doudevski, DK Schwartz, *Applied Surface Science* **175**, 17 (2001).
- [41] R Maoz, J Sagiv, *Journal of Colloid and Interface Science* **100**, 465 (1984).
- [42] GE Poirier, *Chemical Reviews* **97**, 1117 (1997).
- [43] N Cabrera, NF Mott, HH Wills Physical Laboratory, University of Bristol.
- [44] A Ulman, *Chemical Reviews* **96**, 1533 (1996).
- [45] DK Schwartz, *Annual Review of Physical Chemistry* **52**, 107 (2001).
- [46] CH Chang, EI Franses, *Colloids and Surfaces A* **100**, 1 (1995).
- [47] KA Peterlinz, R Georgiadis, *Langmuir* **12**, 4731 (1996).
- [48] DS Karpovich, GJ Blanchard, *Langmuir* **10**, 3315 (1994).

## Bibliography

- [49] O Dannenberger, M Buck, M Grunze, *Journal of Physical Chemistry B* **103**, 2202 (1999).
- [50] CD Bain, EB Troughton, YT Tao, J Evall, GM Whitesides, RG Nuzzo, *Journal of the American Chemical Society* **111**, 321 (1989).
- [51] S Xu, SJN Cruchon-Dupeyrat, JC Garno, *GY* **60**, 1962 (1988).
- [52] LS Jung, CT Campbell, *Physical Review Letters* **84**, 5164 (2000).
- [53] RF DeBono, GD Loucks, D DellaManna, UJ Krull, *Canadian Journal of Chemistry* **74**, 677 (1996).
- [54] HJP Adler, *Progress in Organic Coatings* **34**, 1 (1998).
- [55] ES Gawalt, *Langmuir* **22**, 6469 (2006).
- [56] E Hoque, *J Phys Chem* **110**, 10855 (2006).
- [57] K Wapner, M Stratmann, G Grundmeier, *International Journal of Adhesion and Adhesives* **28**, 59 (2008).
- [58] J Pahnke, J Rühle, *Makromol Rapid Commun* **28**, 1396 (2004).
- [59] E Schrödinger, *Ann Physik* **79** 361 (1926).
- [60] M Born, JR Oppenheimer, *Ann Physik* **84** 457 (1927).
- [61] P Hohenberg, W Kohn, *Physical Review* **136** 864 (1964).
- [62] W Kohn, LJ Sham, *Physical Review* **140** 1133 (1965).
- [63] JC Slater, *Quantum Theory of Molecular and Solids. Vol. 4: The Self-Consistent Field for Molecular and Solids* (McGraw-Hill, New York, 1974).
- [64] C Stromberg, P Thissen, I Klueppel, N Fink, G Grundmeier, *Electrochimica Acta* **52**, 804 (2006).
- [65] JF Stephens, *Surface of Colloid and Interface Science* **38** 2 (1972).
- [66] S Hermes, RA Fischer, L Khodeir, *Journal of the American Chemical Society* **231** 83 (2006).
- [67] AN Rider, DR Arnott, *Surface and Interface Analysis* **21** 179 (1996).

## *Bibliography*

- [68] JW Bibber, *Metal Finishing* **5** 85 (1991).
- [69] E Vago, K de Waeldige, M Rohwerder, *Fres. J. Anal. Chem.* **353** 316 (1995).
- [70] J Benne, S Ballandras, F Cherioux, *Applied Surface Science* **255** 1796 (2008).
- [71] M Volmer, *Anbindung von Mercaptanen und deren Einfluß auf elektrochemische Reaktionen an Eisenoberflächen*, Dissertation Dortmund (1989).
- [72] KL Mittal, *Silanes and other coupling agents*, VSP (1992).
- [73] RD Ramsier, PN Henriksen, AN Gent, *Surface Science* **203** 72 (1988).
- [74] HL Skriver, NM Rosengaard, *Physical Review* **46** 7157 (1992).
- [75] R Browning, T Vanzandt, CR Helms, *Journal of Electron Spectroscopy and Related Phenomena* **51** 315 (1990).
- [76] BL Wang, *Spectroscopy* **12**, 30 (1997).
- [77] BJ Barner, MJ Green, EI Saez, RM Corn, *Analytical Chemistry* **63**, 55 (1991).
- [78] MD Ward, EJ Delawski, *Analytical Chemistry* **63**, 886 (1991).
- [79] SJ Martin, GC Frye, AJ Ricco, SD Senturia, *Analytical Chemistry* **65**, 2910 (1993).
- [80] CK O'Sullivan GG Guilbault, *Biosensors and Bioelectronics* **14**, 663 (1999).
- [81] C Gabrielli, M Keddah, R Torresi, *Journal of the Electrochemical Society* **138**, 2657 (1991).
- [82] DR Denison, *Journal of Vacuum Science and Technology* **10**, 126 (1973).
- [83] KH Behrndt, *Journal of Vacuum Science and Technology* **8**, 622 (1971).

## *Bibliography*

- [84] CS Lu, *Journal of Vacuum Science and Technology* **12**, 578 (1975).
- [85] M Rodahl, B Kasemo, *Sensors and Actuators B-Chemical* **37**, 111 (1996).
- [86] F Josse, Y Lee, SJ Martin, RW Cernosek, *Analytical Chemistry*, **70**, 237 (1998).
- [87] <http://www.maxtek.com/>
- [88] FM Fowkes, *Industrial and Engineering Chemistry*, **56**, 40 (1964).
- [89] G Grundmeier, W Schmidt, M Stratmann, *Electrochimica Acta* **45**, 2515 (2000).
- [90] M Rohwerder, G Grundmeier, M Stratmann, *Corrosion Mechanisms in Theory and Practice*, 479 (2002).
- [91] I Maege, E Jaehne, A Henke, HJP Adler, C Bram, C Jung, M Stratmann, *Progress in Organic Coatings* **34**, 1 (1998).
- [92] J Pahnke, J Ruhe, *Macromolecular Rapid Communications* **25**, 1396 (2004).
- [93] K Wapner, M Stratmann, G Grundmeier, *International Journal of Adhesion and Adhesives* **28**, 59 (2008).
- [94] DL Allara, RG Nuzzo, *Langmuir* **1**, 45 (1985).
- [95] J van den Brand, O Blajiev, PCJ Beentjes, H Terryn, JHW de Wit, *Langmuir* **20**, 6308 (2004).
- [96] J van den Brand, O Blajiev, PCJ Beentjes, H Terryn, JHW de Wit, *Langmuir* **20**, 6318 (2004).
- [97] CK O'Sullivan, GG Guilbault, *Biosensors and Bioelectronics* **14**, 663 (1999).
- [98] J Raacke, M Giza, G Grundmeier, *Surface and Coatings Technology* **200**, 280 (2005).
- [99] G Sauerbrey, *Zeitschrift Fur Physik* **155**, 206 (1959).

## Bibliography

- [100] G Grundmeier, M Stratmann, *Berichte Der Bunsen-Gesellschaft-Physical Chemistry Chemical Physics*, **99**, 1387 (1995).
- [101] G Grundmeier, E Matheisen, M Stratmann, *Journal of Adhesion Science and Technology* **10**, 573 (1996).
- [102] J van den Brand, S Van Gils, PCJ Beentjes, H Terryn, JHW de Wit, *Applied Surface Science* **235**, 465 (2004).
- [103] S Van Gils, CA Melendres, H Terryn, *Surface and Interface Analysis* **35**, 387 (2003).
- [104] AB Kiss, G Keresztury, L Farkas, *Spectrochimica Acta Part a-Molecular and Biomolecular Spectroscopy* **36**, 653 (1980).
- [105] D Briggs, *Practical surface analysis*. 1983, Wiley: Chichester.
- [106] E McCafferty, JP Wightman, *Surface and Interface Analysis* **26**, 549 (1998).
- [107] MR Alexander, GE Thompson, G Beamson, *Surface and Interface Analysis* **29**, 468 (2000).
- [108] F Cordier, E Ollivier, *Surface and Interface Analysis* **23**, 601 (1995).
- [109] K Wapner, M Stratmann, G Grundmeier, *International Journal of Adhesion and Adhesives* **28**, 59 (2008).
- [110] J Pahnke, J Ruhe, *Macromol. Rapid Commun.* **25**, 1396 (2004).
- [111] I Maege, E Jaehne, A Henke, HJP Adler, C Bram, C Jung, M Stratmann, *Progress in Organic Coating* **34**, 1 (1998).
- [112] G Grundmeier, W Schmidt, M Stratmann, *Electrochimica Acta* **45**, 2515 (2000).
- [113] M Rohwerder, G Grundmeier, M Stratmann, *Corrosion Mechanism in Theory and Practice*, JOP Marcus, Editor. 2002, Marcel Dekker: New York. p479.
- [114] E Jaehne, S Oberoi, HJ Adler, *Progress in Organic Coatings* **61**, 211 (2008).

## Bibliography

- [115] DL Allara, RG Nuzzo, *Langmuir* **1**, 45 (1985).
- [116] J van den Brand, O Blajiev, PCJ Beentjes, H Terryn, JHW de Wit, *Langmuir* **20**, 6308 (2004).
- [117] J van den Brand, O Blajiev, PCJ Beentjes, H Terryn, JHW de Wit, *Langmuir* **20**, 6318 (2004).
- [118] M Giza, P Thissen, G Grundmeier, *Langmuir* **24**, 8688 (2008).
- [119] D Beaglehole, HK Christenson, *J. Phys. Chem.* **96**, 3395 (1992).
- [120] T Hasegawa, J Nishijo, T Imae, Q Huo, RM Leblanc, *J. Phys. Chem. B* **105**, 12056 (2001).
- [121] EG Ewing, *J. Phys. Chem. B* **108**, 15953 (2004).
- [122] M Mezger, H Reichert, S Schröder, J Okasinski, H Schröder, H Dosch, D Palms, J Ralston, V Honkimäki, *Proceedings of the National Academy of Sciences* **103**, 18401 (2006).
- [123] J Raacke, M Giza, G Grundmeier, *Surface and Coatings Technology* **200**, 280 (2005).
- [124] G Grundmeier, M Stratmann, *Berichte der Bunsen-Gesellschaft* **99**, 1387 (1995).
- [125] G Grundmeier, E Matheisen, M Stratmann, *Journal of Adhesion Science and Technology* **10**, 573 (1996).
- [126] G Sauerbrey, *Zeitschrift für Physik* **155**, 206 (1959).
- [127] DB Asay, SH KIM, *J. Phys. Chem. B* **109**, 16760 (2005).
- [128] A Thiel, TE Madey, *Surf. Sci. Rep.* **7**, 211 (1987).
- [129] Q Du, E Freysz, YR Shen, *Science* **264**, 826 (1994).
- [130] JR Zimmerman, JA Lasater, *J. Phys. Chem.* **62**, 1157 (1958).
- [131] Y Kuroda, S Kittaka, S Takahara, T Yamaguchi, MC Bellissent-Funel **103**, 11064 (1999).

## Bibliography

- [132] LH Guo, JS Facci, G McLendon, R Mosher, *Langmuir* **10**, 4588 (1994).
- [133] DA Hutt, GJ Leggett, *J. Phys. Chem.* **100**, 6657 (1996).
- [134] Y Zhang, RH Terrill, TA Tanzer, PA Bohn, *Journal of the American Chemical Society* **120**, 2654 (1998).
- [135] G Liu, JA Rodriguez, J Dvorak, J Hrbek, T Jirsak, *Surf. Sci.* **505**, 297 (2002).
- [136] EM Cheadle, DN Batchelder, SD Evans, HL Zhang, H Fukushima, S Miyashita, M Graupe, A Puck, EO Shmakova, R Colorado, TR Lee, *Langmuir* **17**, 6616 (2001).
- [137] K Raiber, A Terfort, *Surface Science* **56**, 56 (2005).
- [138] N Cabrera, F Mott, *Reports on Progress in Physics* **12**, 163 (1948).
- [139] K Stella, D Diesing, *J. Electrochem. Soc.* **154**, C663 (2007).
- [140] J van den Brand, S van Gils, PCJ Beentjes, H Terryn, JHW de Wit, *Applied Surface Science* **235**, 465 (2004).
- [141] Lawrence, H Dubois, R Bernard, A Zegarski, RG Nuzzo, *Proceedings in the National Academy of Sciences* **84**, 4739 (1987).
- [142] CK O'Sullivan, GG Guilbault, *Biosensors and Bioelectronics* **14**, 663 (1999).
- [143] B Wilson, N Fink, G Grundmeier, *Electrochimica Acta* **51**, 3066 (2006).
- [144] N Fink, B Wilson, G Grundmeier, *Electrochimica Acta* **51**, 2956 (2006).
- [145] G Grundmeier, W Schmidt, M Stratmann, *Electrochimica Acta* **45**, 2515 (2000).
- [146] G Grundmeier, M Stratmann, *Annual Review of Materials Research* **35**, 571 (2005).
- [147] G Grundmeier, M Stratmann, *Applied Surface Science* **141**, 43 (1999).

### *Bibliography*

- [148] K Wapner, M Stratmann, G Grundmeier, *International Journal of Adhesion and Adhesives* **28**, 59 (2008).
- [149] I Maege, E Jaehne, A Henke, HJP Adler, C Bram, C Jung, M Stratmann, *Progress in Organic Coatings* **34**, 1 (1998).
- [150] M Giza, P Thissen, G Grundmeier, *Langmuir* **24**, 8688 (2008).
- [151] KC Hass, WF Schneider, A Corioni, W Andreoni, *Journal of Physical Chemistry B* **104**, 5527 (2000).
- [152] VA Ranea, WF Schneider, I Carmichael, *Surface Science* **602**, 268 (2008).
- [153] J Edgar, AM Chaka, XG Wang, M Scheffler, D Barr, *Abstracts of Papers of the American Chemical Society* **220**, U187 (2000).
- [154] JW Elam, CE Nelson, MA Tolbert, SM George, *Surface Science* **450**, 64 (2000).
- [155] CE Nelson, JW Elam, MA Cameron, MA Tolbert, SM George, *Surface Science* **416**, 341 (1998).
- [156] A Frerichs, F Voigts, W Maus-Friedrichs, *Applied Surface Science* **253**, 950 (2006).
- [157] LC Thomas, R Chittend, *Spectrochimica Acta* **26**, 781 (1970).
- [158] MJ Pellerite, TD Dunbar, LD Boardman, EJ Wood, *Journal of Physical Chemistry B* **107**, 11726 (2003).
- [159] BL Frey, DG Hanken, RM Corn, *Langmuir* **9**, 1815 (1993).
- [160] CD Bain, EB Troughton, YT Tao, J Evall, GM Whitesides, RG Nuzzo, *Journal of the American Chemical Society* **111**, 321 (1989).
- [161] M Valtiner, S Borodin, G Grundmeier, *Langmuir* **24**, 5350 (2008).
- [162] N Tillman, A Ulman, JS Schildkraut, TL Penner, *Journal of the American Chemical Society* **110**, 6136 (1988).
- [163] C Barth, M Reichling, *Nature* **414**, 54 (2001).

## Bibliography

- [164] VA Ranea, A Michaelides, R Ramirez, JA Verges, PL de Andres, DA King, *Physical Review B* **69** (2004).
- [165] S Meng, EG Wang, SW Gao, *Physical Review B* **69** (2004).
- [166] S Wendt, R Schaub, J Matthiesen, EK Vestergaard, E Wahlstrom, MD Rasmussen, P Thostrup, LM Molina, E Laegsgaard, I Stensgaard, B Hammer, F Besenbacher, *Surface Science* **598**, 226 (2005).
- [167] JJ Yang, EG Wang, *Physical Review B* **73** (2006).
- [168] S Tosoni, K Doll, P Ugliengo, *Chemistry of Materials* **18**, 2135 (2006).
- [169] XL Hu, A Michaelides, *Surface Science* **602**, 960 (2008).
- [170] C Ruberto, Y Yourdshahyan, BI Lundqvist, *Physical Review B* **67** (2003).
- [171] PJ Eng, TP Trainor, GE Brown, GA Waychunas, M Newville, SR Sutton, ML Rivers, *Science* **288**, 12 (2000).
- [172] MS Lim, ES Gawalt, AT Timperman, *Langmuir* **23**, 2444 (2007).
- [173] MJ Brukman, GO Marco, TD Dunbar, LD Boardman, RW Carpick, *Langmuir* **22**, 3988 (2006).
- [174] T Becker, A Birkner, G Witte, C Wöll, *Physical Review B* **65** (2008).
- [175] TTT Nguyen, D Bonamy, L Pham Van, L Barbier, J Cousty, *Surface Science* **602**, 3232 (2008).
- [176] XG Wang, AM Chaka, M Scheffler, *Physical Review Letters* **84** (1999).
- [177] EA Soares, MA van Hove, CF Walters, KF McCarty, *Physical Review B* **65** (2001).
- [178] RG Snyder, *J. Mol. Spectrosc.* **4**, 411 (1960).
- [179] IL Liakos, E McAlpine, X Chen, R Newman, MR Alexander, *Applied Surface Science* **255**, 3282 (2008).

## *Bibliography*

- [180] G Grundmeier, W Schmidt, M Stratmann, *Electrochimica Acta* **45**, 2515 (2000).
- [181] G Grundmeier, M Stratmann, *Annual Review of Materials Research* **35**, 571 (2005).
- [182] G Grundmeier, M Stratmann, *Applied Surface Science* **141**, 43 (1999).
- [183] C Stromberg, P Thissen, I Klueppel, N Fink, G Grundmeier, *Electrochimica Acta* **52**, 804 (2006).
- [184] I Maege, E Jaehne, A Henke, HJP Adler, C Bram, C Jung, M Stratmann, *Progress in Organic Coatings* **34**, 1 (1998).
- [185] W Miao, *Journal of the Electrochemical Society* **154**, 1 (2007).
- [186] H Dafydd, *Corrosion Science* **47**, 3006 (2005).
- [187] J Elvins, *Corrosion Engineering, Science and Technology* **38**, 197 (2003).
- [188] J Elvins, *Corrosion Science* **47**, 2740 (2005).
- [189] IL Liakos, MR Alexander, *Surf. Interface Anal.* **36**, 347 (2004).
- [190] K Wapner, M Stratmann, G Grundmeier, *International Journal of Adhesion and Adhesives* **28**, 59 (2008).
- [191] J van den Brand, H Terryn, *Progress in Organic Coatings* **51**, 339 (2004).
- [192] J Ruhe, *Langmuir* **20**, 10080 (2004).
- [193] J Pahnke, J Ruhe, *Macromol Rapid Commun.* **25**, 1396 (2004).
- [194] S Pawsey, *Langmuir* **18**, 5205 (2002).
- [195] M Giza, P Thissen, G Grundmeier, *Langmuir* **24**, 8688 (2008).
- [196] AR Marder, *Progress in Materials Science* **45**, 191 (2000).
- [197] CE Jordan, AR Marder, *Met. Mater. Trans.* **28**, 2695 (1997).

## *Bibliography*

- [198] JL Murray, TB Massalski, editor. Materials Park, OH: ASM 185 (1986).
- [199] PJ Gellings, EW de Bree, G Giermann, *Z Metallkde* **70**, 312 (1979).
- [200] JH Selverian, AR Marder, MR Notis, *Met. Mater. Trans.* **19**, 1193 (1988).
- [201] ARP Ghuman, JI Goldstein, *Met. Mater. Trans.* **2**, 2903 (1971).
- [202] S van Gils, CA Melendres, H Terryn, *Surface and Interface Analysis* **35**, 387 (2003).
- [203] AB Kiss, G Keresztury, L Farkas, *Spectrochimica Acta Part A* **36**, 653 (1980).
- [204] J van den Brand, O Blajiev, PCJ Beentjes, H Terryn, JHW de Wit, *Langmuir* **20**, 6308 (2004).
- [205] N Fink, B Wilson, G Grundmeier, *Electrochimica Acta* **51**, 2956 (2006).
- [206] M Frerichs, F Voigts, W Maus-Friedrichs, *Applied Surface Science* **253**, 950 (2006).
- [207] B Wilson, N Fink, G Grundmeier, *Electrochimica Acta* **51**, 3066 (2006).
- [208] PR Davies, NG Newton, *Appl. Surf. Sci.* **18**, 296 (2001).
- [209] C Jung, *Alkylphosphonsäuren als Haftvermittler für Aluminium und Zinkwerkstoffe*, Technische Fakultät der Universität Erlangen (1998).
- [210] N Tillman, A Ulman, JS Schildkraut, TL Penner, *Journal of the American Chemical Society* **110**, 6136 (1988).
- [211] P Thissen, M Valtiner, G Grundmeier, submitted to *Langmuir*.
- [212] P Wernet, D Nordlund, U Bergmann, M Cavalleri, M Odelius, H Ogasawara, L Å Naäslund, T K Hirsch, L Ojamäe, P Glatzel, L G M Pettersson, and A Nilsson, *Science* **304**, 995 (2004).

## *Bibliography*

- [213] A Hermann, W G Schmidt, and P Schwerdtfeger, *Phys. Rev. Lett.* **100**, 207403 (2008).
- [214] M Henderson, *Surf. Sci. Rep.* **46**, 1 (2002).
- [215] P J Feibelman, *Science* **295**, 99 (2002).
- [216] P J Feibelman, *Phys. Rev. Lett.* **90**, 186103 (2003).
- [217] A Michaelides and K Morgenstern, *Nature Materials* **6**, 597 (2007).
- [218] J Stähler, M Mehlhorn, U Bovensiepen, M Meyer, D. O Kusmirek, K Morgenstern, and M Wolf, *Phys. Rev. Lett.* **98**, 206105 (2007).
- [219] F Traeger, D Langenberg, Y. K Gao, and Ch Wöll, *Phys. Rev. B* **76**, 033410 (2007).
- [220] S Wippermann and W G Schmidt, *Phys. Rev. B* **78**, 235439 (2008).
- [221] V Coustet and J Jupille, *Surf. Sci.* **307-309**, 1161 (1994).
- [222] J.W Elam, C E Nelson, M A Cameron, M A Tolbert, and S.M George, *J. Phys. Chem. B* **102**, 7008 (1998).
- [223] C E Nelson, J.W Elam, M A Cameron, M A Tolbert, and S M George, *Surf. Sci.* **416**, 341 (1998).
- [224] P Liu, T Kendelewicz, G E Brown, E J Nelson, and S A Chambers, *Surf. Sci.* **417**, 53 (1998).
- [225] D B Almy, D C Foyt, and J M White, *J. Electron Spec. and Rel. Phenom.* **11**, 129 (1977).
- [226] C Barth and M Reichling, *Nature* **414**, 54 (2001).
- [227] K. C Hass, *Science* **282**, 265 (1998).
- [228] R Di Felice and J E Northrup, *Phys. Rev. B* **60**, R16287 (1999).
- [229] V Shapovalov and T N Truong, *J. Phys. Chem. B* **104**, 9859 (2000).
- [230] J M Wittbrodt, W L Hase, and H B Schlegel, *J. Phys. Chem. B* **102**, 6539 (1998).

## Bibliography

- [231] V Ranea, W Schneider, and I Carmichael, *Surf. Sci.* **602**, 268 (2007).
- [232] P D Tepesch and A A Quong, *phys. stat. sol. (b)* **217**, 377 (2000).
- [233] X-G Wang, A Chaka, and M Scheffler, *Phys. Rev. Lett.* **84**, 3650 (2000).
- [234] R Di Felice and J E Northrup, *Phys. Rev. B* **60**, R16287 (1999).
- [235] V Ranea, I Carmichael, and W Schneider, *J. Phys. Chem. C* **113**, 2149 (2009).
- [236] G Kresse and J Furthmüller, *Comp. Mat. Sci.* **6**, 15 (1996).
- [237] G Kresse and D Joubert, *Phys. Rev. B* **59**, 1758 (1999).
- [238] J P Perdew, J A Chevary, S H Vosko, K A Jackson, M R Pederson, D J Singh, and C Fiolhais, *Phys. Rev. B* **46**, 6671 (1992).
- [239] D R Hamann, *Phys. Rev. B* **55**, R10157 (1997).
- [240] C Thierfelder, A Hermann, P Schwerdtfeger, and W G Schmidt, *Phys. Rev. B* **74**, 045422 (2006).
- [241] I Batyrev, A Alavi, and M W Finnis, *Faraday Discussions* **114**, 33 (1999).
- [242] M Causa, R Dovesi, C Pisani, and C Roetti, *Surf. Sci.* **215**, 259 (1989).
- [243] Arnaud Marmier and Stephen Parker, *Phys. Rev. B* **69**, 115409 (2004).
- [244] G-X Qian, R M Martin, and D J Chadi, *Phys. Rev. Lett.* **60**, 1962 (1988).
- [245] B Lange and W Schmidt, *Surf. Sci.* **602**, 1207 (2008).
- [246] Z Lodziana, J K Nørskov, and P Stoltze, *J. Chem. Phys.* **118**, 11179 (2003).
- [247] M J Stirniman, C Huang, R S Smith, S A Joyce, and B D Kay, *J. Chem. Phys.* **105**, 1295 (1996).

### *Bibliography*

- [248] N Mulakaluri, R Pentcheva, M Wieland, W Moritz, and M Schefler, *Verhandl. DPG (VI)* **44**, 465 (2009).
- [249] P A Redhead, *Vacuum* **12**, 203 (1962).
- [250] R C Barrett and C F Quate, *J. Vac. Sci. Technol. A* **8**, 400 (1990).
- [251] V E Heinrich and P A Cox, *The Surface Science of Metal Oxides* (Press Syndicate of the University of Cambridge, Cambridge, 1994).

## A. Glossary

<b>AES</b>	Auger Electron Spectroscopy
<b>AFM</b>	Atomic Force Microscopy
<b>DFT</b>	Density Functional Theory
<b>DRIFTS</b>	Diffuse Reflectance Infrared Fourier Transform Spectroscopy
<b>EBSD</b>	Electron Back Scattering Diffraction
<b>EELS</b>	Electron Energy Loss Spectroscopy
<b>FT-IR</b>	Fourier Transform Infrared Spectroscopy
<b>GIXRD</b>	Grazing Incident X-ray Diffraction
<b>hcp</b>	hexagonal closed package
<b>HDG</b>	Hot Dip Galvanizing
<b>IETS</b>	Inelastic Electron Tunneling Spectroscopy
<b>IF-steel</b>	Interstitial-Free steel
<b>LEED</b>	Low Energy Electron Diffraction
<b>LMIG</b>	Liquid Metal Ion Gun
<b>OES</b>	Optical Emission Spectroscopy
<b>ODPA</b>	OctaDecylPhosphonic Acid
<b>PEM</b>	Photoelastic Modulator
<b>PM-IRRAS</b>	Polarization Modulation - Infrared Reflection Absorption Spectroscopy
<b>PVD</b>	Physical Vapor Deposition
<b>QCM</b>	Quartz Crystal Microweighing
<b>QMS</b>	Quadropole Mass Spectrometer
<b>RHEED</b>	Reflection High Energy Electron Diffraction
<b>SAM</b>	Self-Assembled Monolayer
<b>SEM</b>	Scanning Electron Microscopy
<b>TDS</b>	Thermal Desorption Spectroscopy
<b>ToF-SIMS</b>	Time-of-Flight Secondary-Ion-Mass-Spectroscopy
<b>TPD</b>	Temperature Programmed Desorption
<b>UHV</b>	Ultra High Vacuum
<b>XPS</b>	X-ray Photoelectron Spectroscopy

## B. List of Symbols

$t$	Time
$T$	Temperature, Kinetic energy
$\Psi$	Wavefunction
$m$	Mass
$h$	Planck's constant
$V$	Potential, Potential energy
$E$	Energy
$H$	Hamiltonian
$Z$	Atomic number of an atom
$\Delta f$	Frequency change
$C_f$	Sensitivity factor
$\rho$	Density
$\eta$	Viscosity
$\gamma$	Surface tension
$E_{ads}$	Adsorption energy
$\Theta$	Surface coverage
$E_B$	Binding energy
$E_{kin}$	Kinetic energy
$e_\phi$	Electronic work function
$M$	Molar mass
$\lambda$	Inelastic mean free path
$F$	Faraday constant

## C. Publications

[1] C Stromberg, **P Thissen**, I Klueppel, N Fink, G Grundmeier, *Synthesis and characterisation of surface gradient thin conversion films on zinc coated steel*, *Electrochimica Acta* **52**, 804 (2006).

[2] M Giza, **P Thissen**, G Grundmeier, *Adsorption Kinetics of Organophosphonic Acids on Plasma Modified Oxide Covered Aluminum Surfaces*, *Langmuir* **24**, 8688 (2008).

[3] J Zuo, P Keil, M Valtiner, **P Thissen** and G Grundmeier, *Deposition of Ag Nanoparticles on fluoroalkylsilane self-assembled monolayers with varying chain length*, *Surface Science* **602**, 3750 (2006).

[4] **P Thissen**, M Valtiner, G Grundmeier, *Formation and Stability of Phosphonic Acid Self-Assembled Monolayers on Amorphous and Single Crystalline Aluminum Oxide Surfaces in Aqueous Solution*, submitted to *Langmuir*.

[5] **P Thissen**, G Grundmeier, S Wippermann and WG Schmidt, *Water Adsorption on the alpha-Al<sub>2</sub>O<sub>3</sub>(0001) Surface*, submitted to *Physical Review B*.

[6] **P Thissen**, J Wielant, M Köyer, S Toews and G Grundmeier, *Formation and Stability of Organophosphonic Acid Monolayers on ZnAl Alloy Coatings*, submitted to *Surface and Coatings Technology*.

[7] **P Thissen**, G Grundmeier, *Water Adsorption and Proton Exchange Reactions on Octadecylphosphonic Acid Monolayer Covered Aluminum*, in preparation.